Development of a Fiber-based Shape Sensor for Navigating Flexible Medical Tools

Inaugural dissertation

to
be awarded the degree of

Dr. sc. med.

presented at
the Faculty of Medicine
of the University of Basel

by
Samaneh Manavi
from Lahijan, Iran

Basel, 2022

Approved by the Faculty of Medicine
on application of

Prof. Dr. Philippe C. Cattin, University of Basel – *primary advisor*
Prof. Dr. med. Raphael Guzman, University of Basel – *secondary advisor*
Prof. Dr. Bernhard Schmauss, Friedrich-Alexander University Erlangen-Nuremberg – *external expert*
Dr. Sara Freund, University of Basel – *further advisor*

Basel, the 12th of December 2022

Prof. Dr. Primo Schär
Dean

بسم الله الرحمن الرحيم

*Dedicated to my parents, Masoumeh & Mohammad Ali, my husband, Ehsan,
and my son, Amir Ali.*

Contents

Acronyms

3D three-dimensional. xiii, 2, 6, 14, 15, 51, 101, 103

BPM beam propagation method. 12

CNN convolutional neural network. 19, 103

CW continuous wave. 8, 9

EM electromagnetic. xiii, 2, 5, 6, 9, 15, 16

FBG fiber Bragg grating. xiii, xv, 2, 3, 6–12, 14–16, 21, 25, 39, 51, 81, 101–104

FOSS fiber optic shape sensor. 6, 14

fs femtosecond. 7, 10, 11, 15

MCF multicore fiber. 6

MIRACLE minimally invasive robot-assisted computer-guided laserosteotome. 1

MIS minimally invasive surgical procedures. 1, 103

OFDR optical frequency domain reflectometry. 9, 10

OR operation room. 2

OTDR optical time domain reflectometry. 9, 10

PbP point-by-point. 7, 10, 11, 15

PMD polarization mode dispersion. 17

RAMIS robot-assisted minimally invasive surgical procedures. xiii, 1, 3, 101, 103, 104

TDM time-division-multiplexing. 7–9

UV ultraviolet. 7, 9

WDM wavelength-division-multiplexing. 7–9, 101

Acknowledgements

Looking back, I can see that it would have been impossible to be where I am now without the support of many individuals. I was so blessed to be surrounded by kind people in such an inspiring atmosphere to learn and gain experience, Alhamdulillah.

First, I would like to express my gratitude to my primary advisor, Prof. Dr. Philippe Cattin, for trusting me and allowing me to be a part of his research team. I sincerely thank you, Philippe, for your support and guidance during my PhD. I learned a lot from you, which will benefit me for the rest of my life.

Furthermore, I thank my secondary advisor, Prof. Dr. med. Raphael Guzman, for his support in the medical field. I would also like to thank Prof. Dr. Bernhard Schmauss for honoring me by reading and evaluating my thesis. Next, I would like to thank our collaborators from Fraunhofer Institute, Prof. Dr. Wolfgang Schade and Dr. Martin Angelmahr, for sharing their expertise and providing our eccentric FBG sensors.

Special thank goes to Dr. Sara Freund and Dr. Lilian Witthauer as my further advisors for our countless hours of discussions, proofreading my papers, and of course, listening to my complaints whenever I needed to talk to someone. Furthermore, I would like to thank all the members of the CIAN group, including Dr. Uri Nahum, Dr. Lorenzo Iafolla, Dr. Antal Huck, Dr. Christoph Jud, Dr. Robin Sandkuehler, Dr. Julia Wolleb, Carlo Seppi, Marek Zelechowski, Balazs Faludi, Massimiliano Filipozzi, Eva Schnider, Norbert Zentai, Madina Kojanazarova, Florentin Bieder, and many other past and present members. I enjoyed all the inspiring discussions and fun times we had. Thank you all.

In addition, I would like to thank the MIRACLE team, especially Dr. Azhar Zam, Dr. Georg Rauter, Dr. Ferda Canbaz, Dr. Nicolas Gerig, and Dr. Constanze Pfeiffer. Thank you for being such a great team; I enjoyed working with you. Also, a big thank goes to the administrative team, including Dr. Daniela Vavrecka-Sidler, Corinne Eymann-Baier, Dr. Gabriela Oser, Hannah Heissler, Dr. Beat Fasel, Beat Göpfert, and Dr. Reinhard Wendler. I would also like to thank Sascha Martin from the Physics Workshop for his technical support.

And last but not least, I would like to thank my dearest parents, Masoumeh and Mohammad Ali, for always being there for me. Making you proud and happy has always been my motivation booster. An especial thank goes to my beloved husband, Ehsan, who believed in me and supported me greatly. I could not do it without you; thank you. Furthermore, my deepest gratitude goes to my parent-in-law for their support. Finally, I would like to thank my dear son, Amir Ali, who was born during my PhD and brought me endless happiness and joy.

Thank you all!

Summary

Robot-assisted minimally invasive surgical procedure (RAMIS) is a subfield of minimally invasive surgeries with enhanced manual dexterity, manipulability, and intraoperative image guidance. In typical robotic surgeries, it is common to use rigid instruments with functional articulating tips. However, in some operations where no adequate and direct access to target anatomies is available, continuum robots can be more practical, as they provide curvilinear and flexible access. However, their inherent deformable design makes it difficult to accurately estimate their 3D shape during the operation in real-time. Despite extensive model-based research that relies on kinematics and mechanics, accurate shape sensing of continuum robots remains challenging. The state-of-the-art tracking technologies, including optical trackers, electromagnetic (EM) tracking systems, and intraoperative imaging modalities, are also unsuitable for this task, as they all have shortcomings. Optical fiber shape sensing solutions offer various advantages compared to other tracking modalities and can provide high-resolution shape measurements in real-time. However, commercially available fiber shape sensors are expensive and have limited accuracy.

In this thesis, we propose two cost-effective fiber shape sensing solutions based on multiple single-mode fibers with FBG (fiber Bragg grating) arrays and eccentric FBGs. First, we present the fabrication and calibration process of two shape sensing prototypes based on multiple single-mode fibers with semi-rigid and super-elastic substrates. Then, we investigate the sensing mechanism of edge-FBGs, which are eccentric Bragg gratings inscribed off-axis in the fiber's core. Finally, we present a deep learning algorithm to model edge-FBG sensors that can directly predict the sensor's shape from its signal and does not require any calibration or shape reconstruction steps.

In general, depending on the target application, each of the presented fiber shape sensing solutions can be used as a suitable tracking device. The developed fiber sensor with the semi-rigid substrate has a working channel in the middle and can accurately measure small deflections with an average tip error of $2.7\,\mathrm{mm}$. The super-elastic sensor is suitable for measuring medium to large deflections, where a centimeter range tip error is still acceptable. The tip error in such super-elastic sensors is higher compared to semi-rigid sensors ($9.9\,\mathrm{mm}$ to $16.2\,\mathrm{mm}$ in medium and large deflections, respectively), as there is a trade-off between accuracy and flexibility in substrate-based fiber sensors. Edge-FBG sensor, as the best performing sensing mechanism among the investigated fiber shape sensors, can achieve a tip accuracy of around $2\,\mathrm{mm}$ in complex shapes, where the fiber is heavily deflected. The developed edge-FBG shape sensing solution can compete with the state-of-the-art distributed fiber shape sensors that cost 30 times more.

Zusammenfassung

Robotergestützte minimalinvasive chirurgische Eingriffe sind ein Teilbereich der minimalinvasiven Chirurgie mit verbesserter manueller Geschicklichkeit, Manipulierbarkeit und intraoperativer Bildführung. Bei typischen Roboteroperationen werden in der Regel starre Instrumente mit funktionalen Gelenkspitzen verwendet. Bei einigen Operationen, bei denen kein adäquater und direkter Zugang zur Zielanatomie möglich ist, können jedoch Kontinuumsroboter praktischer sein, da sie einen gekrümmten und flexiblen Zugang bieten. Aufgrund ihrer verformbaren Konstruktion ist es jedoch schwierig, ihre 3D Form während des Eingriffs in Echtzeit genau abzuschätzen. Trotz umfangreicher Forschung modellbasierter Ansätze, die sich auf Kinematik und Mechanik stützt, bleibt die genaue Formerfassung von Kontinuumsrobotern eine Herausforderung. Die modernsten Tracking-Technologien wie optische Tracker, elektromagnetische Trackingsysteme oder intraoperative Bildgebungsmodalitäten sind für diese Aufgabe ebenfalls ungeeignet, da sie alle Mängel aufweisen. Faseroptische Formerfassungslösungen sind vielversprechend, und bieten im Vergleich zu anderen Verfolgungsmodalitäten verschiedene Vorteile und können hochauflösende Formmessungen in Echtzeit liefern. Kommerziell erhältliche Faserformsensoren sind jedoch teuer und haben eine begrenzte Genauigkeit.

In dieser Arbeit schlagen wir zwei kostengünstige Lösungen für Faserformsensoren vor, die auf mehreren Singlemode Fasern mit FBG Arrays und exzentrischen FBGs basieren. Zunächst stellen wir den Herstellungs- und Kalibrierungsprozess von zwei Prototypen zur Formerfassung vor, die auf mehreren Singlemode Fasern mit halbstarren und superelastischen Substraten basieren. Im zweiten Schritt, untersuchen wir den Erfassungsmechanismus von Edge-FBGs, bei denen es sich um exzentrische Bragg Gitter handelt, die aussermittig in den Kern der Faser eingeschrieben sind. Wir stellen einen Deep Learning Algorithmus zur Modellierung von Edge-FBG Sensoren vor, der die Form des Sensors direkt aus dem Signal vorhersagen kann, ohne dass Kalibrierungs oder Formrekonstruktionsschritte erforderlich sind.

Im Allgemeinen kann jede der vorgestellten Lösungen für Faserformsensoren je nach Zielanwendung als geeignetes Trackinggerät verwendet werden. Der entwickelte Fasersensor mit dem halbstarren Substrat hat einen Arbeitskanal in der Mitte und kann kleine Auslenkungen mit einem durchschnittlichen Spitzenfehler von $2.7\,\mathrm{mm}$ genau messen. Der superelastische Sensor ist für die Messung mittlerer bis grosser Auslenkungen geeignet, bei denen ein Spitzenfehler im Zentimeterbereich noch akzeptabel ist. Der Spitzenfehler ist bei solchen superelastischen Sensoren höher als bei halbstarren Sensoren ($9.9\,\mathrm{mm}$ bis $16.2\,\mathrm{mm}$ bei mittleren bzw. grossen Auslenkungen), da es bei substratbasierten Fasersensoren einen Kompromiss zwischen Genauigkeit und Flexibilität gibt. Der Edge-FBG Sensor, der leistungsfähigste Sensormechanismus unter

den untersuchten Faserformsensoren, kann bei komplexen Formen, bei denen die Faser stark ausgelenkt wird, eine Spitzengenauigkeit von etwa $2\,\mathrm{mm}$ erreichen. Die entwickelte Lösung zur Erfassung der Kantenform kann mit den modernsten verteilten Faserformsensoren konkurrieren, die 30 mal mehr kosten.

Chapter 1

Introduction

1.1 Motivation

Minimally invasive surgical procedures (MIS) are delicate operations performed through small incisions or natural openings in the human body. Compared to conventional open surgeries, which require large incisions to provide a full view of the structures or organs involved, MIS are often preferable and offer various benefits. Their key advantages are less trauma, lower risk of infection, and shorter hospital stay and wound healing time [10, 70].

The downside of such procedures includes the restricted workspace, the limited field-of-view, and an excess burden on surgeons' manual dexterity and visuomotor control [70]. With the advent of robot-assisted minimally invasive surgical procedures (RAMIS), manual dexterity, manipulability, and intraoperative image guidance are enhanced, permitting improved clinical uptake of the technology and ensuring better operative safety and consistency [70]. Typical surgical robots, which have enabled enhanced performance in minimally invasive abdominal surgeries, consist of rigid instruments that are straight with a functional articulating tip [38]. Still, specific procedures in areas with no adequate and direct access through tiny incisions to target anatomies are performed using more invasive open approaches [7, 75]. Thus, having small, flexible, strong manipulators that can reach difficult-to-access surgical sites via nonlinear pathways and complete the surgical task with dexterity are greatly beneficial. Such a category of robots is called continuum or snake-like robot [10].

The present work was conducted in the framework of the flagship project MIRACLE (Minimally Invasive Robot-Assisted Computer-guided LaserosteotomE), that aims to develop a robotic endoscope for cutting bones with laser light. The main applications would be in orthopedics, craniomaxillofacial surgery, neurosurgery, otolaryngology, traumatology, and spine surgery. Depending on the target application, the envisioned endoscopic device could be based on continuum or articulated robots. The focus of this PhD project was on continuum robotic tools only.

Continuum robots provide not only curvilinear and flexible access through small incisions, but are also capable of generating large forces at the distal ends to support various operations [10, 24, 56, 77]. They are defined as actuatable structures whose constitutive materials form curves with continuous tangent vectors [10], and include concentric tube robots, active cable/tendon-driven catheters and needles[73], single-backbone and multi-backbone continuum robots, and pneumatically and hydraulically driven continuum manipulators [54, 79].

However, the inherent deformable and snake-like designs of continuum robots make it difficult to accurately estimate their 3D shape during the operation in real-time. Precise, reliable, and closed-loop motion control of continuum robots would make path planning possible and alleviates manipulation safety concerns [81, 85]. Despite extensive model-based research that relies on kinematics and mechanics, accurate shape estimation of continuum robots remains challenging [14, 24, 31, 37, 81]. Alternative emerging techniques in this field for 3D shape reconstruction include optical tracking [1, 2], electromagnetic (EM) tracking [1], intraoperative imaging[76], and fiber optic shape sensing.

Optical trackers are state-of-the-art technology for tracking medical tools and patients inside the operation room (OR). Wireless tracking, reliable measurement, and stable performance are the key advantages of this technology. However, they require a line-of-sight and are best suited to use with large, rigid tools. These limitations make optical trackers unsuitable for navigating continuum robots inside the patient's body.

EM sensors allow intracorporeal tracking, as they do not require a line-of-sight and can be embedded or placed at the tip of flexible tools. EM tracking systems are less accurate than optical trackers and have a smaller working volume. Multiple sensors along the object of interest are often impossible, as the sensors must be wired. Furthermore, they are sensitive to environmental EM interferences (*e.g.,* the EM field of the robot) and to the presence of conductive or ferromagnetic metals.

Intraoperative imaging modalities, including fluoroscopy, cone-beam CT, and ultrasound, can be an alternative to EM sensors for intracorporeal tracking. Some imaging modalities like biplane fluoroscopy achieve even higher accuracy than EM sensors, but are challenging to perform in crowded OR settings. In addition, they have limitations such as high doses of radiation (*e.g.,* X-ray-based imaging) and high computational cost (*e.g.,* cone-beam CT). Although ultrasound imaging tools are safe and less expensive, they have poor resolution and cannot penetrate through air or bone.

Fiber optic shape sensors are a game-changing technology with many advantages over other tracking modalities. They are immune to EM fields and require no line-of-site. Fiber shape sensors are small in diameter, easily integrable into flexible instruments, biocompatible, highly flexible, and can provide high-resolution shape measurements in real-time. Shape sensors based on multicore fibers have been on the cutting edge of fiber shape sensing and are commercially available. They can measure quasi-distributed or distributed off-axis strain, which is then used for reconstructing the fiber's shape [12].

In quasi-distributed fiber sensors [35], arrays of co-located sensing elements like fiber Bragg grating (FBG) are inscribed inside the cores of a multicore fiber. These sensors require a fan-out device for reading the signal from the cores and a multichannel FBG interrogator for monitoring the Bragg wavelength, making them expensive navigation solutions. Another limitation is the shape reconstruction algorithms that calculate the fiber's 3D shape from the measured strain at discrete points. Low spatial resolution (usually around $1\,\mathrm{cm}$ [6]) and inaccuracies in strain measurement cause an accumulative error in shape reconstruction.

In distributed sensors, off-axis strain is measured from Rayleigh scatterings that naturally occur in optical fibers and are caused by refractive index fluctuations. Multicore distributed sensors are intensity-based and need a complex optical reflectometer for analyzing their signal. Although such sensors can perform high-resolution strain measurements, their overall cost is high and yet are limited by the accumulative error in shape reconstruction.

In light of the former considerations, no comprehensive technology is available for tracking continuum robots in RAMIS. Therefore, there is still room for developing cost-effective and accurate shape sensing solutions based on optical fibers.

1.2 Contribution

Within the scope of this thesis, we investigated two cost-effective fiber shape sensing solutions based on multiple single-mode fibers with FBG arrays and eccentric FBGs and evaluated their benefits and limitations.

In the multiple single-mode fiber design, the sensor probe consists of three single-mode fibers with FBG arrays, which are attached on the surface of a cylindrical substrate. We made two prototypes with semi-rigid and super-elastic substrates and evaluated the sensors' performance in small and large deformation conditions.

The second sensing mechanism is based on eccentric FBGs that are localized fiber Bragg gratings inscribed off-axis in the fiber's core. Edge-FBGs, designed by our collaborators at the Fiber Optical Sensor Systems department in Fraunhofer HHI in Germany, are specific types of eccentric FBG sensors with great potential for shape sensing applications. These sensors can be categorized as intensity-based shape sensors that do not require expensive and complex interrogation systems. Although edge-FBG sensors offer many advantages, accurate shape estimation in such sensors is still an open question, which we have addressed in this thesis. We developed a deep learning algorithm that directly estimates the sensor's shape given the full spectrum of the edge-FBG array. We designed a data acquisition setup to provide the deep neural networks with training samples. We investigated various network architecture designs for the deep learning algorithm and achieved a shape prediction accuracy that competes with the state-of-the-art distributed fiber shape sensors that cost 30 times more.

1.3 Outline

In Chapter 2, the essential scientific background in optical fiber sensors and deep learning techniques is provided for the reader to understand the main concept of this thesis. Subsequently, research publications emerging from this project are presented in Chapters 3 to 7. Chapters 3 and 4 present the working principle, fabrication, and characterization of the first shape sensing solution based on multiple single-mode fibers with semi-rigid and super-elastic substrates. Chapter 5 presents a feasibility study on using a low-cost interrogation system and deep learning techniques for edge-FBG shape sensing. Chapter 6 states a more thorough investigation of using deep learning models with a focus on optimizing the network architecture design and data preprocessing steps. Chapter 7, as the highlight of this thesis, describes the beneficial role of disturbing physical effects in bent optical fibers and investigates how deep neural networks benefit from such effects in edge-FBG sensors and use them as additional sources of information to provide higher spatial resolution shape prediction. Chapter 8 concludes this thesis with an overall discussion of the findings, current limitations, and possible future developments.

Chapter 2

Scientific Background

2.1 Fiber Optic Shape Sensor

2.1.1 Optical Fiber

An optical fiber is a circular waveguide made from dielectric materials with a low optical loss for transmitting guided optical waves. It consists of a central part, the core, surrounded by cladding material. The cladding is covered with a protective layer called coating. The refractive index of the core, which is a number expressing the interaction between the EM wave and the medium, is higher than the cladding, allowing total reflection of most optical rays in the core. Based on Snell's law, the total reflection of light at the interface of two media occurs if the incident angle is greater than the critical angle [25].

The modes of an optical fiber are the possible solutions to Maxwell's equations that satisfy the boundary conditions imposed by the fiber. The general solution form for a monochromatic transverse, propagating wave in a lossless fiber is given by

$$E(x, y, z, t) = E_0(x, y)\ \cos(\beta z - \omega t), \tag{2.1}$$

where,

$$\begin{aligned} \beta &= \frac{2\pi n_{eff}}{\lambda}, \\ \omega &= 2\pi f. \end{aligned}$$

In this equation, $E_0(x, y)$ is the field amplitude distribution in the transverse plane, β is the propagation constant, λ is the optical wavelength, and f is the optical frequency. Depending on the transverse intensity distribution, guided fiber modes can be categorized into the core and cladding modes [65]. Core modes are radiation fields in the core region guided by total internal reflections at the core-cladding interface, and can propagate indefinitely in a lossless fiber. Cladding modes are a portion of the radiation field propagating through the cladding, bounded between the core and the coating [28].

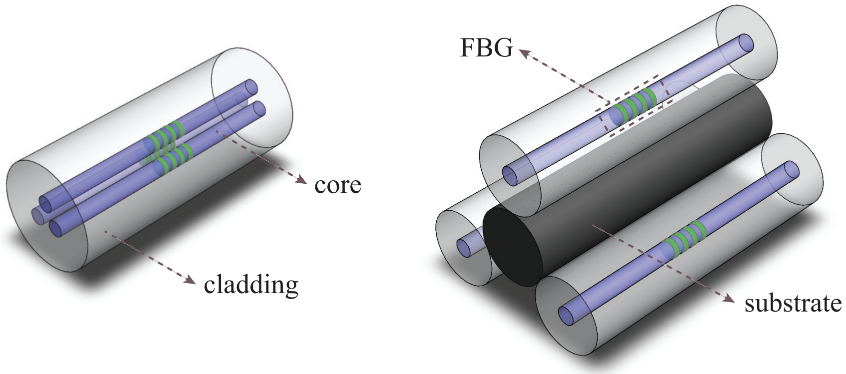

Figure 2.1: A three-core MCF (left) and a multi-fiber shape sensor (right) with one sensing plane.

2.1.2 Optical Fiber Shape Sensing

Fiber optic shape sensors (FOSS) can be categorized into two main groups, multicore fiber (MCF) and multi-fiber sensors [21], shown in Figure 2.1. An MCF is an optical fiber containing more than one fiber core. The FOSSs based on MCFs have very diverse configurations with different angular spacing and number of cores. The most widely used configurations are the MCFs with three [40, 51], four [5, 20] and seven cores [13, 82–84, 90, 91] with constant core spacing. In a multi-fiber sensor, multiple single-mode fibers are epoxy-molded [50] or attached on a cylindrical substrate [36, 40, 42, 57, 80]. Single-mode fibers are specific types of optical fibers in which the core size is small and only one core mode of EM radiation can propagate [25]. When a FOSS is bent, the curvature induces longitudinal strain in the off-axis fiber cores. The generated strain has a linear relationship with the distance between the fiber cores and the sensor's neutral axis. Therefore, the cross-section characteristics of the FOSS dramatically impact the accuracy and the sensitivity of the strain measurement. In FOSS, the shape tracking process consists of three steps: strain measurement, curvature calculation, and 3D shape reconstruction. Commonly used strain measurement technologies in FOSS are based on fiber Bragg grating (FBG) and light scattering, which are briefly explained in Sections 2.1.3 and 2.1.4. Curvature calculation and 3D shape reconstruction are described in detail in Section II of Chapter 4.

2.1.3 Fiber Bragg Grating Sensors

FBG Theory An FBG is a short section of a single-mode optical fiber in which the core refractive index is periodically modulated. Such a structure acts as a wavelength-selective reflection filter, where the peak reflectivity is determined by the phase matching condition (also known as the Bragg condition)

$$\lambda_B = 2n_{eff}\Lambda, \tag{2.2}$$

where λ_B is the Bragg wavelength, n_{eff} is the effective refractive index of the guided mode, and Λ is the period length of the refractive index modulation. Such periodical index-modulated

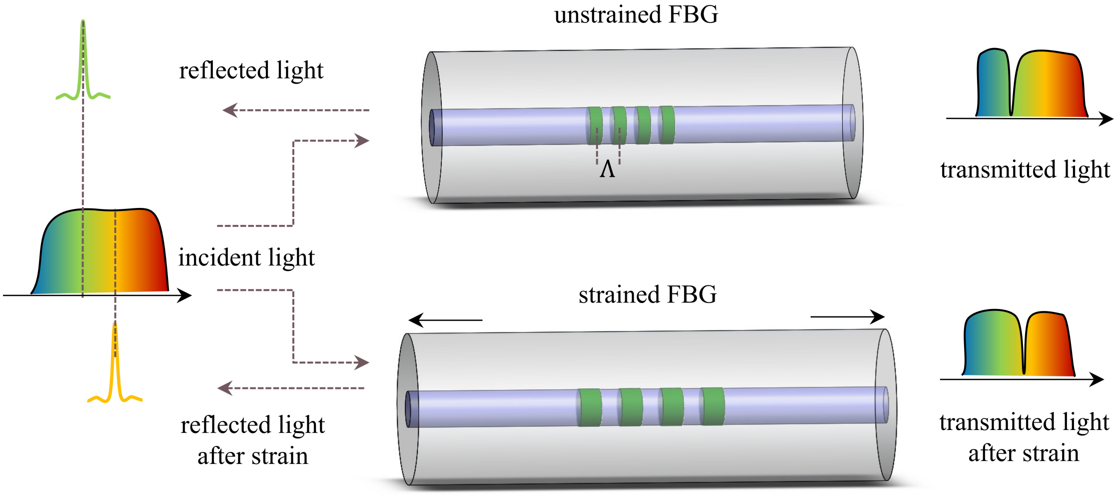

Figure 2.2: FBG working principle. When an FBG structure is under tensile or compression force, the period length of the grating changes, leading to a shift in the reflected Bragg signal.

structures can be achieved by exposing a photosensitive core to intense ultraviolet (UV) interference fringe patterns [87] or by the point-by-point (PbP) inscription using femtosecond (fs) laser pulses [46] (explained in Section 2.2). Typical FBGs, used as strain or temperature sensors, are a few millimeters long and can provide up to 100% peak reflectivity with a reflection bandwidth of $<0.5\,\mathrm{nm}$ [87].

Strain and Temperature Sensitivity of FBGs According to the Bragg condition (Eq. 2.2), the reflecting response of FBGs depends on the grating period (Λ) and the effective refractive index (n_{eff}) that are sensitive to external mechanical or thermal perturbations [87]. Figure 2.2 illustrates the working principle of FBGs. The Bragg wavelength shift $\Delta\lambda_B$ due to strain ε and temperature change ΔT is given by [58, 74]

$$\frac{\Delta\lambda_B}{\lambda_B} = (1 - P_e)\,\varepsilon + (\alpha_\Lambda + \alpha_n)\,\Delta T. \tag{2.3}$$

In this equation, P_e is the strain-optic coefficient, that is, the strain-induced modification of the refractive index. α_Λ is the thermal expansion coefficient, showing the changes in the grating period due to the temperature. α_n is the thermo-optic coefficient, indicating the thermally-induced refractive index changes.

Interrogation Techniques A sequential array of FBGs can be inscribed in the length of one optical fiber, forming multiple sensing planes [32]. An array of FBG sensors can be interrogated by applying a multiplexing technique. The most common interrogation techniques are the time-division-multiplexing (TDM) (Figure 2.3 (a)) and the wavelength-division-multiplexing (WDM)

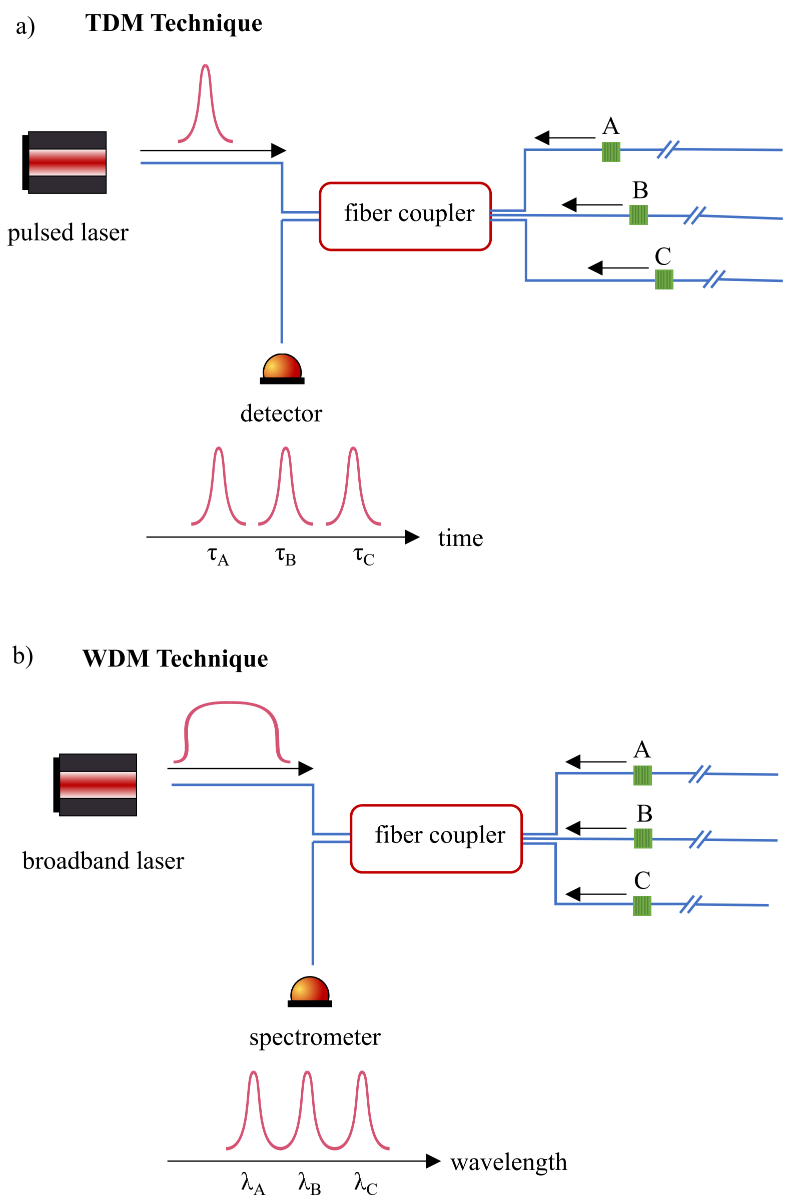

Figure 2.3: The schematics of TDM and WDM techniques are shown in (a) and (b), respectively. Laser pulses in TDM are sent to multiple FBG sensors via a fiber coupler (or an optical switch). All FBGs have the same wavelength, inscribed at fiber locations with different optical path lengths. The reflected Bragg signals from the FBGs have different time delays and can be measured with a fast detector. In WDM, a continuous wave (CW) broadband laser system that covers the Bragg wavelengths of all the FBGs in the fiber sensor is used. The reflected spectrum can be measured using a spectrometer. Alternatively, a swept laser and a fast detector combination is also suitable in the WDM technique.

[12] (Figure 2.3 (b)). In TDM, each FBG has the same Bragg wavelength with low reflectivity, identified by temporal gating of the reflected signals. In the second approach, WDM, each sensor is identified by a unique reflection peak.

FBGs are well-established single-point strain sensors with high sensitivity and accuracy. FBG based strain sensors are low cost and can perform high-frequency data acquisition ($\sim \mathrm{kHz}$) over kilometer range optical fibers. FBGs are considered as quasi-distributed strain sensors, as at least $1\,\mathrm{cm}$ distance is needed between the sensing planes. Such sensors are unsuitable for detecting complex shape deformations requiring high spatial resolution strain measurement.

2.1.4 Scattering-based Strain Measurement

Light scattering is a physical process that describes how localized non-uniformities force the propagating light in a medium to deviate from a straight trajectory into a new direction with a different intensity. Rayleigh and Brillouin scatterings are two kinds of scattering effects that show strain sensitivity. Brillouin scattering is inelastic scattering of the incident light, caused by thermally generated acoustic vibrations [92] or excited vibrational modes [9]. In Rayleigh scattering, local fluctuations in the effective refractive index of the optical fiber scatter the EM waves in all directions [9]. The Rayleigh signal can be enhanced by exposing the optical fiber to UV laser [43] or inscribing a continuous grating into the fiber's cores [82, 83]. Scattering-based fiber sensors are considered as distributed sensors with thousands of continuous sensing points along the fiber. Compared to FBG-based strain sensors, distributed sensors have a considerably lower data acquisition rate (an indicative value could be $\sim \mathrm{mHz}/\mathrm{Hz}$). Depending on the optical reflectometry technique used to analyze the sensor's returning light, spatial resolution, strain accuracy, and the sensing range can vary.

Optical Reflectometry It is a method for analyzing the optical light paths and reflection characteristics in optical fibers. Optical time domain reflectometry (OTDR), and optical frequency domain reflectometry (OFDR) are two common optical reflectometry techniques used in distributes fiber sensors.

In OTDR (shown in Figure 2.4), a laser pulse is launched into the optical fiber, and the returning light is analyzed in the time domain. The power changes in the detected signal provide information on the position and magnitude of the strain along the fiber length. Both Rayleigh and Brillouin signals can be analyzed using the OTDR technique, resulting in a large sensing range (up to tens of kilometers) with an accuracy of tens of $\mu\epsilon$ and spatial resolution of a few meters [4, 49, 61]. In the OFDR technique [17] (shown in Figure 2.5), a CW laser beam, whose optical frequency is linearly tuned, is coupled to an optical interferometer, consisting of the reference and the measurement arms. The interference between the scattered light from the measurement arm and the reference arm is recorded using optical detectors [34]. These interference fringes are processed using the Fourier transform into the time domain, in which a map of the reflections as a function of the fiber sensor's length is constructed [66]. This technique provides accurate strain measurements ($\sim\mu\epsilon$) with high spatial resolution (millimeter scale) [4] in the range of $10\,\mathrm{m}$ to $35\,\mathrm{m}$ [4, 49, 88].

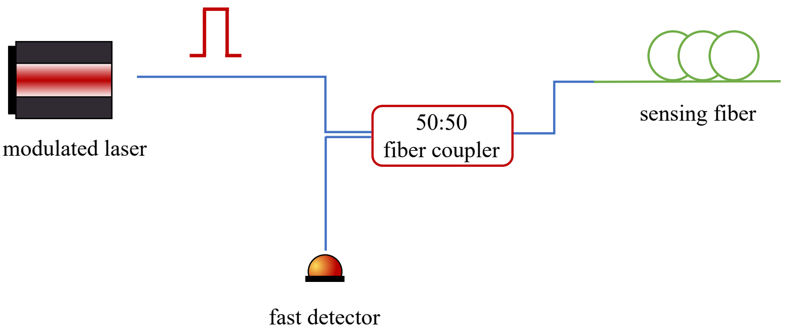

Figure 2.4: Operating principle of OTDR. laser pulses from a modulated laser are sent to the sensing fiber, and the reflected signal's power is measured with a fast detector. Changes in the measured power provide the strain along the fiber length.

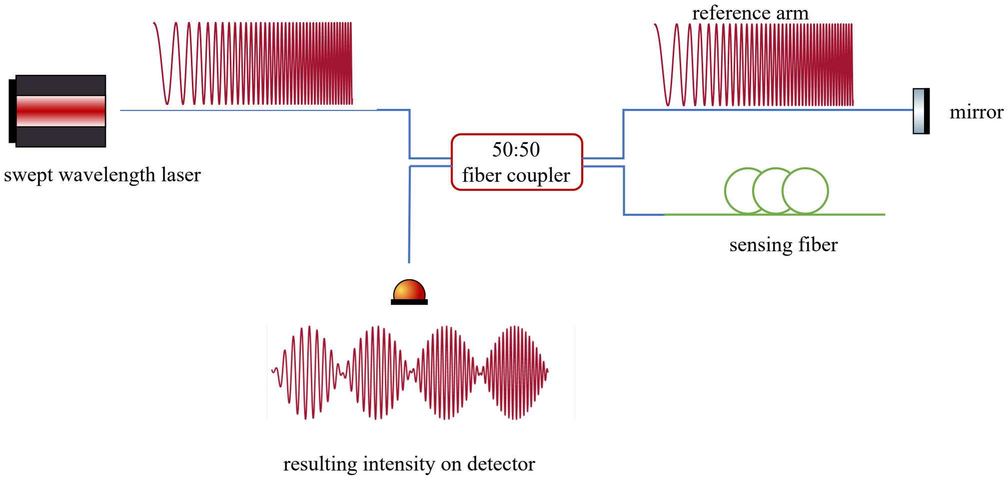

Figure 2.5: Operating principle of OFDR. The beam of a swept wavelength laser is coupled to an optical interferometer, consisting of the reference and the measurement arms. The resulting interference fringes are measured using a fast detector and processed for calculating strain information along the fiber.

2.2 Eccentric FBG Bend Sensors

The advent of PbP FBG inscription using fs infrared laser pulses made it possible to fabricate Bragg gratings in standard optical fibers directly through their coating. This relatively new technology, demonstrated in 2004 [47] for the first time, allows inscribing several highly localized FBGs at any place in the cross-section of an optical fiber. In this technique (Figure 2.6), the optical fiber is illuminated with laser pulses focused at the planned FBG location inside the optical fiber. The induced variations on the refractive index will be periodical when the fiber is moved at a constant speed along its optical axis, and the laser pulses are repeated at a constant rate. Benefiting from such remarkable technological flexibility, Martinez *et al.*, in 2005 [48], developed an optical fiber bend sensor based on eccentric FBG, a localized Bragg grating in-

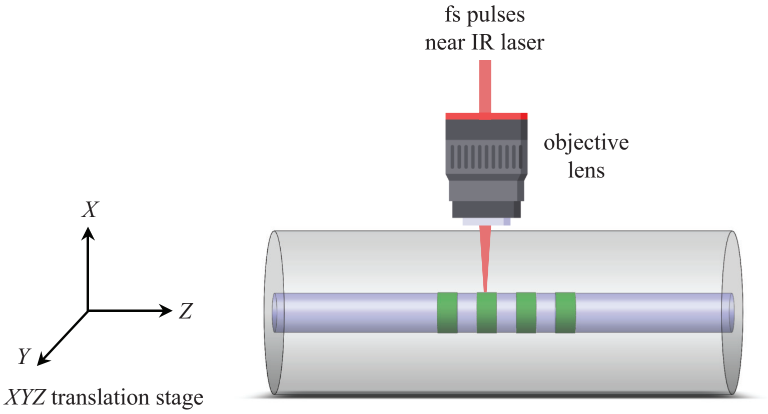

Figure 2.6: A schematic of PbP technique. The fs laser pulses, repeated at a constant rate, are focused at the planned FBG location inside the optical fiber with an objective lens. The fiber is moved constantly using an XYZ translation stage for periodic variations on the refractive index.

scribed off-axis in a fiber's core. However, only the wavelength shift of the designed eccentric FBG was studied during bending. In recent years, the intensity of eccentric FBGs, written in depressed cladding [3] and multi-cladding fibers [11] has also been investigated. The FBGs were inscribed at the core/cladding interface, and the bending sensitivity of coupling from core mode to higher order modes [3] and cladding modes [11] has been studied. These modes are highly sensitive to environmental perturbations and are explained in Section 2.2.3. Waltermann *et al.*, in 2018 [78], proposed a novel curvature sensor based on three co-located FBGs, written around the core of a standard single-mode fiber (shown in Figure 2.7). In this sensor, the curvature and the bending direction are calculated by estimating the centroid of the mode field profile based on the intensity ratio of the reflection peaks from co-located FBGs. This approach is described in more detail in Sections 2.2.1 and 2.2.2. In a curved optical fiber, other effects, including cladding mode coupling, polarization mode dispersion, and bending loss, also modify the intensities at the Bragg peaks. These effects are explained in Sections 2.2.3, 2.2.4, and 2.2.5.

2.2.1 Mode Field Dislocation

The fundamental mode is the main, guided field in single-mode fibers. Considering the propagating wave equation of Eq. 2.1, the fundamental mode has the following field amplitude distribution in the transverse plane,

$$E_0(r) = E_0 \begin{cases} \frac{J_0(ur/a)}{J_0(u)} & 0 \leqslant r \leqslant a, \\ \\ \frac{K_0(vr/a)}{K_0(v)} & r \geqslant a. \end{cases} \tag{2.4}$$

Where, u and v are the propagation and exponential decay constants [30], and J_0 and K_0 are the Bessel and the modified Bessel functions. Due to the similarity between the shape of the guided

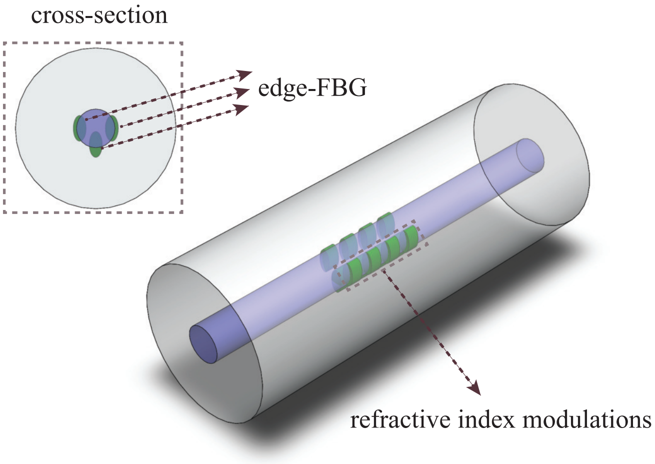

Figure 2.7: An eccentric FBG bend sensor with one sensing plane. Three co-located, highly localized FBGs are inscribed around the core of a standard single-mode fiber.

intensity in the fundamental mode to Gaussian, the field distribution of this mode can also be approximated by a Gaussian function [30, 78]. The field distribution of guided modes changes in curved optical fibers, which can be simulated using the beam propagation method (BPM) [60] in combination with conformal mapping technique [27] (see Figure 2.8). The conformal mapping is a technique for representing a circularly curved fiber by an equivalent straight fiber with modified refractive index distribution [62],

$$n' = n_{stressed}\ \exp\left(\frac{x}{R}\right) \approx n_{stressed}\ \left(1+\frac{x}{R}\right), \tag{2.5}$$

where the $\exp\left(\frac{x}{R}\right)$ accounts for the optical path length increase along the fiber with a distance of x from the curvature's center. The bending is assumed to be relatively small ($x << R$). The $n_{stressed}$ is the refractive index of the bent fiber, which can be calculated through stress-optic effect [33, 71].

$$n_{stressed} = n(1-\varepsilon P_e), \tag{2.6}$$

Where ε is the bending induced strain that can be calculated by $\frac{x}{R}$ [23]. The fiber is compressed along its inner layer ($x < 0$) and under tensile stress along the outer layers ($x > 0$). Substituting Eq. 2.6 into Eq. 2.5 gives

$$\begin{aligned} n' &= n\left(1+\frac{x}{R_{eff}}\right), \\ R_{eff} &= \frac{R}{1-P_e}. \end{aligned} \tag{2.7}$$

Solving the wave equation, adapted according to the modified refractive index distribution, gives the dislocated mode field distribution in the curved area. The mode field dislocation is in the opposite direction of bending (shown in Figure 2.9).

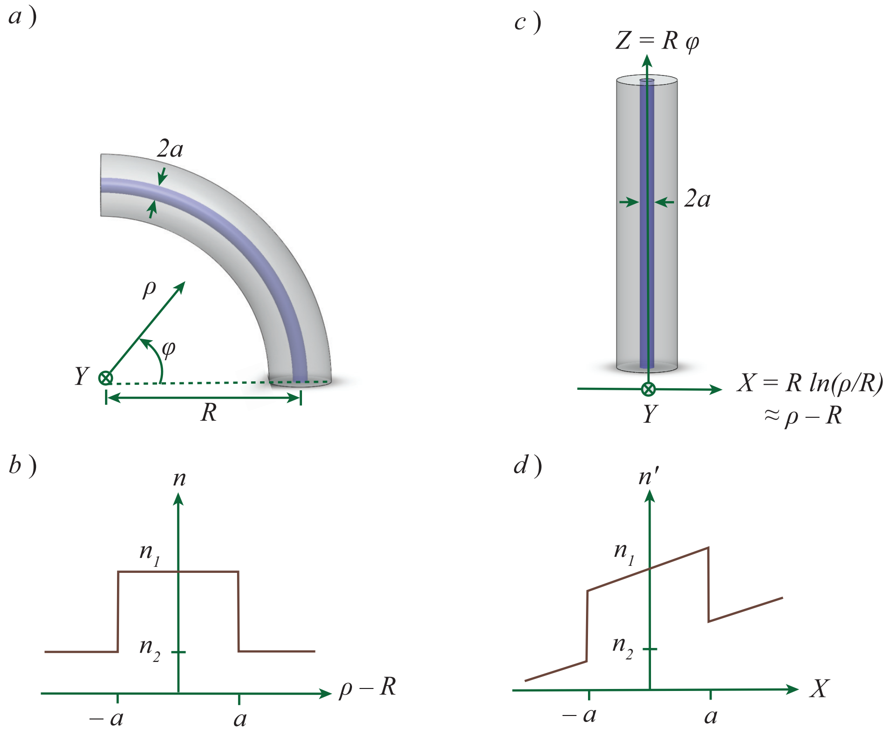

Figure 2.8: Schematic diagram of an unstressed circularly bent fiber (a) and its refractive index distribution (b). The equivalent, straight fiber after conformal mapping (c). The refractive index of the conformal mapped fiber, shown in (d), increases away from the center of curvature. n_1 and n_2 are the refractive indices of the core and the cladding, respectively.

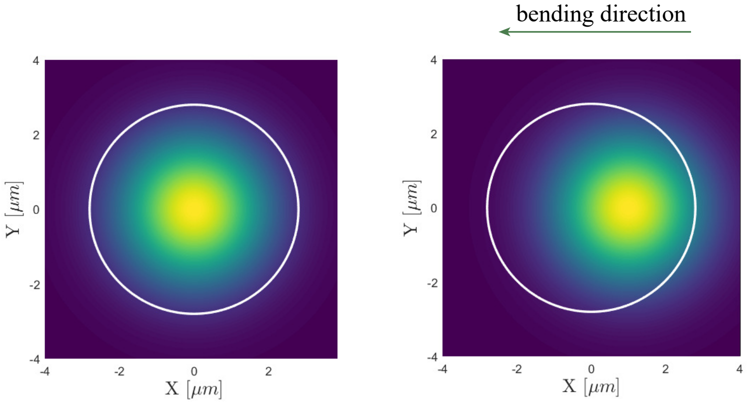

Figure 2.9: The mode field distribution in a straight (left) and bent (right) single-mode fiber. The fiber core is depicted with a white circle.

2.2.2 Shape Sensing Based on Mode Field Dislocation

As mentioned earlier, the field profile of the fundamental mode in a standard single-mode fiber can be mathematically described by a Gaussian distribution with a wavelength-dependent diameter of ω_m. An optimized empiric solution for this approximation is given by [78, 86]

$$\omega_m = a(172.04e^{\frac{(-V+3.412)^2}{2.141^2}} + 1), \tag{2.8}$$

In a curved optical fiber, the centroid of the approximated intensity distribution moves in the opposite direction of bending. This shift can be estimated using $\Delta r = D/R$, where D is a fiber-specific constant that translates the shape deformation to the mode field shift. In edge-FBG sensors, three co-located FBGs measure the intensity of the mode field distribution at three different positions inside the fiber's core. Assuming that the co-located FBGs have the same reflectivity and the incident light has a flat top spectrum profile, the back reflected intensity from the FBGs in a curved fiber can be calculated by

$$I_n = I_0 \, e^{\frac{-[(x_n-\Delta x)^2 + \ (y_n-\Delta y)^2]}{2\omega_m}} \tag{2.9}$$

where, x_n and y_n (with $n = 1, 2, 3$) show the position of the co-located edge-FBGs in the core region. Δx and Δy are the x and y components of the field displacement Δr. Together with Eq. 2.8, the field displacement can be computed

$$\begin{aligned} \Delta y &= \frac{A_{1,2} - A_{2,3}}{C_{1,2} - C_{2,3}} \\ \Delta x &= A_{1,2} + C_{1,2}\Delta y \end{aligned} \tag{2.10}$$

with

$$\begin{aligned} A_{i,j} &= \frac{2\omega_m^2 ln(\frac{I_i}{I_j}) + x_i^2 + y_i^2 - x_j^2 - y_j^2}{2(x_i - x_j)} \\ C_{i,j} &= \frac{y_i - y_j}{x_i - x_j} \ ; \quad i, j = 1, 2, 3. \end{aligned} \tag{2.11}$$

The bending direction ϕ and radius of curvature R can be estimated using the calculated field displacement

$$\begin{aligned} R &= \frac{D}{\sqrt{\Delta x^2 + \Delta y^2}}, \\ \phi &= \tan^{-1}(\frac{\Delta y}{\Delta x}). \end{aligned} \tag{2.12}$$

Similar to the aforementioned FOSS, the 3D shape of the edge-FBG sensors can then be reconstructed using the methods described in Section II of Chapter 4.

2.2.3 Cladding Modes

Cladding modes are 3D field patterns of propagating waves in the core/cladding regions of an optical fiber. In cylindrical coordinate system (r, ϕ, z), the electric field E of the cladding modes inside the core are expressed in terms of the Bessel functions J_n [68]:

$$\begin{aligned} E_z &= E_{lm}\,\frac{u_1^2}{\beta}\,P\,J_l(u_1 r)\,\sin(l\phi+\phi)\,e^{i(\beta z-\omega t)}, \\ E_r &= iE_{lm}\,\frac{u_1}{2}\,[(1-P)\,J_{l-1}(u_1 r)+(1+P)\,J_{l+1}(u_1 r)]\,\sin(l_\phi+\phi)\,e^{i(\beta z-\omega t)}, \\ E_\phi &= iE_{lm}\,\frac{u_1}{2}\,[(1-P)\,J_{l-1}(u_1 r)+(1+P)\,J_{l+1}(u_1 r)]\,\cos(l_\phi+\phi)\,e^{i(\beta z-\omega t)}, \end{aligned} \tag{2.13}$$

In these equations, l and m are the azimuthal and radial integer indices, n_1 is the refractive index of the core, $u_1 = (2\pi/\lambda)\sqrt{n_1^2 - n_{eff}^2}$ is the transverse wave vector, Z_0 is the EM impedance in vacuum, and P is the mode parameter. Cladding modes can get excited using fiber gratings that provide inter-mode coupling and convert the core mode energy into cladding modes. In conventional FBGs, with uniformly modified core's cross-section, only the lowest azimuthal order of cladding modes is excited [18]. Higher azimuthal orders, that are more sensitive to directional bending, can be excited with tilted [39] or highly localized eccentric [68, 69] FBGs. In PbP written eccentric FBGs, the induced refractive index change is determined solely by the focusing geometry of the fs laser pulses. These types of FBGs can create very strong (up to 25dB) cladding mode coupling [68]. An example of strong cladding mode resonances in eccentric FBGs is shown in Figure 2.10). More information on modeling spectral properties of localized (eccentric) FBGs can be found in [69].

Using the coupled mode equations, adapted for FBGs [18], the coupling constants between the fundamental mode and the cladding modes can be computed. These equations evaluate an overlap integral between the interacting modes with the FBG. In case of Bragg grating perturbations, the coupling associated with longitudinal field components is negligible. The transverse coupling constant, determining the coupling of the incoming fundamental mode to reflected

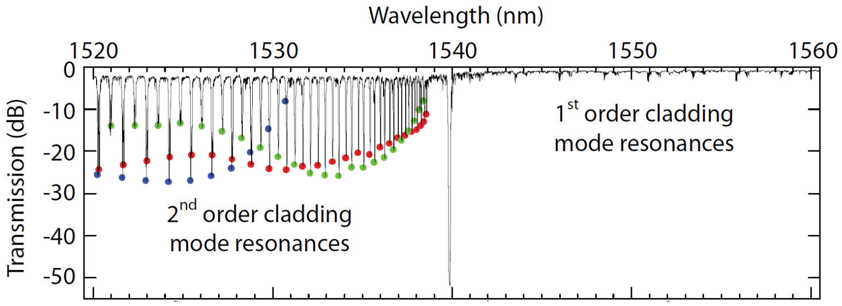

Figure 2.10: Transmission spectrum of a PbP-written grating at 1540 nm that shows strong cladding mode resonances. The colored dots indicate the envelopes of three resonances, $HE_{l=1}$ (red), $EH_{l=1}$ (blue), and $HE_{l=2}$ (green). Courtesy of [68], reprinted and modified with permission of the author, © [2011] Optics Express

modes, is calculated by [68]

$$\kappa_{lm} = \frac{4}{\pi\nu}\,\frac{\omega}{4}\int_0^{2\pi} d\phi \int_0^{\inf} dr\; r\; \Delta\varepsilon(r,\phi)\; \mathbf{E}_{11}(r,\phi)^T.\; \mathbf{E}_{lm}(r,\phi)^{T*}, \tag{2.14}$$

where $\mathbf{E}_{11}(r,\phi)^T$ is the transverse electric field of the fundamental mode that can be approximated by a Gaussian function [25, 30], $\mathbf{E}_{lm}^T$ indicates the transverse electric field of the reflected mode (Eq. 2.13), and ν is the FBG reflection order. The perturbation dielectric constant $\Delta\varepsilon(r,\phi)$ is induced by refractive index modifications of the FBG. The coupling strength highly depends on the overlap integral in Eq. 2.14 and can be enhanced or reduced as the optical fiber is bent [15, 28, 89]. This is due to bending-induced modifications in the effective refractive index and the overlapping changes between core and cladding mode fields [3, 63].

2.2.4 Polarization of Light

The polarization of the transverse EM wave indicates the oscillation orientation of its electric field component. Considering a monochromatic plane wave with an angular frequency of ω propagating in the z direction, a general expression of the electric field is given by [59]

$$\mathbf{E}(z,t) = E_x\hat{x} + E_y\hat{y}, \tag{2.15}$$

where E_x and E_y are the x and y components of the electric field vector [16, 59]:

$$\begin{aligned} E_x(z,t) &= E_{0,x}\,\cos[\omega t - kz + \varphi_x],\\ E_y(z,t) &= E_{0,y}\,\cos[\omega t - kz + \varphi_y]. \end{aligned} \tag{2.16}$$

The amplitudes ratio of $E_{0,y}$ and $E_{0,x}$, and the phase difference $\Delta\varphi = \varphi_x - \varphi_y$ determine the light polarization state. For instance, if the phase difference is 0 or π the light is considered linearly polarized in the direction of $\tan^{-1}(E_{0,y}/E_{0,x})$.

When a light wave propagates in a birefringent medium, where the refractive index is orientation-dependent, the light propagation velocity is different in each traveling direction. This means that the phase difference between the electric field components changes as the EM wave passes through the birefringent medium, modifying its polarization state accordingly [16],

$$\Delta\varphi = \frac{2\pi}{\lambda}\,\Delta n_{eff}, \tag{2.17}$$

where Δn_{eff} is the difference between the effective refractive indices in x- and y-directions. Figure 2.11 illustrates how the polarization state changes in a birefringent medium.

An ideal optical fiber is a homogeneous isotropic medium exhibiting the same refractive index for both electric field components (E_x and E_y). However, in reality, optical fibers do not have a constant circular cross-section and exhibit anisotropy under mechanical stress. Consequently, optical fibers behave as a birefringent medium with different refractive indices in x- and y-directions. Bending an optical fiber induces linear birefringence, caused by mechanical stress on the cladding (illustrated in Figure 2.12). Due to the photo-elastic effect [8, 33, 64, 71], the bending-induced pressure, imposed on the core, increases the refractive index in the bending

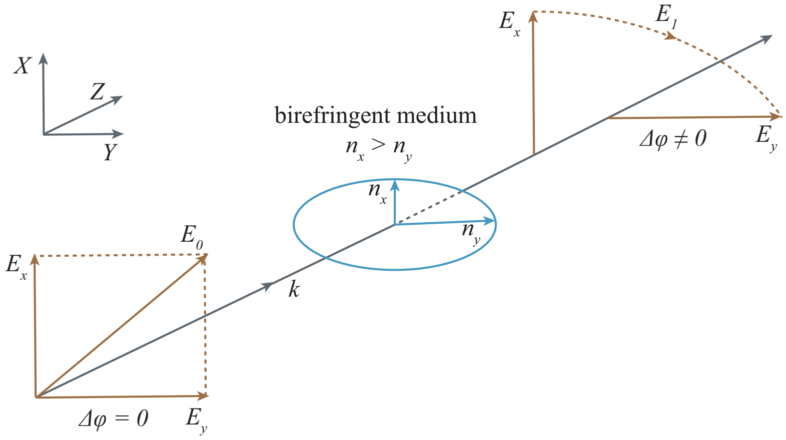

Figure 2.11: Linearly polarized electric field component E_0 passes through a birefringent medium. The resulting phase shift modifies its polarization state.

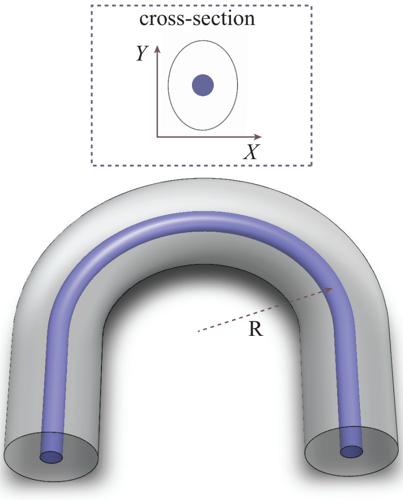

Figure 2.12: Bending-induced mechanical stress on the cladding region imposes pressure on the fiber's core and increases the refractive index in the bending direction (the X-axis).

direction, resulting in a change of $\Delta n_{eff} = \varepsilon P_e$ in the effective refractive index (using Eq. 2.6). This phase shift $\Delta\phi$ is wavelength-dependent, consequently, the polarization state changes differently at each wavelength. This effect is known as polarization mode dispersion (PMD) [22].

2.2.5 Bending Loss

As mentioned, bending an optical fiber changes its guiding properties by modifying the refractive index and reshaping the guided field. When the optical fiber is bent, the guided field moves in the opposite direction of bending and can escape the fiber. This attenuation is known as bend

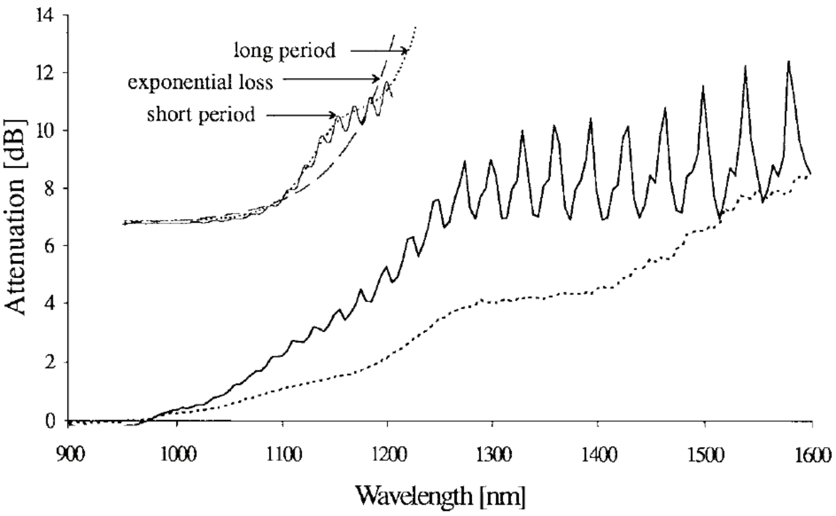

Figure 2.13: Spectral bend losses of a standard optical fiber (York LB800), curved at a curvature radius of $21.5\,\mathrm{mm}$ with bend arc of 18°. Courtesy of [19], reprinted with permission of the author, © [1997] IEEE.

loss. Such bending-induced perturbations in the mode field distribution can excite leaky modes that are propagating-radiating fields reflected by cladding-coating or coating-air interfaces [19]. These coherent couplings between the core and leaky modes appear like modulation patterns in the spectral bend loss [19]. A typical trend of spectral losses showing the bending loss oscillations is shown in Figure 2.13. The short-period modulation is due to the reflected field at the coating-air interface, while the long-period one is caused by reflections at the cladding-coating interface [26, 52, 53, 67].

In the literature, different models have been proposed for evaluation of bend loss oscillations [26, 53, 55, 72]. However, the most general expression explaining such spectral attenuation is reported by Faustini *et al.,* [19]. Following the same conformal mapping, explained in Section 2.2.1, the scalar wave equation is transformed to the local Cartesian coordinate with the equivalent straight fiber. Neglecting the coating-air interface, the transformed scalar wave equation in the cladding and coating regions is given by [19]

$$\frac{d^2\tilde{\psi}_q(x,\zeta)}{dx^2} + \left[k^2 \acute{n}_q^2 - \beta_0^2 - \zeta^2\right]\tilde{\psi}_q(x,\zeta) = 0, \tag{2.18}$$

where $\tilde{\psi}_q(x,\zeta)$ is the Fourier transform of the transverse field component $\psi_q(x,y)$ in core and cladding regions (with $q = 2,\ 3$, respectively). $\acute{n}_q$ is the modified refractive index distribution (from Eq. 2.5), assuming that the stress-optic effect is negligible. k is the vacuum wavenumber, given by $2\pi/\lambda$, and β_0 in the unperturbed propagation constant of the fundamental mode in straight fiber. The solution of Eq. 2.18 gives the evanescent field in cladding and coating regions. The bend loss coefficient can be computed once the bending-induced variation of the propagation constant ($\delta\beta$) is calculated using the interaction of the unperturbed incident field with the evanescent field,

$$\begin{aligned} 2\alpha &= -2\, Im(\delta\beta) \\ &= -2\, \frac{k^2}{\beta\, V^2\, K_1^2(\alpha\gamma)}\, Im(\rho). \end{aligned} \tag{2.19}$$

$V = ka\sqrt{n_1^1 - n_2^2}$ is the normalized frequency in which, a is the core radius and n_1 and n_2 are the core and cladding refractive indices, respectively. ρ is the amplitude of the backward evanescent field. The reader is referred to [19] for more details.

2.3 Deep Learning

2.3.1 Neural Network

Deep learning is a practice of using algorithms that are inspired by biological neural networks to analyze nonlinearly separable data. Such structures are called artificial neural networks and, similar to the nervous system of the human brain, consist of neurons (also known as perceptrons) that are arranged into various layers. These algorithms are trained using large datasets containing a pair of input and corresponding output data to perform a specific task. Feedforward neural networks are popular types of neural network in which the information moves in one direction, and the output of each layer serves as the input for the next layer(s). The first layer in a feedforward neural network is the input layer that receives the data (depicted in Figure. 2.14). The last layer is the output layer that gives the problem solution. The intermediate layer(s) are called hidden layers that receive raw information from the input layer and process them before sending them to the output layer. The number of hidden layers defines the networks' depth. A deep neural network is a many-layered network that can learn higher-level features from the input data and perform better than traditional machine learning techniques. A convolutional neural network (CNN) is a feedforward deep neural network class that is quite effective in detecting objects and recognizing patterns in image and non-image data, such as audio and signal data. The hidden layers in the architecture of a CNN include convolutional layers that perform convolution operations on each subset of neurons.

2.3.2 Hyperparameter Tuning

In deep learning problems, the learning process is controlled by hyperparameters. The values of these parameters are not learned during training and impact the model architecture, the amount of regularization, and the learning rate. Hyperparameters must be set by optimization techniques such that the algorithm's performance generalizes to new, unseen data. Search methods for hyperparameter optimization problems include two main steps, hyperparameter configuration selection, and configuration evaluation. Hyperband [41] is a well-known optimization algorithm that randomly samples hyperparameter configurations, adaptively allocates resources (*e.g.,* number of iterations, or size of the training set), and invokes Successive Halving [29]. In the Successive Halving algorithm, resources are uniformly allocated to a set of hyperparameter

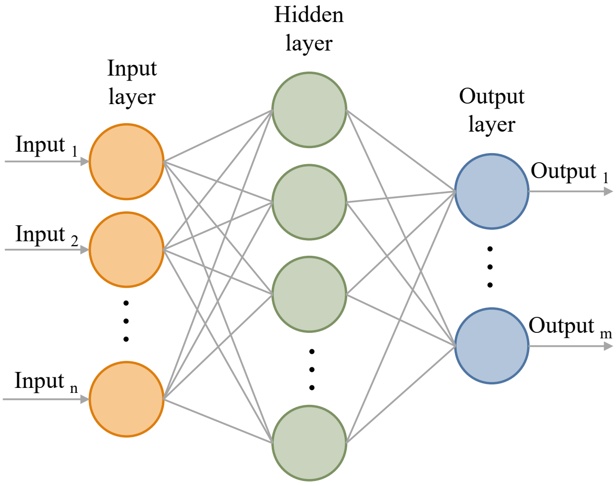

Figure 2.14: A neural network consists of three types of layers, input, hidden, and output layers. The input layer receives the input data and transfers it to the hidden layer/s for feature extraction. The output layer maps the extracted feature to the desired output.

configurations, and after performance evaluation, the worst half of the configurations are thrown out. This process is repeated until one configuration remains.

The Hyperband algorithm consists of two loops; the inner loop applies extended Successive Halving for a fixed number of configurations and minimum resource allocation, and the outer loop iterates over different combinations of the number of configurations and the resources. Compared to the original Successive Halving algorithm, in the inner loop of the Hyperband, the proportion of configurations discarded in each round is three by default and can be adjusted to the desired value. Hyperband can evaluate an order-of-magnitude more configurations in a shorter time compared to black-box procedures (*e.g.,* Bayesian optimization algorithms)

Chapter 3

Temperature-Compensated FBG-Based 3D Shape Sensor Using Single-Mode Fibers

The publication presented in this chapter briefly describes the fabrication, calibration, and evaluation of an FBG-based multi-fiber shape sensor. The substrate used in the presented shape sensing solution is semi-rigid, suitable for shape measurement in small deformation conditions with curvature levels of $0.7\,\mathrm{m}^{-1}$ to $2.5\,\mathrm{m}^{-1}$. The average positioning error is $1.4\,\%$ per unit length of a $20\,\mathrm{cm}$ long sensor, which is equivalent to $\sim 2.7\,\mathrm{mm}$.

Publication. The proposed shape sensing solution was presented in the form of an oral presentation at the Advanced Photonics conference, in July 2018, in Zurich, Switzerland. The following manuscript was published as part of the conference proceedings [45].

This is the accepted manuscript version of the following article:
S. Manavi, L. Witthauer, L. Iafolla, A. Zam, G. Rauter, and P. C. Cattin. Temperature-compensated fbg-based 3d shape sensor using single-mode fibers. In Advanced Photonics 2018 (BGPP, IPR, NP, NOMA, Sensors, Networks, SPPCom, SOF), page JTu6C.1. Optica Publishing Group, 2018.
The final authenticated version is available online at https://doi.org/10.1364/BGPPM.2018.JTu6C.1.

Temperature-compensated FBG-based 3D shape sensor using single-mode fibers

Samaneh Manavi, Lilian Witthauer, Lorenzo Iafolla, Azhar Zam, Georg Rauter, Philippe C. Cattin
Center for medical Image Analysis & Navigation (CIAN), University of Basel, Department of Biomedical Engineering,
Allschwil, Switzerland
samaneh.manavi@unibas.ch

Abstract: We report a temperature-compensated FBG-based 3D shape sensor with an average positioning error of 1.4 %. The sensor consists of three single-mode fibers with four arrays of FBGs, which are glued on a substrate.

OCIS codes: (130.6010) Sensors; (060.2370) Fiber optics sensors; (060.2430) Fibers, single-mode; (060.3735) Fiber Bragg gratings; (280.4788) Optical sensing and sensors.

1. Introduction

Laser osteotomy has shown to have several advantages over conventional bone surgery, such as the possibility of making smart cuts and the faster healing time [1]. The MIRACLE project (funded by the Werner Siemens Foundation, Zug, Switzerland) aims to combine laser osteotomy and endoscopy to improve the benefits for the patient even more. One of the challenges in this project is to have real-time feedback on the exact shape and position of the flexible endoscope inside the body. Shape sensing based on Fiber Bragg Gratings (FBG) has shown to be a promising approach for this task [2], since FBGs are small, immune to electromagnetic noise, easy to replace, and can provide position and shape information along the entire sensor length.

This paper describes the calibration process developed for an FBG-based shape sensor in order to improve the positioning accuracy. In Section 2, the design of the sensor probe and the principle of the shape reconstruction process is presented. Section 3 describes the calibration method and at the end of this paper, the tip accuracy of the fabricated sensor is estimated.

2. Method

The shape sensor is composed of three single-mode fibers with four arrays of FBGs within each. The FBGs were 5 cm apart and attached to a wire-braided Polyimide tube with outer diameter of 1.05 mm at 120 degrees using a highly flexible glue. A broadband light source is used to cover the Bragg wavelength of all the FBGs from 1515 nm to 1585 nm. The reflected signal is then detected with a fast spectrometer (I-MON 512, Ibsen) for further analysis.

The strain E_i in fiber i as a function of the bending angle θ and the curvature k is described by the following equation system:

$$E_1 = E_t + kd_1 \sin\theta \quad (1)$$

$$E_2 = E_t + kd_2 \sin(\theta + \theta_{12}) \quad (2)$$

$$E_3 = E_t + kd_3 \sin(\theta + \theta_{13}) \quad (3)$$

$$E_i = \frac{1}{\alpha}\frac{\Delta\lambda_i}{\lambda_i} \quad (4)$$

where E_t is the strain due to temperature, θ_{ij} is the angle between the fiber i and j, and d_i is the distance between the fiber and the neutral axis. The 3D shape information can be provided along the sensor, by numerically solving the Frenet-Serret equations using the Runge-Kutta method.

3. Calibration and Characterization

Since changes in temperature, curvature, and bending angle will all lead to a shift of the Bragg wavelength, a calibration was done separately for all these parameters. For the temperature calibration, the sensor was placed inside a temperature-controlled enclosure without being bent. The time-dependent temperature and the wavelength shifts were studied in the frequency domain which helped to improve the reliability of the calibration procedure even if the data acquisition was not synchronized or the thermocouples were not attached to the FBGs properly. The calibration has shown that the glue had a large effect on the thermal sensitivity of the sensor in such a way that in 1550 nm-FBG for instance, the thermal sensitivity increased from 14.18 pm/°C to 48.62 pm/°C after gluing. The thermal sensitivity was also seen to vary depending on the amount of glue used.

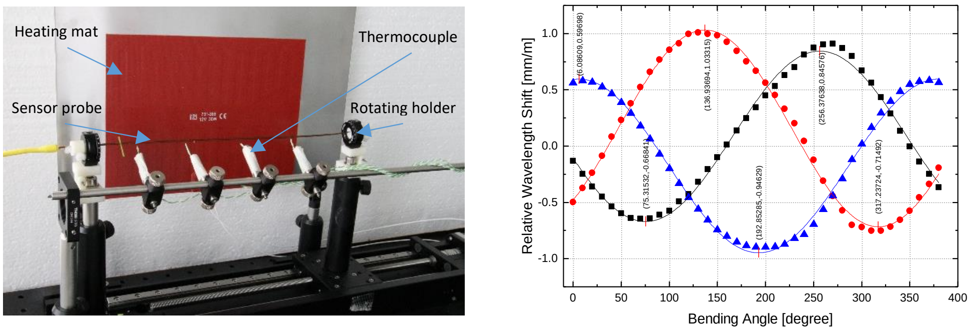

Fig. 1. Left: calibration setup. Right: the sinusoidal dependency of the relative wavelength shift to the bending direction.

The calibration setup is shown in Fig. 1 on the left-hand side. The sensor was mounted on two rotating holders, which were attached to 3D-printed hinges. The inlet of the sensor was fixed to the table while the tip was placed on a motorized linear stage. In order to obtain the exact mounting angles θ_{ij} between the fibers (due to the gluing process there was a deviation from the designed 120 degrees), the sensor was positioned at a fixed curvature in the setup and the Bragg wavelength shifts were measured for different bending directions by rotating the sensor holder in steps of 10 degrees. The resulting sinusoidal dependency of the relative wavelength shift in the first sensor plane to the bending angle is shown in Fig. 1 on the right-hand side. The mounting angles θ_{ij} were directly deduced from the phase shifts between these curves. The same measurement was repeated for different bending radii and the amplitude of the sine wave was extracted for each FBG. The resulting calibration curve for the FBG at 1515 nm is shown in Fig. 2 (left) together with a linear fit. The slope of this line is related to the strain-optic coefficient, the strain transfer, and the distance between the fiber core and the neutral axis (αd_i). As the Bragg wavelength changes with room temperature, one should first correct the measured wavelength using the thermal sensitivity coefficient, and then use it for shape reconstruction.

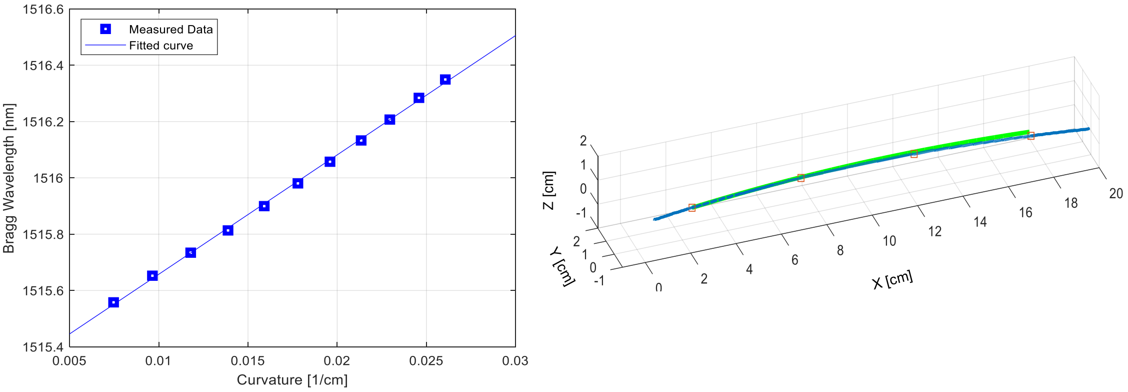

Fig. 2. Left: calibration curve of 1515 nm-FBG at 25.5°C. Right: the real shape (blue) and the reconstructed shape (green) of the sensor

To evaluate the stability of the sensor when the applied mechanical strain is constant, the output signal was recorded for a few days. The reflected wavelength had some fluctuations, which are due to the temperature variations. There is also a trend in the output signal caused by the glue, as it keeps the heat for a longer time.

4. Results

Using the above obtained calibration parameters, the reconstructed 3D shape resulted in error of 1.4 % as shown in Fig. 3. We believe that this reconstruction quality is strongly limited by the calibration setup, and in the future work we will apply some optimization in the calibration process.

6. References

[1] Kyung-won Baek, Waldemar Deibel, Dilyan Marinov, Mathias Griessen, Michel Dard, Alfredo Bruno, Hans-Florian Zeilhofer, Philippe Cattin, Philipp Juergens, “A comparative investigation of bone surface after cutting with mechanical tools and Er:YAG laser”, Lasers in Surgery and Medicine, Volume 47, Issue 5, PP. 426-432, 2015

[2] Seok Chang Ryu, and Pierre E. Dupont, “FBG-based Shape Sensing Tubes for Continuum Robots,” IEEE, pp. 3531-3537, 2014

Chapter 4

Fabrication and Characterization of a Flexible FBG-Based Shape Sensor Using Single-Mode Fibers

The publication presented in this chapter describes the fabrication, calibration, and evaluation of a $20\,\mathrm{cm}$ long shape sensor based on multi-fiber FBG arrays attached on a super-elastic substrate. The presented shape sensing solution is able to detect medium to large deflections (in the curvature range of $0.04\,\mathrm{m}^{-1}$ to $8.7\,\mathrm{m}^{-1}$) with a median tip error of $9.9\,\mathrm{mm}$ to $16.2\,\mathrm{mm}$. Our observations showed that, in such sensor configurations, there is a trade-off between the shape prediction accuracy and the sensor's flexibility. This is because the bending stiffness at the sensor's cross-section is no longer uniform, and random twisting effects can occur during bending. We designed a generalized model for curvature and torsion prediction in such a non-uniform sensor configuration. We also investigated two shape reconstruction methods, the Frenet-Serret formula and the kinematic model, and believe that the latter approach is better suited for such sensor design.

Publication. The following manuscript was published in the journal of *IEEE Transactions on Biomedical Engineering* (IEEE TBME) on the 1st of February 2022 [58].

This is the accepted manuscript version. The final authenticated version is available online at https://doi.org/10.1109/TBME.2022.3148040.

Fabrication and Characterization of a Flexible FBG-based Shape Sensor using Single-mode Fibers

Samaneh Manavi Roodsari*, Sara Freund, Azhar Zam, Member, IEEE, Georg Rauter, Member, IEEE,
Philippe C. Cattin, Member, IEEE

Abstract— **Minimally invasive surgical procedures have become the preferable option, as the recovery period and the risk of infections are significantly lower than traditional surgeries. However, the main challenge in using flexible tools for minimal surgical interventions is the lack of precise feedback on their shape and tip position inside the patient's body. Shape sensors based on fiber Bragg gratings (FBGs) can provide accurate shape information depending on their design. One of the most common configurations in FBG-based shape sensors is to attach three single-mode optical fibers with arrays of FBGs in a triangular fashion around a substrate. Usually, the selected substrates dominate the bending stiffness of the sensor probe, as they have a larger diameter and show less flexibility compared to the optical fibers. Although sensors with this configuration can accurately estimate the shape, they cannot be implemented in flexible endoscopes where large deflections are expected.**

This paper investigates the shape sensor's performance when using a superelastic substrate with a small diameter instead of a substrate with dominating bending stiffness. A generalized model is also designed for characterizing this type of flexible FBG-based shape sensor. Moreover, we evaluated the sensor in single and multi-bend deformations using two shape reconstruction methods.

IndexTerms— **Minimally invasive surgery, optical fiber shape sensing, sensors for flexible endoscope, fiber Bragg grating (FBG), fiber sensor characterization.**

I. INTRODUCTION

Laser osteotomy, compared to conventional mechanical bone surgery, allows small, functional, and precise cuts based on pre-operative planning. When laser osteotomy is combined with endoscopy (minimally invasive surgery), the healing process will be accelerated, and the risk of infection and trauma will be reduced for the patient [1], [2]. However, permanent damage may happen to patients if the shape or tip position of the endoscope is not estimated correctly. Many studies were reported in the literature on using different tracking technologies during the surgery [3]–[5]. Still, they all have shortcomings like electromagnetic (EM) sensitivity (EM sensors), limited resolution (ultrasound imaging), low speed (MRI), or require high doses of radiation (X-ray or CT imaging) [6]. FBG-based shape sensors have received considerable attention in recent years. These sensors are easily integrable into medical instruments as they are bio-compatible and have small diameters. Unlike EM sensors, FBG-based shape sensors are not sensitive to the presence of conductive or ferromagnetic materials and are immune to EM disturbances [7]. These advantages make FBG shape sensors ideal candidates for enabling a closed-loop control system when using elastic structures in clinical applications such as catheter navigation, surgical needle tracking, and medical robotic navigation.

Commercially available FBG shape sensors are mainly based on multicore fibers. However, due to the short distance between the sensing elements and the neutral axis (often less than 100 μm), the sensor can only detect deformations with bending radii below 10 cm [8], and therefore, are limited to the applications where only large deflections are expected. At the same time, the cost of such systems is high [9] due to the optical frequency domain reflectometer (OFDR) used for FBG interrogation [10] and a fan-out device to read out the signal from the cores [11].

Shape sensors made from multiple single-mode fibers are more cost-effective as expensive custom-made fan-out devices are replaced by standard fiber couplers. To create such a bundle, the optical fibers can either be directly glued together [12], embedded in a grooved cylindrical base [6], molded into flexible materials [13], or attached on a cylindrical substrate [7], [14], [15]. Shape sensors based on these different designs present various benefits and drawbacks and are a tradeoff between flexibility and accuracy. For instance, although gluing the optical fibers together is simple and straightforward, the middle area is filled with extra adhesive, which lowers the mechanical flexibility [12] and may increase the thermal sensitivity of the sensor. Moreover, these sensor structures have a non-circular cross-section with different bending stiffness for each direction, leading to preferred bending angles for the sensor. In embedded FBG arrays, the sensor has a circular cross-section, and therefore, the bending stiffness asymmetry is negligible, and the sensor is mechanically more stable. However, these sensors can only tolerate small tip deflections

---

Manuscript received August 09, 2021; revised December 25, 2021; accepted January 18, 2021. This work was supported by the Werner Siemens Foundation.

Samaneh Manavi Roodsari, Sara Freund, and Philippe C. Cattin are with the CIAN in the Department of Biomedical Engineering, University of Basel, Allschwil, Switzerland (correspondence e-mail: samaneh.manavi@unibas.ch).

Azhar Zam is with the BLOG in the Department of Biomedical Engineering, University of Basel.

Georg Rauter is with the BIROMED-Lab in the Department of Biomedical Engineering, University of Basel.

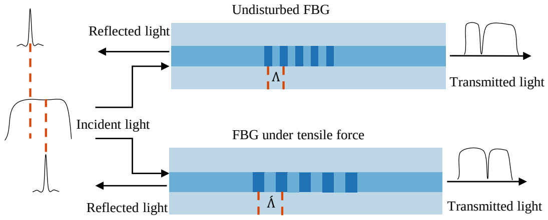

Fig. 1. Working principle of fiber Bragg gratings.

[6], [16], or curvatures up to 2.8 m^{-1} [17] and are mainly used for needle tracking. Molded FBG sensors may improve the sensor's flexibility to detect up to 90° bending [18], but the self-fabrication process is challenging.

Compared to other methods, for optical fibers attached on a cylindrical substrate the maximum reachable curvature of the sensor can be defined based on the stiffness and the diameter of the substrate (usually $>$ 1 mm) [12], [15], [18]–[21]. In our previous work [14], we designed a shape sensor by attaching three single-mode fibers on a wire-braided Polyimide tube with an outer diameter of 1.05 mm and Young's modulus of 24.7 GPa [7]. This sensor was able to detect small deformations in the curvature level of 0.7 m^{-1} with a 1.4% positioning error per unit length of the sensor. Although this sensor had a triangular cross-section, the Polyimide substrate, which had higher stiffness than the optical fibers, protected the sensor from bending preferences. However, due to the low flexibility of the substrate, the sensor was mainly suitable for detecting small curvatures (below 2.5 m^{-1}).

In this contribution, we present a 3D shape sensor based on three single-mode fibers glued on a superelastic Nitinol wire. The small diameter of the substrate and its superelasticity enable achieving larger curvatures and increase the flexibility of the sensor. In this design, the bending stiffness of the sensor is no longer dominated by the substrate, which affects the angular behavior of the sensor. Therefore, standard calibration methods fail to model the sensor. Here we proposed a new technique to model asymmetric and highly flexible sensors, which improves the shape estimation accuracy in these types of sensors.

II. FBG-BASED SHAPE SENSOR WORKING PRINCIPLE

FBGs are periodic structures of different refractive indices inside the core of an optical fiber. They show large reflectivity around a specific wavelength, which fulfills the Bragg condition. The narrow reflected signal, known as the Bragg wavelength, is sensitive to environmental perturbations such as temperature variations and mechanical strain [22]. The Bragg wavelength can be calculated by $2\,n_{eff}\,\Lambda$, where n_{eff} is the effective refractive index and Λ is the period length of the grating. As illustrated in Fig. 1, if the FBG is disturbed, the period length of the grating changes and causes shifts in the reflected signal. The relative Bragg wavelength shift changes linearly with respect to the mechanical strain and temperature variations [19]

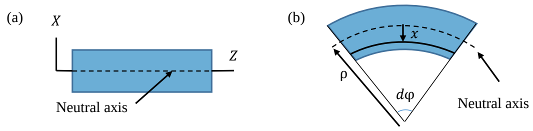

Fig. 2. (a) Bending plane of the beam. (b) Deformation of the beam in pure bending, where $d\varphi$ is the angle of the selected segment.

$$\frac{\Delta\lambda_B}{\lambda_B} = (1 - P_e)\,\varepsilon + (\alpha_\Lambda + \alpha_n)\,\Delta T. \tag{1}$$

In this equation, ε is the relative longitudinal change in the Bragg grating caused by a mechanical strain, and ΔT indicates temperature variations. P_e, α_Λ, and α_n are strain-optic, thermal expansion, and thermo-optic coefficients, respectively. FBG sensors can detect bending deflections if placed away from the centroid. In a beam under pure bending (shown in Fig. 2), where the bending moment is constant, the normal strain at a distance x from the neutral axis (or neutral plane) can be calculated using the following equation [23]

$$\varepsilon_z = \frac{x}{\rho} = k\,x, \tag{2}$$

where ρ is the bending radius, and k is the reciprocal of the bending radius, called curvature. The intensity of the applied force to the beam, called stress, holds the points above the neutral axis in tension, resulting in a positive strain. Points below the neutral axis are under compressive stress, and the strain is negative. In other words, depending on the sign of the strain, the curvature direction can be determined in the bending plane. Therefore, once the normal strain is calculated from the measured wavelength shift in the FBG sensor using (1), the curvature of the beam and the upward or downward direction of bending can be extracted from (2).

Shape sensing using FBGs is based on multiple off-axis strain measurements at the cross-section during bending. At least two FBGs are required to determine the spatial curve of the sensor, assuming that z-information is already known by the position of the FBGs. A third FBG is further needed to compensate for the effect of temperature on the reflected signal. In the literature, placing three FBGs at each sensor plane was usually done by multicore fibers with FBG arrays [8] or embedded single-mode FBGs in a grooved cylindrical substrate [24]. It was assumed that the sensor probe behaves as a uniform, symmetric, linear Kirchhoff rod [8]. Therefore, considering the sensor probe as a beam under pure bending results in the following equations, which calculate the strain of three independent FBGs (also called FBG triplet) at each sensor plane,

$$\begin{aligned} \varepsilon_1 &= |k|\,d\,sin(\theta) + \varepsilon_T, \\ \varepsilon_2 &= |k|\,d\,sin(\theta + 120°) + \varepsilon_T, \\ \varepsilon_3 &= |k|\,d\,sin(\theta + 240°) + \varepsilon_T. \end{aligned} \tag{3}$$

In these equations, d is the radial distance between the FBGs and the neutral axis of the sensor, and ε_T is the thermal strain.

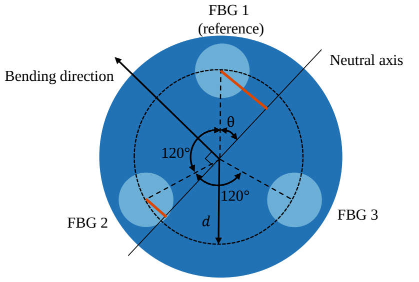

Fig. 3. Cross-section of a shape sensor based on multicore or embedded FBGs. The orange lines indicate the distance between the FBGs and the neutral plane.

As can be seen in Fig. 3, the sensor probe does not meet the homogeneity condition due to the presence of the optical fibers. However, this heterogeneous material density leads to minor inaccuracies when the sensor is not under tight bending [8].

According to (3), the Bragg wavelength in these sensors changes linearly with respect to curvature and temperature variations. The first arguments on the right-hand side are the normal strain caused by the bending moment in which the distance between the FBGs and the neutral plane (orange lines in Fig. 3) changes sinusoidally depending on the bending direction. Therefore, the sensor's angular behavior can be fitted with a sine function as long as the bending resistance remains the same in all possible directions.

However, attaching the optical fibers to a small cylindrical substrate result in a triangular cross-section with considerable non-uniformity in the material density. Beams with non-uniform bending resistance may twist during bending at specific directions, depending on the shape and density distribution at their cross-section. Therefore, the expression that describes the angular behavior of the sensor should include the effect of twisting at bending directions where material density changes significantly [25]. Consequently, the angular response of the sensor cannot be fitted with a sine wave anymore. Replacing the sine functions in (3) with a general angular function $G(\theta)$ and substituting it in (1) leads to the following equation system

$$\frac{\Delta\lambda_{Bj}}{\lambda_{Bj}} = F_j(|k|)\, G_j(\theta) + (\alpha_\Lambda + \alpha_n)\, \Delta T\ ;\ j\ =\ 1, 2, and\ 3. \qquad (4)$$

The function $G(\theta)$ should be obtained experimentally as there are many unknown factors related to the exact shape and density distribution in the cross-section of the fiber bundle after assembling the sensor. Therefore, a calibration setup should be designed such that enough data can be acquired to estimate $G(\theta)$. The linear response of the sensor to the curvature variations $F(|k|)$ is equal to $\eta\ (1\ -\ P_e)\ |k|\ d_j$ which includes a correction factor η for strain transfer between the substrate and the FBGs. Solving the equation system (4) at each sensor plane provides the curvature and the bending direction, which are later used to reconstruct the 3D shape of the sensor.

III. 3D SHAPE RECONSTRUCTION

In this paper, we investigated two commonly used methods to reconstruct spatial curves from discrete k and θ values, the Kinematic model [26] and Frenet-Serret formulas [24], [8], and compared the predicted shape and tip position of the sensor. For the kinematic model, we first linearly interpolated the measured k and θ to return values at arc elements with 1 mm length along the sensor. Then, each arc element's spatial coordinate was calculated in its local frame using the curvature and bending direction of that segment. Finally, the coordinates of the arc elements were transferred to a global frame to draw the spatial curve of the sensor. As shown in Fig. 4, the local coordinate system for each segment is defined, such that the arc element is tangent to the Z-axis, and its beginning point coincides with the origin of the frame. Having the bending plane of the arc element at the angle of θ from the X-axis, the homogeneous coordinate of the segment's tip P can be obtained

$$P = \begin{bmatrix} \Delta x \\ \Delta y \\ \Delta z \\ 1 \end{bmatrix} = \begin{bmatrix} \frac{1}{k}(1 - cos\varphi)\ cos\theta \\ \frac{1}{k}\ (1 - cos\varphi)\ sin\theta \\ \frac{1}{k}\ sin\varphi \\ 1 \end{bmatrix}, \qquad (5)$$

where φ is the central angle of the arc, calculated from the curvature multiplied by the arc length ds; $\varphi\ =\ k\ ds$.

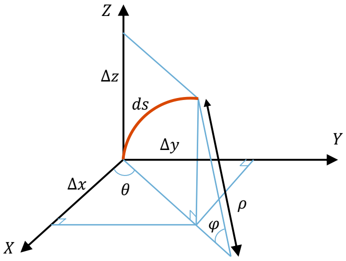

Fig. 4. The local coordinate system for each arc element.

The 3D shape of the sensor is reconstructed by transforming the coordinate of the arc elements from their local coordinate system to the global frame. The global frame Ψ_0 is defined at the base of the sensor, which coincides with the local coordinate system of the first arc element Ψ_1. Transforming Ψ_1 to the local frame of the second segment includes rotating the coordinate system using R_1 (more detail is available in the Appendix) followed by translation T_1 from O_1 to O_2, the origins of the coordinate systems

$$T_1\ = \begin{bmatrix} 1 & 0 & 0 & -\Delta x_1 \\ 0 & 1 & 0 & -\Delta y_1 \\ 0 & 0 & 1 & -\Delta z_1 \\ 0 & 0 & 0 & 1 \end{bmatrix}. \qquad (6)$$

The local coordinate system of the second segment Ψ_2 is as follows

$$\Psi_2 = T_1 R_1 \Psi_1. \tag{7}$$

The transformation matrix from Ψ_1 to the desired local coordinate system Ψ_t, where t shows the segment number, is a sequence of the transformation matrices from the previous segments

$$\Psi_t = T_{t-1} R_{t-1} T_{t-2} R_{t-2} \ldots T_1 R_1 \Psi_1, \tag{8}$$

which can be reformulated as

$$\Psi_t = R_{t-1} T_{t-1} \Psi_{t-1}. \tag{9}$$

The spatial coordinate of each arc element in the global frame can be calculated by multiplying its local coordinates by the inverse of the transformation matrix

$$\begin{bmatrix} X_{t+1} \\ Y_{t+1} \\ Z_{t+1} \\ 1 \end{bmatrix} = \Psi_t^{-1} \begin{bmatrix} \Delta x_t \\ \Delta y_t \\ \Delta z_t \\ 1 \end{bmatrix}. \tag{10}$$

The second approach to reconstruct the 3D shape of the sensor is based on Frenet-Serret formulas that define the geometric properties of a curve in the Euclidean space. These formulas describe the derivatives of three unit-vectors in terms of each other

$$\begin{aligned} \frac{dt}{ds} &= k\, n, \\ \frac{dn}{ds} &= -k\, t + \tau\, b, \\ \frac{db}{ds} &= -\tau\, n, \end{aligned} \tag{11}$$

The unit-vector t is tangent to the curve, the bending direction is shown by the unit-vector n, and b is the binormal unit-vector, perpendicular to the bending plane. The torsion, indicated by τ, is the derivative of the bending direction θ with respect to the arc length s. Once the unit-vectors at each segment are obtained using the equation system (11), knowing the curvature and the torsion, the position vector $r(s)$ can be calculated

$$\begin{aligned} dr &= T ds, \\ r(s) &= \int T ds. \end{aligned} \tag{12}$$

Consequently, the spatial coordinate of the segments in the global frame is obtained as a function of the arc length

$$\begin{bmatrix} X(s) \\ Y(s) \\ Z(s) \end{bmatrix} = r(s). \tag{13}$$

IV. SENSOR ASSEMBLY AND INTERROGATION SETUP

The performance of the FBG shape sensors using single-mode fibers highly depends on the characteristics of the substrate. In the current design, we replaced the wire-braided Polyimide substrate used in our previous work [14] with a superelastic Nitinol wire that offers higher flexibility and lower thermal sensitivity. The wire's diameter is 0.25 mm, similar to Acrylate coated optical fibers, making the outer diameter of the sensor 0.75 mm. The single-mode fibers with four FBGs separated by 5 cm were chosen to cover the entire length of a typical 20 cm long endoscope. The three fibers were attached to the substrate using a highly flexible UV-cured glue (LOCTITE AA 3926). Three laser-cut holders were designed to properly align the optical fibers in a 120° configuration on the substrate during the gluing process. Each holder, as shown in Fig. 5 (a), was made from three aluminum pieces that create a unique shape in the middle, fitting the triangular cross-section of the sensor (see Fig. 5 (b)). The main reason for using multipiece holders was to remove them easily from the fiber bundle once the glue was cured.

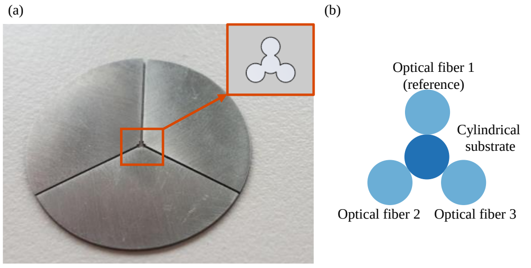

Fig. 5. (a) Three-piece laser cut holder used for aligning the optical fibers on the Nitinol wire. (b) Cross-section of the sensor.

The FBGs were interrogated using the wavelength division multiplexing (WDM) technique, as illustrated in Fig. 6. A superluminescent diode (SLED) with an integrated circulator was used to cover the Bragg wavelength of all 12 FBGs from 1515 nm to 1570 nm. The Bragg wavelengths were then monitored using a fast spectrometer (I-MON 512, Ibsen) that was connected to the sensor via a fiber coupler. The measured relative wavelength shifts in the FBG triplets were then used to calculate the spatial coordinate of the arc segment at each sensor plane and to reconstruct the 3D shape of the sensor.

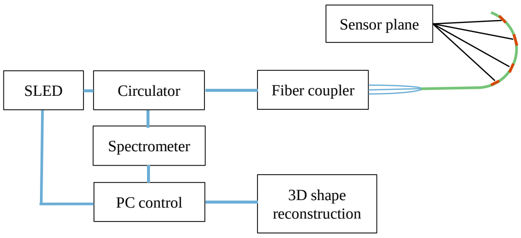

Fig. 6. Schematic of the interrogation setup.

V. CALIBRATION

The most common characterization technique for FBG-based shape sensors is to find the calibration curves by monitoring Bragg wavelength shifts in known 3D shapes, which is usually done by rotating the sensor in slots with different curvatures. However, the investigated design has an asymmetrical cross-section with preferred bending directions that causes instabilities during axial rotations. Consequently, repeatable measurements cannot be achieved using calibration setups that include rotational movements. Therefore, we designed 3D curvature templates to acquire ground truth data for bending radii of 17 cm, 20 cm, 23 cm, and 26 cm at all possible directions without the need for rotating the sensor. Each template consisted of a two-piece curved aluminum bar creating a 0.9 mm cylindrical groove in the middle to guide the sensor. The templates were fixed on a precision rotary stage, as shown in Fig. 7, to tune the bending direction accurately. For each curvature, the corresponding template was rotated from 0 to 360°, taking measurements every 20°. After each measurement, the sensor was carefully removed from the template and reinserted in the cylindrical groove at the desired angle using a slider. The Bragg wavelengths were recorded five minutes after sensor insertion for temperature settling, while the temperature was being monitored using a thermocouple attached to the template. Each measurement was repeated three times to reduce random angular deflection during sensor insertion into the template.

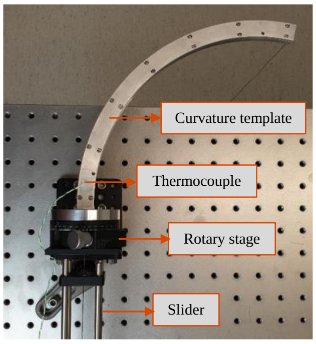

Fig. 7. Calibration setup, curvature template attached to a precision rotary stage.

Fig. 8 (a), (d), and (g) show the measured relative wavelength shifts of the FBGs in the first sensor plane at different bending angles and curvatures. Each data point is an average of three repeated measurements. The sensor warped slightly during bending at directions, where the material resistance varies significantly, resulting in sudden changes in the sensor's output. Therefore, as mentioned in Section II, the sine function describing the angular behavior of the sensor should be replaced with a more general function $G(\theta)$ that includes the twisting effect during bending. To obtain the function $G(\theta)$ for each FBG, we first fitted the acquired relative wavelength shifts at different bending angles using a smoothing spline. For the fitted curves to have a continuous transition from 360° to 0° angles and vice versa, we repeated ten data points in the fitting data for bending angles $\theta<0^\circ$ and $\theta>360^\circ$, which served as boundary conditions. Then, the normalized versions of the spline fitted curves were averaged to find the angular function $G(\theta)$ for the three FBGs in the first sensor plane, which are illustrated in Fig. 8 (b), (e), and (h). The function $F(|k|)$ that predicts the response of each FBG to different curvatures was obtained by linearly fitting the maximum relative wavelength shifts extracted from the spline fitted curves (see Fig. 8 (c), (f), and (i)). A similar method was used for all other FBG triplets.

For testing the generality of the proposed model, a 10-fold cross-validation test has been carried out. The data collected from each template were shuffled randomly, then for each fold of cross-validation, 10% of them were left out for evaluation. The remaining data were used to find the function G and linear fit parameters for co-located FBGs. The estimated values for k and θ were calculated by numerically solving the equation system (4). Table I shows the P-values of the one-way ANOVA test on the curvature and bending direction prediction error for all four FBG triplets. All P-values are higher than 0.05, the significance level, which indicates that differences between the means are not statistically significant. The box plot of the prediction error in curvature and bending direction for different folds at the first FBG triplet is illustrated in Fig. 9, which graphically shows that the median does not significantly change between the folds. Therefore, it can be concluded that the proposed model is general enough to describe asymmetric shape sensors that have bending preferences, and the fitting parameters do not change for different datasets.

TABLE I
P-VALUES OF ONE-WAY ANOVA TEST ON THE PREDICTION ERROR IN THE CURVATURE AND BENDING DIRECTION AT FOUR FBG TRIPLETS.

FBG triplet	1	2	3	4
P-value (Curvature)	0.9805	0.6700	0.3138	0.2459
P-value (Bending direction)	0.4525	0.3794	0.2375	0.2635

VI. SENSOR EVALUATION

The shape prediction model for the fiber sensor can be selected from any fitting parameters calculated in each fold of the ANOVA test. We tested the sensor's performance, based on fold number 10, in two different situations, single-bend and multi-bend. In single-bend, also known as C-bend, all FBG triplets experienced the same curvature and bending direction, whereas, in multi-bend, various curve deformations existed throughout the sensor.

For the single-bend test, 27 measurements at different curvatures and bending angles were acquired using the 3D templates. Fig. 10 (a) illustrates the 3D view of reconstructed shapes using the kinematic model and Frenet-Serret equations, as well as the real shape of the sensor, which is known from the curvature template. The top, side, and front views of all three curves can be seen in Fig. 10 (b). The residuals, calculated from the Euclidean distance between the predicted and the real

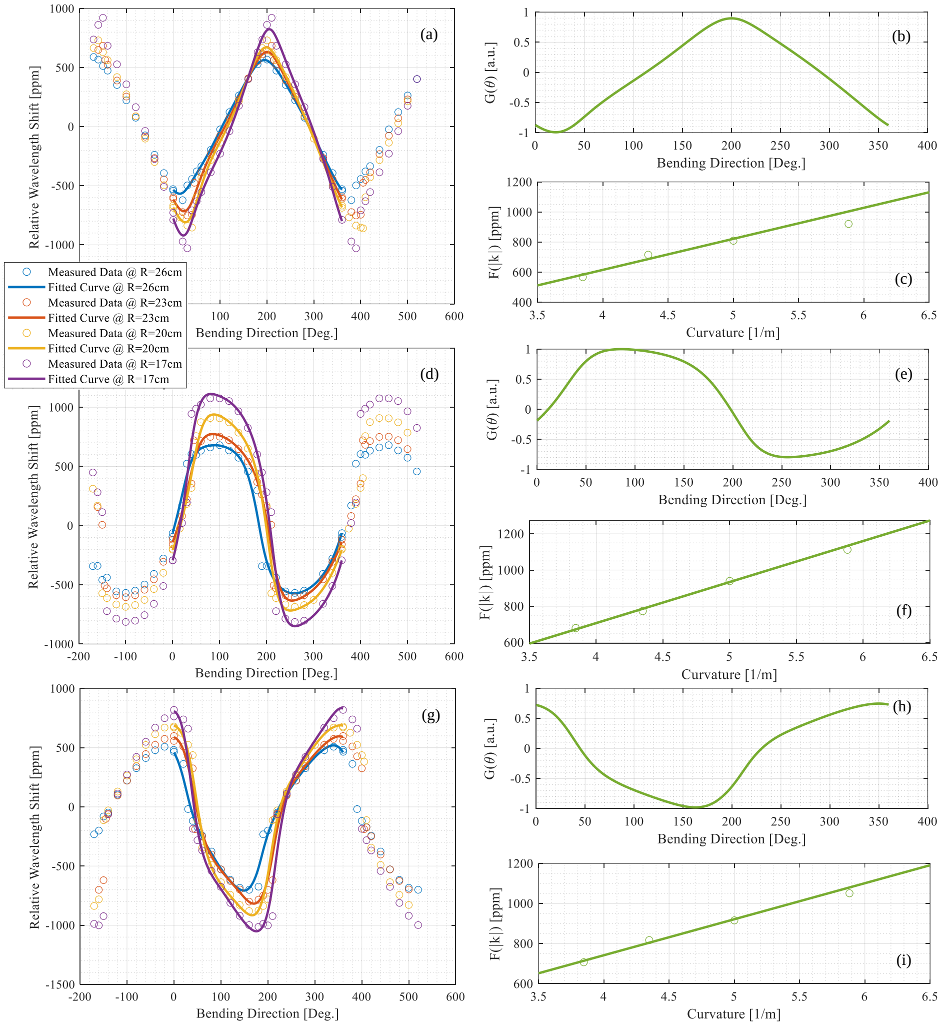

Fig. 8. Measured relative wavelength shifts and the fitted curves for the first FBG triplet using four curvature templates (a, d, and g). The angular functions are displayed in graphs b, e, and h. The linear functions (also known as curvature sensitivity) for FBG numbers 1, 2, and 3 are shown in figures c, f, and i, respectively.

coordinate values at FBG triplet locations, are shown in Fig. 10 (c). It can be noticed that the residuals are accumulatively increasing when getting closer to the sensor's tip, which is due to the error in the predicted bending direction. We observed the ascending error in most testing data. In all testing examples, the reconstructed shape using the Frenet-Serret formula had a larger error than the kinematic model. We believe this larger error can be attributed to the adaptive arc elements' length in solving the differential Frenet-Serret equations. The arc lengths in this method depend on how the torsion and curvature values are changing along the spatial curve. The torsion and the curvature values for each arc element are calculated by interpolating predicted k and θ at FBG triplets. Therefore, if the predicted values have an error, interpolating for small elements raises the inaccuracy of the predicted shape even further.

Evaluating the sensor in a multi-bend case, when the sensor experienced larger deflections in arbitrary shapes, was performed using a motion capture system (MOCAP) (Qualisys AB, Sweden). The MOCAP system consists of five cameras to capture motions from different views, as shown in Fig. 11 (a). Five passive markers were attached to the sensor to monitor the real shape during data acquisition. The markers are 9.5 mm in diameter and have a 1 mm hole in the middle allowing the fiber sensor to pass through (Fig. 11 (b)).

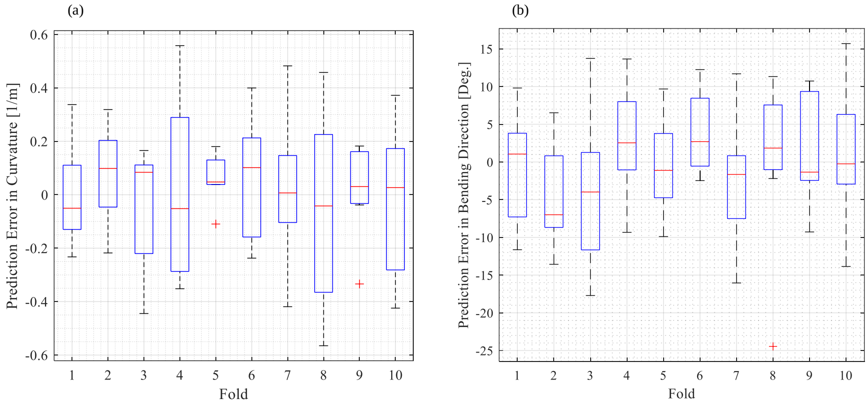

Fig. 9. Box plot of prediction error in (a) curvature and (b) bending direction for 10 folds, at the first sensor plane. On each box, the median is indicated with a central mark, and the 25th and 75th percentiles are indicated with the bottom and top edges of the box, respectively. The whiskers show the minimum and maximum values within each group not considered outliers, and the outliers are marked with the '+' symbol.

The local coordinate system of the sensor was realized by fixing the sensor's base on a reference plate. The reference plate was a rectangular Aluminum part with two circular grooves and one cylindrical groove for placing markers and the sensor in predefined locations. The X and Y-axis of the reference plate were measured by placing two markers in the circular grooves and two markers in the cylindrical one, as shown in Fig. 12 (a). The location and orientation of the sensor's base were fixed during data acquisition (Fig. 12 (b)). The marker locations in the coordinate system, defined by the MOCAP managing software, were moved into the sensor's local frame using a transformation matrix. Finally, the spatial curve of the sensor's real shape with 1 mm resolution was estimated by interpolating the marker locations using the cubic Spline method [27].

Collecting the testing data in the multi-bend case was

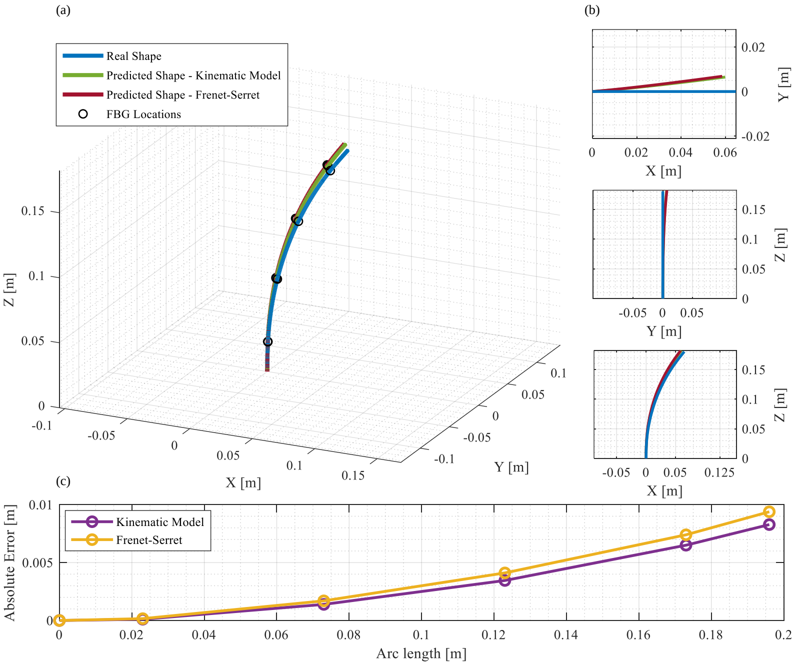

Fig. 10. (a) 3D view, and (b) 2D views of the real and the predicted shapes in a single-bend deformation. (c) The absolute error between the predicted and the real coordinates at FBG triplets, where the circles show the base, the sensing spots, and the tip of the sensor.

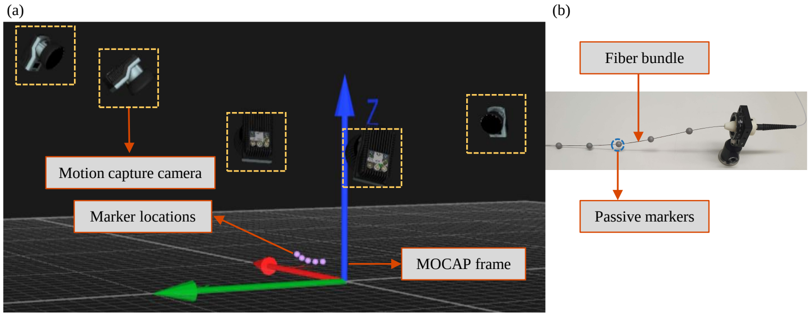

Fig. 11. (a) Oqus camera setup in MOCAP software. (b) Marker attachment to the sensor.

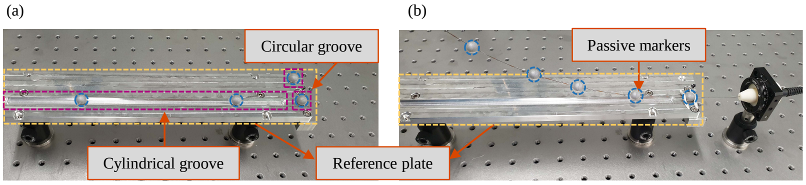

Fig. 12. (a) The local frame realization of the reference plate. (b) Fixation of the sensor in the reference plate.

performed by moving the sensor's tip at different locations, allowing the sensor to be bent in various curvatures and bending directions from 0° to 180°. The experiment was repeated after rotating the sensor's base for 180° to cover the bending direction from 180° to 360°. To ensure that the tip of the sensor is free to rotate during shape manipulation, it was inserted into a Nitinol tube which was fixed in a moving holder.

An example of the reconstructed shape in the multi-bend experiment is shown in Fig. 13. Similar to the single-bend test, the kinematic model performs better than the Frenet-Serret method. However, as the number of sensing planes was limited, the shape sensor was not able to detect the deformations happening between the sensor planes. In Fig. 13 (b), a zoomed view of the beginning part of the sensor in the X-Y plane is shown. It can be noticed that the sensor did not see the deflection between its base and the first FBG triplet, and therefore, the false prediction in the bending direction resulted in a large error at the sensor's tip. Although this error can also happen in single-bend curves, the shape estimation is still more accurate because the curvature and bending direction are constant in C-bends.

In order to compare the goodness of predicted shapes in single and multi-bend cases, the root mean square (RMS) of the Euclidean distance between the predicted and real coordinates was calculated. The box plot in Fig. 14 (a) shows the RMSE for single and multi-bend curves using both kinematic and Frenet-Serret methods. Median values of the RMSE in reconstructed shapes using the kinematic model were 5 mm and 8.5 mm for single and multi-bend, respectively. These values increased up to 5.7 mm and 10.5 mm when Frenet-Serret equations were used for shape reconstruction. The median value for the tip positioning error in single and multi-bend deformations are 9.9 mm and 16.2 mm using the kinematic model, and 12.7 mm and 21.3 mm in the Frenet-Serret method. The higher median values in multi-bend curves, using both kinematic and Frenet-Serret formulas, can be explained by investigating the expected accuracy in marker-based curve estimations. The uncertainty in the estimated marker coordinates and the unknown distance between the centroid of the marker and the sensor's neutral axis are two possible error sources in this method. However, as mentioned earlier, the most important reason is the random twisting effect due to uneven force application during bending or the asymmetric cross-section of the sensor. The latter effect is stronger when the sensor is bent at smaller banding radii.

Another vital parameter to investigate is the bonding strength between the fibers and the substrate, which can be affected by adhesive aging. To study the effect of glue aging on the prediction accuracy, the single-bend measurements were repeated after ten months. As can be seen in Fig. 14 (b), the median values of the RMSE were 5 mm and 5.2 mm in kinematic, and 5.7 mm and 5.9 mm in Frenet-Serret-based shape reconstructions before and after this period. No significant change in the median value was observed, meaning that the aging of the glue is negligible, and the designed sensor remained stable over this time under the lab condition.

To see how the error changes with respect to the applied curvatures, the scatter plot of the estimated curvatures in the multi-bend experiment is shown in Fig. 15. The correlation coefficient for the predicted and the ground truth curvatures is 0.73, suggesting that the proposed calibration method is indeed suitable for the designed sensor. It can also be noticed that the error increases at higher curvatures, which might be due to the random twisting effect.

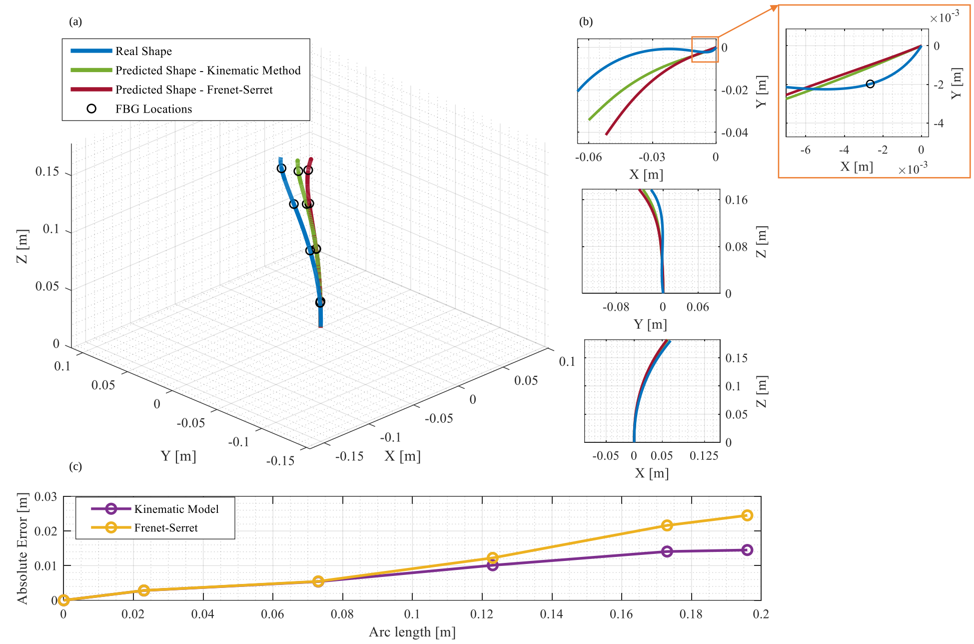

Fig. 13. (a) 3D view, and (b) 2D views of the real and the predicted shapes in a multi-bend deformation. (c) The absolute error between the predicted and the real coordinates at FBG triplets, where the circles show the base, the sensing spots, and the tip of the sensor.

VII. CONCLUSION

A suitable alternative to EM trackers or multicore fibers in medical tool navigation can be shape sensors composed of three single-mode fibers. In such sensors, the substrate plays a crucial role. If a semi-rigid substrate is used, like Nitinol needles or wire-braided polyimide tubes, an uncertainty of around 1 % at the sensor's tip (average error divided by the sensor length) can be reached [6], [14]. However, these sensors are only suitable for applications where small deflections are expected. For a sensor with the same level of flexibility as an optical fiber, a substrate with similar mechanical resistance must be used. Although such a sensor can reach higher curvature levels, bending stiffness at its cross-section is no longer uniform and can show bending preference and random twisting effect during

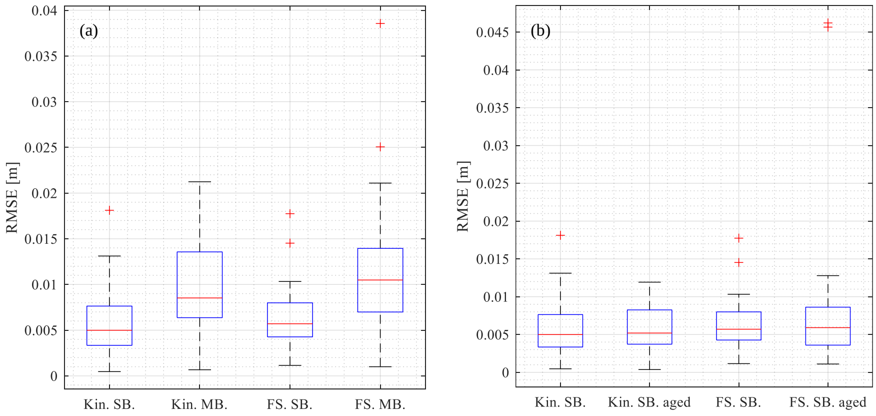

Fig. 14. (a) RMSE of the Euclidean distance between the predicted and real coordinates in single-bend (SB.) and multi-bend (MB.) shapes, reconstructed using kinematic model (Kin.) and Frenet-Serret formula (FS.). (b) The effect of glue aging on the prediction accuracy in single-bend measurements.

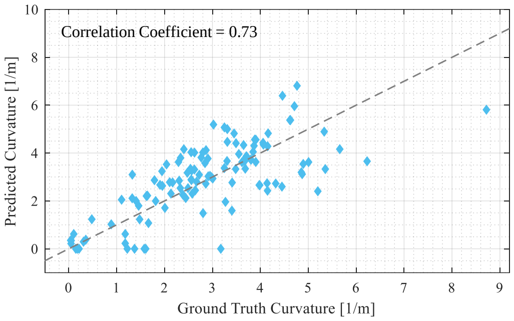

Fig. 15. Scatter plot for the predicted and the ground truth curvatures. The dashed line shows the baseline at 45°.

bending. We observed that in such sensor configurations, the prediction accuracy of the bending direction is limited by the random twisting effect, which increases the uncertainty at the sensor's tip up to 5 % in medium and 10 % in large deflections. Therefore, there is always a tradeoff between the accuracy of the sensor's shape prediction and flexibility. We studied two shape reconstruction methods, the kinematic model and the Frenet-Serret formula. We believe that the kinematic model is more suitable for such sensor design, as it shows higher shape prediction accuracy compared to the Frenet-Serret approach. We also demonstrated that our sensor shows no significant glue aging after ten months under lab conditions.

For further development of this highly flexible shape sensor, we will use draw tower gratings with polymer coating as they offer higher mechanical strength compared to the currently used stripped FBGs. To compensate for the asymmetric cross-section of the sensor, dummy fibers will be placed around the sensor probe, which may reduce the flexibility of the sensor yet increase the accuracy by limiting bending preferences.

REFERENCE

[1] "Flagship Project MIRACLE | Department of Biomedical Engineering." https://dbe.unibas.ch/en/research/flagship-project-miracle/ (accessed Nov. 12, 2021).

[2] M. Eugster *et al.*, "Miniature parallel robot with submillimeter positioning accuracy for minimally invasive laser osteotomy," *Robotica*, pp. 1–28, 2021, doi: 10.1017/S0263574721000990.

[3] C. Shi *et al.*, "Shape sensing techniques for continuum robots in minimally invasive surgery: a survey," *IEEE Trans. Biomed. Eng.*, vol. 64, no. 8, pp. 1665–1678, Aug. 2016, doi: 10.1109/TBME.2016.2622361.

[4] A. Dore *et al.*, "Catheter navigation based on probabilistic fusion of electromagnetic tracking and physically-based simulation," in *IEEE Int. Conf. Intell. Robots Syst.*, Oct. 2012, pp. 3806–3811. doi: 10.1109/IROS.2012.6386139.

[5] M. Bock *et al.*, "Active catheter tracking using parallel MRI and real-time image reconstruction," *Magn. Reson. Med.*, vol. 55, pp. 1454–1459, May 2006, doi: 10.1002/mrm.20902.

[6] R. J. Roesthuis *et al.*, "On using an array of fiber Bragg grating sensors for closed-loop control of flexible minimally invasive surgical instruments," in *IEEE Int. Conf. Intell. Robots Syst.*, Nov. 2013, pp. 2545–2551. doi: 10.1109/IROS.2013.6696715.

[7] S. C. Ryu and P. E. Dupont, "FBG-based shape sensing tubes for continuum robots," in *IEEE Int. Conf. Robot. Autom. (ICRA)*, May 2014, pp. 3531–3537. doi: 10.1109/ICRA.2014.6907368.

[8] J. P. Moore and M. D. Rogge, "Shape sensing using multi-core fiber optic cable and parametric curve solutions," *Opt. Express*, vol. 20, no. 3, pp. 2967–2973, Jan. 2012, doi: 10.1364/OE.20.002967.

[9] C. Waltermann *et al.*, "Femtosecond laser processing of evanescence field coupled waveguides in single mode glass fibers for optical 3D shape sensing and navigation," in *Proc. of SPIE*, May 2015, vol. 9480, pp. 948011–948015. doi: 10.1117/12.2183334.

[10] B. J. Soller *et al.*, "High resolution optical frequency domain reflectometry for characterization of components and assemblies," *Opt. Express*, vol. 13, no. 2, pp. 666–674, 2005, doi: 10.1364/OPEX.13.000666.

[11] R. R. Thomson *et al.*, "Ultrafast-laser inscription of a three dimensional fan-out device for multicore fiber coupling applications," *Opt. Express*, vol. 15, no. 18, pp. 11691–11697, 2007, doi: 10.1364/OE.15.011691.

[12] M. Cohen *et al.*, *Planar Waveguides and other Confined Geometries*, vol. 189. New York: Springer New York, 2015. doi: 10.1007/978-1-4939-1179-0.

[13] H. Moon *et al.*, "FBG-based polymer-molded shape sensor integrated with minimally invasive surgical robots," in *IEEE Int. Conf. Robot. Autom. (ICRA)*, May 2015, pp. 1770–1775. doi: 10.1109/ICRA.2015.7139427.

[14] S. Manavi *et al.*, "Temperature-compensated FBG-based 3D shape sensor using single-mode fibers," in *Adv. Photonics*, 2018, p. JTu6C.1. doi: BGPPM.2018.JTu6C.1.

[15] J. Yi *et al.*, "Spatial shape reconstruction using orthogonal fiber Bragg grating sensor array," *Mechatronics*, vol. 22, pp. 679–687, Jan. 2012, doi: 10.1016/j.mechatronics.2011.10.005.

[16] Y.-L. Park *et al.*, "Real-time estimation of 3-D needle shape and deflection for MRI-guided interventions," *IEEE/ASME Trans. Mechatronics*, vol. 15, no. 6, pp. 906–915, Dec. 2010, doi: 10.1109/TMECH.2010.2080360.

[17] K. R. Henken *et al.*, "Error analysis of FBG-based shape sensors for medical needle tracking," *IEEE/ASME Trans. Mechatronics*, vol. 19, no. 5, pp. 1523–1531, Oct. 2013, doi: 10.1109/TMECH.2013.2287764.

[18] H. Moon *et al.*, "Fiber-Bragg-grating-based ultrathin shape sensors displaying single-channel sweeping for minimally invasive surgery," *Opt. Lasers Eng.*, vol. 59, pp. 50–55, Aug. 2014, doi: 10.1016/j.optlaseng.2014.03.005.

[19] A. Othonos *et al.*, "Fibre Bragg gratings," in *Wavelength Filters in Fibre Optics*, vol. 123, Germany: Springer Berlin Heidelberg, 2006, p. 197. doi: 10.1007/3-540-31770-8_6.

[20] X. Chen *et al.*, "Updated shape sensing algorithm for space curves with FBG sensors," *Opt. Lasers Eng.*, vol. 129, no. April, p. 106057, 2020, doi: 10.1016/j.optlaseng.2020.106057.

[21] B. Kim *et al.*, "Optimizing curvature sensor placement for fast, accurate shape sensing of continuum robots," *Proc. - IEEE Int. Conf. Robot. Autom.*, pp. 5374–5379, 2014, doi: 10.1109/ICRA.2014.6907649.

[22] S. Yin *et al.*, *Fiber Optic Sensors*, 2nd ed. Boca Raton: CRC Press, 2008.

[23] J. M. Gere and S. P. Timoshenko, *Mechanics of Materials*, vol. 53, no. 9. Boston, MA: Springer US, 1991. doi: 10.1007/978-1-4899-3124-5.

[24] K. Henken *et al.*, "Accuracy of needle position measurements using fiber Bragg gratings," *Minim. Invasive Ther. Allied Technol.*, vol. 21, pp. 408–414, Nov. 2012, doi: 10.3109/13645706.2012.666251.

[25] F. B. Seely *et al.*, "The torsional effect of transverse bending loads on channel beams," Urbana, Jul. 1930.

[26] R. J. Roesthuis *et al.*, "Modeling and steering of a novel actuated-tip needle through a soft-tissue simulant using Fiber Bragg Grating sensors," in *IEEE Int. Conf. Robot. Autom. (ICRA)*, May 2015, pp. 2283–2289. doi: 10.1109/ICRA.2015.7139502.

[27] C. de Boor, *A Practical Guide to Splines - Revised Edition*, 1st ed. Springer New York, 1978.

[28] M. Duncan, *Applied Geometry for Computer Graphics and CAD*. London: Springer London, 2005. doi: 10.1007/b138823.

VIII. APPENDIX

Transforming the local frame of the arc element i (Ψ_i) to the local frame of the next segment (Ψ_{i+1}) includes rotating the coordinate system about an arbitrary axis called B through the angle φ_i followed by translation T_i from O_i to O_{i+1}, the origins of the coordinate systems

$$T_i \ = \begin{bmatrix} 1 & 0 & 0 & -\Delta x_i \\ 0 & 1 & 0 & -\Delta y_i \\ 0 & 0 & 1 & -\Delta z_i \\ 0 & 0 & 0 & 1 \end{bmatrix}. \tag{14}$$

As illustrated in Fig. 16, axis B is perpendicular to the bending plane π_i, passing through the origin of the frame. A series of rotations are required to obtain the desired orientation of the local frame for the next segment [28]. First, the coordinate system Ψ_i (X, Y, Z) is rotated through the angle θ_i about the Z-axis, such that axis B lies in the Y-axis, aligning the X-Z plane with the bending plane π_i. The new frame (X', Y', Z) is then rotated about the Y$'$-axis through the angle φ_i, making the Z'-axis tangent to the tip of the next segment in the (X'', Y', Z') frame. Finally, step one should be reversed by rotating the (X'', Y', Z') coordinate system about the Z'-axis through the angle $-\theta_i$ to obtain the local frame (X''', Y'', Z') for the next segment. The total rotation matrix that includes the sequence of rotations is the following

$$R_i \ = \ R_{(Z\prime,-\theta_i)}\, R_{(Y\prime,\varphi_i)}\, R_{(Z,\theta_i)} \tag{15}$$

where,

$$R_{(Z,\theta_i)} = \begin{bmatrix} cos\theta_i & sin\theta_i & 0 & 0 \\ -sin\theta_i & cos\theta_i & 0 & 0 \\ 0 & 0 & 1 & 0 \\ 0 & 0 & 0 & 1 \end{bmatrix}, \tag{16}$$

$$R_{(Y\prime,\varphi_i)} = \begin{bmatrix} cos\varphi_i & 0 & -sin\varphi_i & 0 \\ 0 & 1 & 0 & 0 \\ sin\varphi_i & 0 & cos\varphi_i & 0 \\ 0 & 0 & 0 & 1 \end{bmatrix}, \tag{17}$$

`

$$R_{(Z\prime,-\theta_i)} = \begin{bmatrix} cos\theta_i & -sin\theta_i & 0 & 0 \\ sin\theta_i & cos\theta_i & 0 & 0 \\ 0 & 0 & 1 & 0 \\ 0 & 0 & 0 & 1 \end{bmatrix}. \tag{1}$$

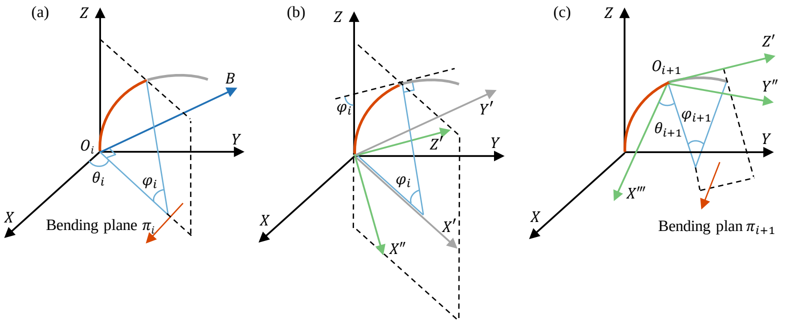

Fig. 16. The transformation steps from the global frame (X, Y, Z) to the second local coordinate system (X''', Y'', Z'). (a) rotation through the angle θ_i about Z-axis, (b) rotation about Y'-axis through the angle φ_i, (c) rotation about Z'-axis through the angle $-\theta_i$ to align the X'''-Y'' plane with the bending plane π_{i+1} followed by translation from O_i to O_{i+1}.

Chapter 5

Feasibility Study on Using Deep Learning to Model Edge-FBG Sensors

The next three chapters address the development process of a second sensing mechanism based on edge-FBGs. This chapter presents a feasibility study on using deep learning for modeling edge-FBG shape sensors. We designed a convolutional neural network optimized using hyperparameter tuning techniques that can learn to predict the sensor's shape directly from the edge-FBG spectra. The developed model can predict the shape of a $30\,\mathrm{cm}$ long sensor with a median tip error of less than $6\,\mathrm{mm}$ in a curvature range of $1.4\,\mathrm{m}^{-1}$ to $35.3\,\mathrm{m}^{-1}$ and does not require any calibration or shape reconstruction steps. The key advantage of this modeling technique compared to other intensity-based fiber shape sensing solutions is utilizing a low-cost interrogation system for measuring the edge-FBGs spectra.

Publication. The proposed shape sensing solution was presented in the form of an oral presentation at the SPIE OPTICS + OPTOELECTRONICS conference, April 2021, Online Only, in the Czech Republic. The following manuscript was published as part of the conference proceedings [44].

This is the accepted manuscript version of the following article:
S. Manavi, T. Renna, A. Horvath, S. Freund, A. Zam, G. Rauter, W. Schade, and P. C. Cattin. Using supervised deep-learning to model edge-FBG shape sensors: a feasibility study. In Optical Sensors 2021, volume 11772, page 117720P. International Society for Optics and Photonics, SPIE, 2021.
The final authenticated version is available online at https://doi.org/10.1117/12.2589252.

Using Supervised Deep-Learning to Model Edge-FBG Shape Sensors: a Feasibility Study

Samaneh Manavi[1,*], Tatiana Renna[1], Antal Horvath[1], Sara Freund[1], Azhar Zam[2], Georg Rauter[3], Wolfgang Schade[4], Philippe C. Cattin[1]

[1]Center for medical Image Analysis & Navigation (CIAN), Department of Biomedical Engineering, University of Basel, Gewerbestrasse 14, 4123 Allschwil, Switzerland;
[2]Biomedical Laser and Optics Group (BLOG), Department of Biomedical Engineering, University of Basel, Gewerbestrasse 14, 4123 Allschwil, Switzerland;
[3]Bio-Inspired RObots for MEDicine-Laboratory (BIROMED-Lab), Department of Biomedical Engineering, University of Basel, Gewerbestrasse 14, 4123 Allschwil, Switzerland;
[4]Department of Fiber Optical Sensor Systems, Fraunhofer Institute for Telecommunications, Heinrich Hertz Institute, HHI, Am Stollen 19H, 38640 Goslar, Germany

[*]Corresponding author: samaneh.manavi@unibas.ch, +41 (0) 61 207 5481, https://dbe.unibas.ch/planning-navigation

ABSTRACT

Continuum robots are snake-like elastic structures that can be bent anywhere along their length hence representing ideal tools for minimally invasive surgery. To accurately control these flexible manipulators, 3D shape sensors that are small, sterile, immune to electromagnetic noise, and easy to replace are required. Fiber Bragg Grating (FBG)-based shape sensing is a promising approach for this task. The recently proposed Edge-FBG based shape sensors are particularly promising due to their high flexibility and high spatial resolution. In Edge-FBGs, the amplitude change at the Bragg wavelengths contains the strain information at sensing nodes. However, such sensors are sensitive to changes in the spectrum profile caused by undesired bending-related phenomena. As the existing theories cannot accurately predict the spectrum profile in curved optical fibers, changes in the initial intensity that each Edge-FBG receives are not precisely known. These uncontrolled variations cause inaccuracies in shape predictions and make standard characterization techniques less suitable for Edge-FBG sensors. Therefore, developing a model that distinguishes the strain signal from the changes in the spectrum profile is needed. Machine learning techniques are great tools for studying complex problems, making it possible to explore the full spectrum of the Edge-FBG sensor for identifying patterns caused by bending.

In this paper, we studied the feasibility of using a low-cost interrogation system for the Edge-FBGs, considering the minimum required signal-to-noise ratio. We trained a neural network with supervised deep learning to directly extract the shape information from the Edge-FBG spectrum. The designed model can predict the shape of a fiber sensor consisting of five Edge-FBG triplets with less than 6 mm tip error.

Keywords: Supervised deep learning, shape sensing, bending birefringence, bending loss, Edge-FBG, fiber sensor

1. INTRODUCTION

In recent years, the need for flexible robots and endoscopes has grown significantly, as they represent ideal tools for getting access to deep locations inside the patient's body during minimally invasive surgeries. However, accurately controlling these flexible manipulators' exact shape and tip position is a challenge that may result in irreversible damages to non-targeted tissues. Therefore, a shape sensor is needed to provide real-time feedback for the surgeon to control the endoscope during the surgical procedure safely. The integrated sensor needs to be small, biocompatible, easily replaceable, and immune to interferences with the robot's electromagnetic field. Commonly used tracking technologies, such as electromagnetic sensors or intraoperative imaging technologies, are not ideal for controlling elastic structures during minimally invasive surgeries, as they all have shortcomings like electromagnetic sensitivity (electromagnetic sensors), limited resolution (ultrasound imaging), low speed (MRI), or high doses of radiation (X-ray or CT imaging) [1]. FBG-based shape sensing, on the other hand, is considered the most promising approach regarding biosafety, high speed, and electromagnetic immunity [2].

Although different configurations for FBG sensors based on multicore fibers, cladding waveguides, and single-mode fiber bundles have been studied in recent years, accurate shape estimation is still challenging. Multicore FBG sensors are costly [3], as an optical frequency domain reflectometer (OFDR) is needed for interrogating the FBGs [4], plus a fan-out device for reading the signal from each core [5]. Cladding waveguide FBG sensors (CWG-FBG) work based on wavelength division multiplexing (WDM). Therefore, the number of sensing points is limited by the spectral bandwidth of the light source and the spectrometer. In addition, the power of the forward propagating light decreases every time that it couples into cladding waveguides, limiting the number of sensors even further. Although shape sensors which consist of multiple single-mode fibers [1], [2], [6, p. 242], [7], [8], also work based on WDM, they have limited flexibility and can only detect low to medium deflections.

Edge-FBGs are a new generation of highly flexible fiber-based shape sensors, in which the FBGs are inscribed on the edge of the fiber's core [9] (shown in Figure 1). Like other FBG-based shape sensors, the wavelength of the Edge-FBGs shifts slightly when bending-induced mechanical strain is applied to the Edge sensor. As these wavelength shifts are usually below 15 pm [9], an expensive interrogation system with high resolution would be needed. However, the amplitude of the Edge-FBGs also carries the strain information, which can be interrogated with simpler setups. As explained in [9], the mode field's center moves toward the bending direction in a curved single-mode fiber. Therefore, the intensity ratio between the Edge-FBGs at each sensor plane changes according to the radial and angular distance between the dislocated mode field and the Edge-FBGs. However, bending-related phenomena that affect the spectrum profile of the light propagating in the single-mode fiber are not considered in this approach. Macro bending in optical fibers may cause oscillatory attenuation loss, as the core-propagating field can couple coherently with reinjected fields reflected by cladding/coating or by coating/air interfaces [10]. Moreover, bending an optical fiber disturbs the symmetricity of the refractive index in the cross-section of the optical fiber and induces birefringence. Consequently, the polarization-sensitive elements inside the interrogation system filter the spectrum profile and cause errors in amplitude measurements. In this paper, we propose to model the Edge sensors using deep learning to predict the sensor's shape based on the full spectrum and not only the amplitude of the FBG peaks. This way, the effect of bending-related phenomena that influence the spectrum profile are also taken into account.

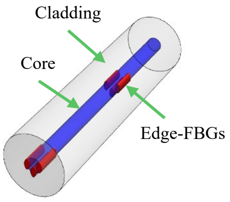

Figure 1. The structure of Edge-FBG sensors. At each sensing node, three FBGs are inscribed on the edge of the fiber's core.

2. METHODOLOGY

2.1 Data acquisition setup

The data acquisition setup used for collecting a set of data to develop our model is shown in Figure 2. The collected data contains the Edge-FBG spectrum and the sensor's actual shape, measured at different curvatures and orientations. We used the MIOPAS FBG interrogator (MIOPAS GmbH, Goslar, Germany), which consists of an uncooled TOSA module SLED and a NIR micro-spectrometer with 0.5 nm resolution and a maximum update rate of 75 Hz, to measure the Edge-FBG spectrum during data collection. Simultaneously, a motion capture system (MOCAP) (Qualisys AB, Sweden) was used to monitor the actual shape of the Edge sensor. The shape sensor is an array of five Edge-FBG triplets from 815 nm to 885 nm, inscribed every 5 cm in an SM800P fiber. As the fiber's outer diameter is only 155 µm, it was impossible to attach optical markers to the sensor directly. Therefore, the fiber was inserted into a Nitinol tube with an inner diameter of 320 µm and an outer diameter of 570 µm. For tracking the Nitinol tube, ten passive markers with an outer diameter of 9.5 mm were used. Each marker has a 1 mm hole in the middle allowing the Nitinol tube to pass through.

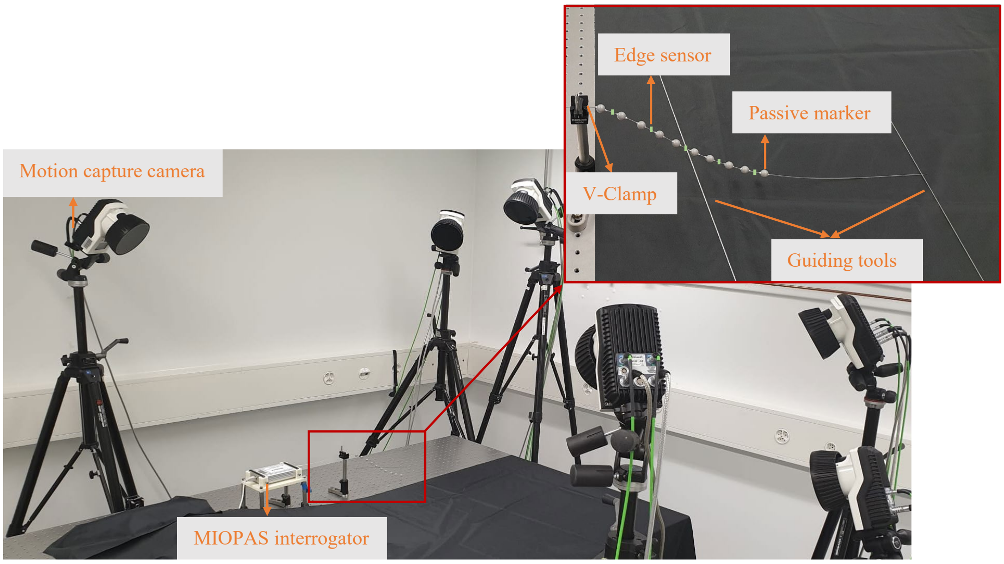

Figure 2. Experimental setup for data acquisition in medium deflections using a Nitinol tube.

The sensor's inlet was fixed using a v-clamp such that only the sensing area was allowed to move. We attached two guiding tools to the Nitinol tube to make the shape manipulation easier. We randomly moved the guiding tools for 30 min to change the sensor's shape in various curvatures and orientations. Later, the measured spectrum from the interrogator, and the marker coordinates from the MOCAP system, were synchronized based on their timestamps with a tolerance of 2.8 msec. The total acquired data size was 143160 samples, each sample containing the Edge-FBG spectrum (125 pixels) and the coordinates of 10 markers.

Although this setup was suitable for testing medium deflections, it was impossible to reach more complex shapes due to the limited flexibility of the Nitinol tube. Therefore, the Nitinol tube was replaced with a Hytrel furcation tubing to collect a separate set of data for larger deflections (Figure 3). The Hytrel tube has an inner diameter of 400 µm and an outer diameter of 900 µm. We used smaller passive markers with an outer diameter of 6.4 mm such that their weight is light enough for bending the tube in positive curvatures. The sensor's length, defined by the distance between the first and the tenth marker, is 22.5 cm in the medium deflection setup, which got extended up to 35 cm in the large deflection setup, as more markers were placed before the first Edge sensor.

2.2 Data preparation

Measurements with spectrometers often show random fluctuations that occur over time caused by various noise sources. Averaging over repeated measurements helps to increase the signal-to-noise ratio. In our case, the detected spectrum was not averaged during the measurement. Instead of averaging the scans in the data preprocessing step, we feed the network all scans acquired within a specified time interval and let the network combine them. We evaluated the network's performance when 2, 3, 5, and 10 measurements are fed into the network for averaging. The best model was achieved by providing three scans as the input data (125 × 3) and averaged marker locations as their output. To further increase the stability and performance of the neural network, the input data were normalized using the Z-score method.

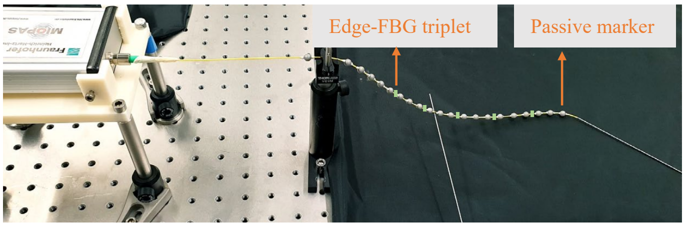

Figure 3. The data acquisition setup for large deflections using Hytrel tubing.

2.3 Hyperparameter tuning

Manually designing a network architecture is a time-consuming and computationally expensive process. Since for each choice of hyperparameter (e.g., parameters of the network architecture and parameters of the training process' optimizer), the network needs to be trained for a reasonable time. The Keras tuner, as an open-source framework for hyperparameter search [11], can automatically propose a suitable network architecture for the task at hand. Several hyperparameter optimization algorithms, such as Random search, Bayesian optimization, and Hyperband, are implemented in the Keras tuner. We chose the Hyperband algorithm, as it showed promising results in preliminary experiments concerning accuracy and execution time. In the hyperparameter search, the Huber loss [12] with a delta of 5 was calculated, projecting the absolute errors of the individual coordinates of all ten markers to a scalar. Table 1 lists the hyperparameters in the search space. The search was started by considering only dense layers, and then convolutional layers were added for possible further improvements. Faster convergence and better validation loss were achieved by applying batch normalization after the activation function of the convolutional layer. The mini-batch size was set to 128, and the size of the validation set was chosen to be 10 % of the total number of samples.

Table 1. The list of hyperparameters in the search space and their searching range. *Stochastic Gradient Descend

Hyperparameter	Search range
Number of 1D convolutional layers	Integer values from 1 to 30
Number of filters for convolutional layers	Integer values from 8 to 256 with a step size of 8
Kernel size	Integer values from 1 to 25
Number of dense layers	Integer values from 0 to 3
Number of units in a dense layer	Integer values from 8 to 128 with a step size of 8
Dropout rate	Values from 0 to 0.5 with a step size of 0.05
Activation function for convolutional layers	ReLU and Tanh
Activation function for dense layers	ReLU, Tanh, or Sigmoid
Learning rate for Adam optimization algorithm	0.01, 0.001, and 0.0001
Learning rate in SGD*	0.01, 0.001, 0.0001, and 0.00001
Momentum of SGD	0, 0.2, 0.4, 0.6, 0.8, and 0.9

2.4 Network architecture

The optimal network architecture was chosen by comparing the average of the validation loss as well as the average values of the tip error and the RMSE on the testing samples for all models proposed by the Keras tuner. The tip error is calculated by the Euclidean distance between the predicted and the actual location of the last marker and RMSE, as a measure of mismatch between the curves, is the root mean square of the Euclidean distance between the real and the predicted coordinates of all markers. Figure 4 shows one of the highest scored models: A feedforward neural network with one input layer, seven 1D Convolutional layers, each followed by the ReLU activation function and Batch normalization, a Flatten Layer, a Dropout Layer, and the output layer.

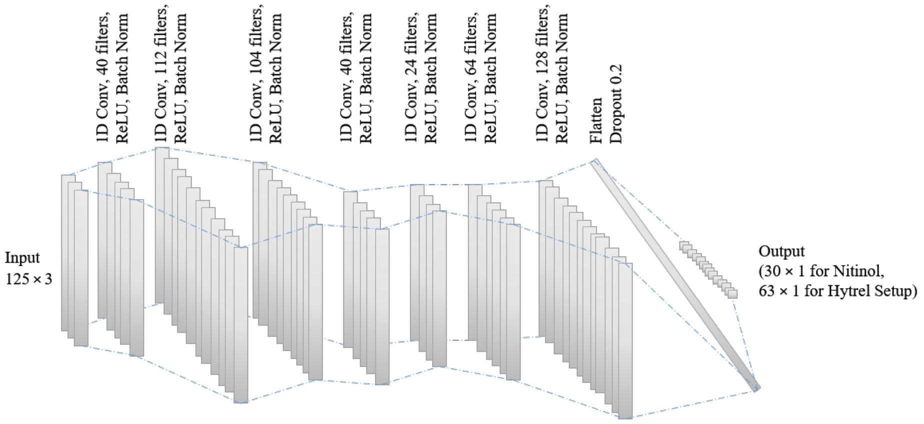

Figure 4. The configuration of the selected network. *Conv: convolutional layer, Norm: normalization.

3. RESULTS AND DISCUSSION

3.1 Feasibility of using low-cost interrogators

One of the main challenges in fiber sensor industrialization is the cost of their interrogation system. We investigated the feasibility of using a low-cost system for Edge-FBG sensors. In intensity-based sensors, it is vital that the level of noise in measured amplitudes at FBG wavelengths is low enough such that the amplitude ratio caused by bending can be detected. As we are only interested in changes in the amplitude ratio between the FBG peaks, the global intensity variations, which cause a linear amplitude change in the adjacent Bragg peaks, can be neglected. However, the spectrum profile in low-cost FBG interrogators might show instabilities over time (Figure 5(a)), as the implemented light sources are often not supported by temperature or current controllers. These ripples can cause errors in the amplitude ratio measurements. To estimate the level of this systematic error inside our interrogator, we monitored the temperature and the spectrum profile of the light source for several hours.

The graph in Figure 5(b) shows changes of the spectrum profile 1 hour, 2 hours, and 3 hours after starting the interrogator. As can be seen, within the first two hours, changes in the spectrum profile are significant. Calculating the attenuation between the spectra taken 2 and 3 hours after starting the interrogator shows that the ripples are still not stable and may cause an error in the measured amplitude ratio at Bragg wavelengths (Figure 5(c)). During our experiment, we observed that two factors could cause these changes: thermal variations and intrinsic instability of the interrogator. For instance, in an interval of five hours, where the temperature was fixed at 25.2 ℃, the amplitude ratio between the FBGs of the third Edge sensor changed for 0.002 a.u. In a similar time interval, when temperature variations of 0.2 ℃ (25.2 ℃ - 25.4 ℃) were detected, the amplitude ratio changed twice as much as it did in the fixed temperature environment. These observations demonstrate the sensitivity of the ripples on the spectrum profile to even sub-degree thermal variations. These systematic errors make the signals coming from small deflections unrecognizable and will be hidden in the noise. Therefore, to detect small deflections, a data acquisition setup with a higher signal-to-noise ratio, including a more stable light source and higher resolution spectrometer, would be needed. Nevertheless, the signal level for medium to large deflections is in the order of few tenths of a.u., which can be detected even if sub-degree thermal variations occur, or the measurements last for several hours. Therefore, it is feasible to use the current setup for detecting medium and large deflections with an Edge sensor.

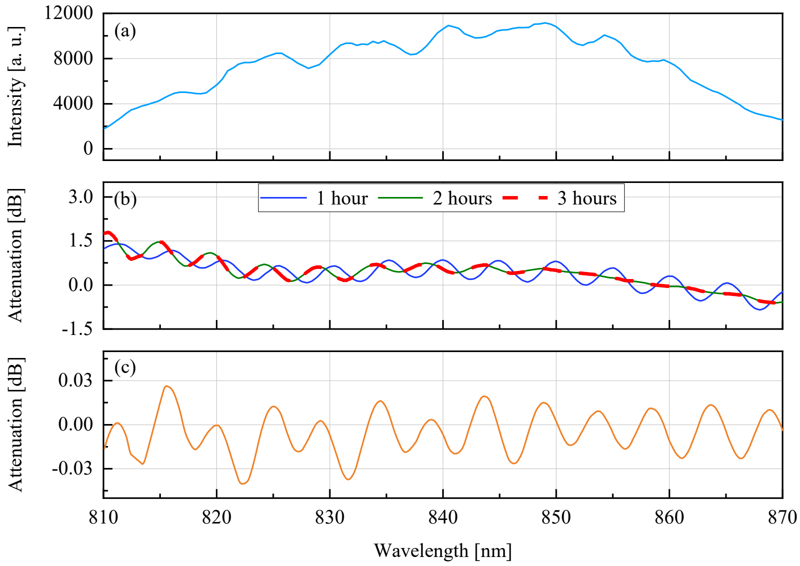

Figure 5: (a) Spectrum profile of the MIOPAS interrogator. (b) The calculated attenuation between the reference spectrum and measured spectrums after 1 hour, 2 hours, and 3 hours. (c) The calculated attenuation between the spectra measured 2 and 3 hours after the reference spectrum.

3.2 Evaluation of the deep learning model

In this section, we discuss the impact of the kernel size on the outcome of the selected architecture. A more thorough analysis of the other parameters' influence in the search space will be done in future work. As shown in Figure 6(a), the model consisting of CNNs with a kernel size of 1 reaches a plateau already after 1000 epochs, and the training loss does not improve any further. Although the models with larger kernel sizes need more extended training to converge, they can achieve lower training losses. Higher validation loss than training loss means that the optimized model based on the training samples does not generalize for making accurate predictions when applying to the validation set. The frequent appearance of a high validation loss for different epochs shows the difficulty level of training. Figure 6(d) shows how these fluctuations disappear as the training loss decreases.

The scores for different kernels over the testing set, including the tip error and the RMSE in both medium and large deflection setups, are respectively shown in Figures 7(a) and (b), where the testing dataset is 10% of the total number of samples. It can be noticed that in the medium deflection setup, the kernel size of 1 can only achieve a median tip error of 12 mm and a median RMSE of 7 mm. However, the kernel size of 25 indicates the least prediction error among others, resulting in a median tip error of 5.3 mm and a median RMSE of 3.3 mm. In the large deflection setup, the Huber loss's median value drops significantly for larger kernel sizes, which results in a median value of 5.8 mm in tip error and 3.4 mm in RMSE for a kernel size of 25. Although the applied shapes are more complicated than the Nitinol-protected sensor, and the output dimension of the network is almost doubled, the model is still able to make shape predictions with the same accuracy level. The model consists of CNNs with a kernel size of 25 is then selected for detecting both medium and large deflections, which can make predictions over unseen data in less than 500 µsec when running on a GPU (GeForce RTX 2080). This means that Edge sensors not only can be interrogated with a low-cost system but can also be trained to make predictions using low-power CPU-based devices. Moreover, the accuracy improvement from kernel size of 1 to 25 suggests that further increment of kernel size can get the current architecture closer to the optimal design.

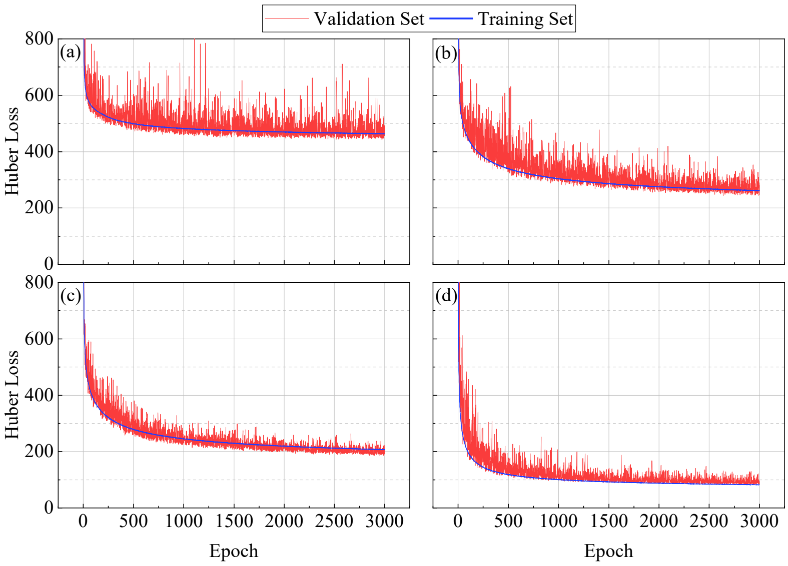

Figure 6. The training and validation Huber loss (δ = 5) of the selected network with kernel size of (a) 1, (b) 3, (c) 5, and (d) 25 in the convolutional layers (large deflection dataset).

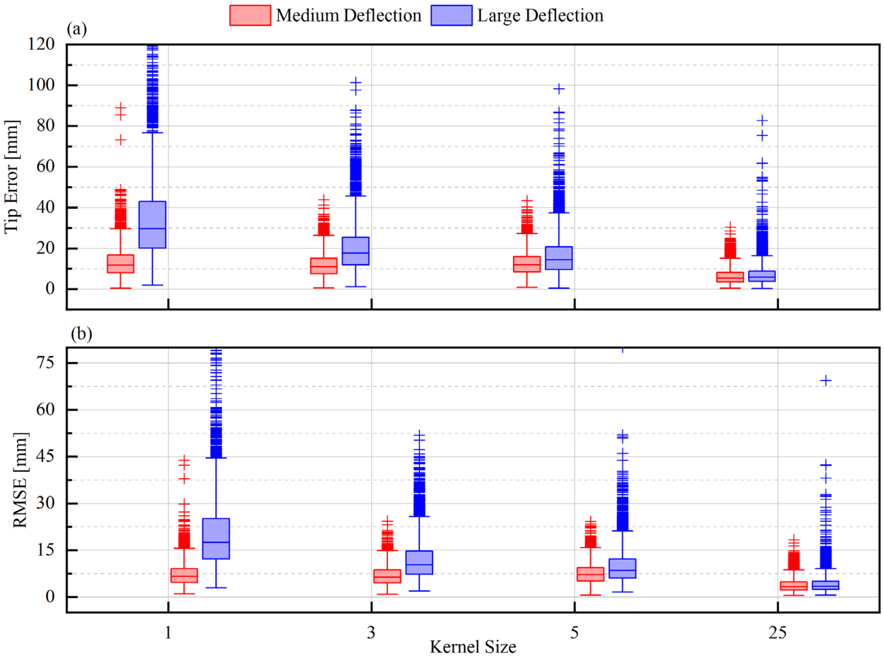

Figure 7. Shape evaluation parameters for kernel sizes of 1, 3, 5, and 25 over the testing dataset in medium and large deflection setup. On each box, the median is indicated with a central mark, and the 25th and 75th percentiles are indicated with the bottom and top edges of the box, respectively. The whiskers show the minimum and maximum values within each group not considered outliers, and the outliers are marked with the '+' symbol. Some outliers are excluded for better visualization of the median values.

The error distribution of the real and the predicted position of the markers are illustrated in Figure 8. As can be seen, the median value increases towards the end of the fiber sensor. This accumulative error can be explained by Figure 9, which shows two examples of the predicted shape in large deflection. In Figure 9 (a), the model was able to predict the shape with less than 3 mm RMSE and 2.2 mm tip error. In Figure 9 (b), although the model nicely predicted the overall shape, it could not correctly estimate the curve's initial orientation, which led to a tip error of 18.9 mm. The inaccuracy of the predicted bending direction at the sensor's inlet can be due to the gap between the v-clamp and the first Edge sensor. In this gap, no sensing node is present, and only the spectrum profile changes depending on the applied curvature. However, inaccurate prediction in the bending orientation suggests that the spectrum profile is more sensitive to the curvature than its direction. The low sensitivity of this part of the fiber to the bending direction leads to large shape prediction errors, especially for Hytrel protected sensor. Therefore, to achieve a more accurate shape estimation, this gap between the v-clamp and the first sensing node should be minimized. Another reason for the inaccuracy in some of the predicted shapes can be the manual movement of the fiber during data acquisition, which was not limited to a specific volume. Consequently, the samples used for training the model might slightly be biased to certain shapes. One possible solution for this issue is to define a constrained volume for the fiber and automate the shape manipulation process such that the training and testing data correspond to the same workspace.

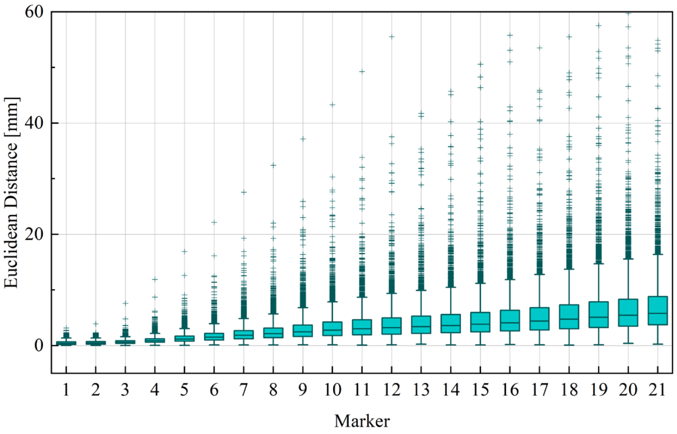

Figure 8. The error distribution of the real and the predicted positions of the markers (large deflection dataset). Some outliers are excluded for better visualization of the median values.

For robustness testing, a new set of data was collected roughly half an hour after the training data acquisition. The median values of the tip error and the RMSE for the predicted shapes increase to 15 mm and 9 mm in the medium deflection setup. The evaluation parameters went up to 30 mm and 18 mm for large deflections. In the time interval between the data acquisitions, we let the tracking system run, which causes thermal variations around the sensor by constantly sending IR pulses to scan the markers. The high prediction error shows the importance of the environmental condition, including temperature, on the spectrum profile that limits the model's accuracy. In future work, we will investigate possible solutions to reduce the impact of thermal variations on prediction accuracy.

4. CONCLUSION

In this work, a new technique was developed for modeling Edge-FBG shape sensors. We used a low-cost interrogator and designed a deep neural network using the Keras tuner framework to directly estimate the sensor's shape based on the full spectrum of the Edge-FBG array. Although there is still room for improvement, this pilot study shows that the Edge sensor's shape can be estimated given its spectrum profile. The hyperparameter optimization points towards simple network architectures, thus enabling these networks also to be run on very simple embedded processors. These findings open new possibilities for real-time shape sensing applications based on low-power devices and inexpensive interrogators.

The key advantage of our method in comparison to the standard sensor characterization technique, in which the fiber's shape is estimated by measuring the mode field dislocation, is that the shape is predicted based on the full spectrum of the Edge sensor, meaning that it takes into account the effect of other bending-related phenomena on the spectrum profile.

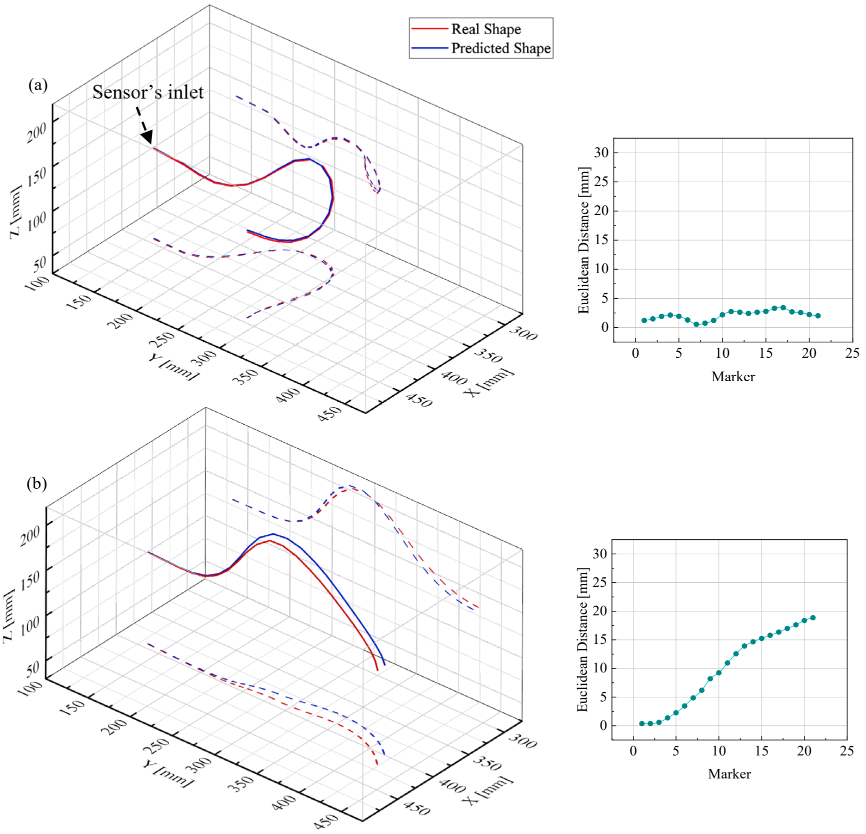

Figure 9. (a) a typical case, (b) an outlier of predicted shapes using the proposed model (large deflection dataset). The dash lines represent the XY and YZ projections in the 3D graphs. The 2D graphs on the right, show the absolute error between the real and the predicted position of all markers.

For future work, we plan to use a data acquisition setup with a higher signal-to-noise ratio for measuring the Edge-FBG spectrum, including a more stable light source and a higher resolution spectrometer to detect small deflections. Limiting the volume in which the sensor moves and automating the shape manipulation process can ensure that the training and testing data correspond to the same workspace. Moreover, we intend to continue investigating other network architectures for further improvements in shape estimation.

REFERENCE

[1] R. J. Roesthuis, S. Janssen, and S. Misra, "On using an array of fiber Bragg grating sensors for closed-loop control of flexible minimally invasive surgical instruments," in *IEEE/RSJ International Conference on Intelligent Robots and Systems*, 2013, pp. 2545–2551.

[2] S. C. Ryu and P. E. Dupont, “FBG-based shape sensing tubes for continuum robots,” in *IEEE International Conference on Robotics and Automation (ICRA)*, 2014, pp. 3531–3537.

[3] C. Waltermann *et al.*, “Femtosecond laser processing of evanescence field coupled waveguides in single mode glass fibers for optical 3D shape sensing and navigation,” in *Proc. of SPIE*, 2015, vol. 9480, p. 948011.

[4] B. J. Soller, D. K. Gifford, M. S. Wolfe, and M. E. Froggatt, “High resolution optical frequency domain reflectometry for characterization of components and assemblies,” *Opt. Express*, vol. 13, no. 2, p. 666, 2005.

[5] R. R. Thomson *et al.*, “Ultrafast laser inscription of a three dimensional fan-out device for multicore fiber coupling applications,” *Opt. InfoBase Conf. Pap.*, pp. 4–5, 2008.

[6] M. Cohen, R. Shavit, and Z. Zalevsky, *Planar Waveguides and other Confined Geometries*, vol. 189. Springer New York, 2015.

[7] S. Manavi, L. Witthauer, L. Iafolla, A. Zam, G. Rauter, and P. C. Cattin, “Temperature-compensated FBG-based 3D shape sensor using single-mode fibers,” *OSA, Adv. Photonics,* p. JTu6C.1, 2018.

[8] J. Yi, X. Zhu, H. Zhang, L. Shen, and X. Qiao, “Spatial shape reconstruction using orthogonal fiber Bragg grating sensor array,” *Mechatronics*, vol. 22, no. 6, pp. 679–687, Sep. 2012.

[9] C. Waltermann *et al.*, “Multiple off-axis fiber Bragg gratings for 3D shape sensing,” *Appl. Opt.*, vol. 57, no. 28, p. 8125, 2018.

[10] L. Faustini and G. Martini, “Bend loss in single-mode fibers,” *J. Light. Technol.*, vol. 15, no. 4, pp. 671–679, 1997.

[11] T. O’Malley *et al.*, “Keras {Tuner},” in *https://github.com/keras-team/keras-tuner*.

[12] P. J. Huber, “Robust Estimation of a Location Parameter,” *Ann. Math. Stat.*, vol. 35, no. 1, pp. 73–101, Mar. 1964.

Chapter 6

Advanced Study on Using Deep Learning to Model Edge-FBG Shape Sensors

The publication presented in this chapter describes a more thorough investigation of modeling edge-FBG sensors with deep learning algorithms. In this study, we first analyzed various data transformations on the edge-FBG spectra and the sensor's 3D shape. We then optimized the hyperparameters of a convolutional neural network. We set a more advanced search space in the hyperparameter optimization algorithm to achieve a better performing configuration that can reach higher shape prediction accuracy with a median tip error of $4.4\,\mathrm{mm}$. We were able to achieve further improvements and reduce the median tip error of the shape prediction to $3.1\,\mathrm{mm}$ by upgrading the network's architecture according to the Siamese design.

This is the submitted version of the following manuscript:
Samaneh Manavi Roodsari, Antal Huck-Horvath, Sara Freund, Azhar Zam, Georg Rauter, Wolfgang Schade, Philippe C. Cattin. Using Supervised Deep-Learning to Model Edge-FBG Shape Sensors.
The preprint version is available online at https://doi.org/10.48550/arXiv.2210.16068.

Using Supervised Deep-Learning to Model Edge-FBG Shape Sensors

Samaneh Manavi Roodsari[a], Antal Huck-Horvath[a], Sara Freund[a], Azhar Zam[b,c], Georg Rauter[d], Wolfgang Schade[e], Philippe C. Cattin[a]

[a] *Center for medical Image Analysis and Navigation (CIAN), Department of Biomedical Engineering, University of Basel, Gewerbestrasse 14, Allschwil, 4123, Switzerland*
[b] *Division of Engineering, New York University Abu Dhabi, Abu Dhabi, 129188, UAE*
[c] *Tandon School of Engineering, New York University, Brooklyn, NY, 11201, USA*
[d] *Bio-Inspired RObots for MEDicine-Laboratory (BIROMED-Lab), Department of Biomedical Engineering, University of Basel, Switzerland*
[e] *Department of Fiber Optical Sensor Systems, Fraunhofer Institute for Telecommunications, Heinrich Hertz Institute, HHI, Am Stollen 19H, Goslar, 38640, Germany*

Abstract

Continuum robots in robot-assisted minimally invasive surgeries provide adequate access to target anatomies that are not directly reachable through small incisions. Achieving precise and reliable motion control of such snake-like manipulators necessitates an accurate navigation system that requires no line-of-sight and is immune to electromagnetic noises. Fiber Bragg Grating (FBG) shape sensors, particularly edge-FBGs, are promising tools for this task. However, in edge-FBG sensors, the intensity ratio between Bragg wavelengths carries the strain information that can be affected by undesired bending-related phenomena, making standard characterization techniques less suitable for these sensors. We showed in our previous work that a deep learning model has the potential to extract the strain information from the full edge-FBG spectrum and accurately predict the sensor's shape. In this paper, we conduct a more thorough investigation to find a suitable architectural design with lower prediction errors. We use the Hyperband algorithm to search for optimal hyperparameters in two steps. First, we limit the search space to layer settings, where the best-performing configuration gets selected. Then, we modify the search space for tuning the training and loss calculation hyperparameters. We also analyze various data transformations on the input and output variables, as data rescaling can directly influence the model's performance. Moreover, we performed discriminative training using the Siamese network architecture that employs two CNNs with identical parameters to learn similarity metrics between the spectra of similar target values. The best-performing network architecture among all evaluated configurations can predict the sensor's shape with a median tip error of 3.11 mm.

Keywords: Supervised deep learning, shape sensing, bending birefringence, bending loss, edge-FBG, fiber sensor, curvature sensing

---

1. Introduction

Minimally invasive surgical procedures (MIS) are delicate operations performed through small incisions or natural orifices on anatomical structures of the human body. Such interventions are beneficial compared to conventional open surgeries, as they reduce patient trauma, shorten recovery time [1], and ensure overall cost-effectiveness [2]. In addition, surgical robots help to realize the full potential of MIS procedures by enhancing dexterity and manipulability, as well as improving stability and motion accuracy [2]. Continuum robots play an important role in complex robot-assisted MIS procedures, where no adequate and direct access through small incisions to target anatomies is available [1, 3, 4, 5, 6, 7, 8]. However, achieving precise and reliable motion control of continuum robots requires accurate and real-time shape sensing. Accurately modeling the shape of these instruments remains challenging due to their inherent snake-like design and inevitable collisions with the surrounding tissues during the surgery [9, 10]. Therefore, a precise and accurate tracking system is needed to enable closed-loop control for such flexible manipulators.

The most common and commercially available medical tracking systems include optical tracking systems [11, 12], electromagnetic sensors [11], intraoperative imaging technologies [13], angular sensors [14, 15], and FBG-based sensors [14]. Optical trackers are state-of-the-art technology for tracking medical tools and patients inside the operating room (OR). The optical trackers consist of cameras that detect navigation markers attached to the object of interest. They can navigate up to 25 tools with sub-millimeter accuracy over a large measurement volume (*e.g.,* Polaris NDI $\sim 0.12\,\mathrm{mm}$ RMS (root-mean-square) over a volume of $\sim 2\,\mathrm{m}^3$ [11]). Wireless tracking, reliable measurement, and stable performance are the other key advantages of this technology. However, they require a line-of-sight and are best suited to use with large, rigid tools. These substantial limitations make optical trackers unsuitable for navigating flexible endoscopes inside the patient's body.

Electromagnetic (EM) tracking systems consist of two key components, field generators and wired sensor coils. The field generator emits a defined low-intensity EM field which establishes the measurement volume (*e.g.,* AURORA NDI, Planar 20-20 FG 75 cm^3 [11]). Once the sensors enter the measurement volume, a small current is induced inside them, which is then used to determine the position and orientation of the sensor relative to the patient. This technology allows intracorporeal tracking, as it does not require a line-of-sight and can be embedded or placed at the tip of flexible tools. However, EM tracking systems are less accurate than optical trackers and have a smaller working volume. Adding multiple sensors along the endoscope is often impossible, as the sensors must be wired. Furthermore, they are sensitive to environmental EM interferences (*e.g.,* the EM field of the robot) and to the presence of conductive or ferromagnetic metals.

Intraoperative imaging modalities, including fluoroscopy, cone-beam CT, and ultrasound, can be an alternative to EM sensors for intracorporeal tracking. Some imaging modalities like biplane fluoroscopy achieve even higher accuracy as compared to EM sensors (mean shape error of 0.54 mm [13]) but are challenging to perform in crowded OR settings. In addition, they have limitations such as high doses of radiation (*e.g.,* X-ray-based imaging), high computational cost (*e.g.,* cone-beam CT), and low resolution (*e.g.,* ultrasound).

In FBG-based shape sensors, the main components are a sensing probe (coated optical fibers) and an interrogation system for measuring the sensor's signal. FBG sensors can track themselves in three dimensions, thus providing real-time feedback on the shape and tip location when inserted into flexible instruments. These sensors are easily integrable into medical devices for tracking, as one single fiber with a typical diameter of 250 µm can carry an array of FBGs to extract strain information along the length of the fiber. Moreover, FBG sensors are immune to EM interferences and are applicable for navigating robotic tools. The coating layer of the optical fiber can be a bio-compatible material, which makes it suitable for tracking catheters as well [16].

Although different configurations for FBG-based shape sensors have been studied in recent years [16, 17, 18, 19, 20, 21, 22], the only fiber shape sensors that have been commercialized work based on multicore fibers (*e.g.,* [23, 24]).

Multicore fiber shape sensors are able to track themselves with a millimeter range accuracy (*e.g.,* an average error of 1.13 mm for a 38 cm long sensor [20]). However, the cost of such systems is quite high [25], as an optical frequency domain reflectometer (OFDR) is needed for interrogating the FBGs [26], plus a fan-out device for reading the signal from each core [27]. Recently, a new configuration for FBG-based shape sensing, called edge-FBG, has been proposed by Waltermann *et al.* [28], in which the FBGs are inscribed on the edge of the core in a single-mode optical fiber. Unlike standard FBG-based shape sensors, edge-FBG sensors are intensity-based, and the strain information is carried by the intensity ratio between the Bragg wavelengths. Such sensors can be interrogated using a broadband light source and a low-cost spectrometer, making the edge-FBG sensor a suitable choice for many applications where the price should be relatively low.

As explained in [28], the mode field's center in a single-mode fiber is sensitive to shape deformations and moves towards the opposite direction of bending. Depending on the radial and the angular distance between the dislocated mode field and the edge-FBGs, the intensity ratio between the edge-FBGs at each sensing plane changes. In this method, the curvature and the bending direction can be calculated from the estimated mode field centroid, and a shape reconstruction accuracy of ~5 cm for a 25 cm long sensor can be achieved [29]. However, in such eccentric FBGs, the intensity values at the Bragg wavelengths also depend on the spectrum profile of the incident light. Macro bending in optical fibers may affect the spectrum profile by causing wavelength-dependent attenuation [30]. Moreover, in curved areas of an optical fiber, the refractive index profile is asymmetric (known as bending-induced birefringence), and therefore, changes in the light's polarization state are wavelength-dependent [31]. Consequently, polarization-sensitive elements inside the FBG interrogation system may modify the spectrum profile by attenuating each wavelength element differently and cause errors in intensity measurements.

The authors showed in [18] that considering the complicated impact of bending-induced phenomena on the signal of edge-FBG sensors, it is feasible to model such sensors using deep learning techniques that predict the sensor's shape based on the full spectrum and not only the intensity at Bragg wavelengths. Meaning that it is already considering the effect of bending-related phenomena on the spectrum profile.

In this paper, we investigate the usage of deep learning algorithms for modeling edge-FBG sensors in more detail. First, we focus on identifying a good set of tuning parameters, known as hyperparameters, for our deep learning algorithm to extract relevant features from the edge-FBG sensor. We perform this hyperparameter tuning when the model's input (the sensor's spectra) and output data (the sensor's spatial shape) are preprocessed using different rescaling methods. Ultimately, we employ the most suitable data rescaling approach and the optimized feature-extracting network to perform discriminative training using the Siamese network [32].

2. Methodology

The importance of choosing a good set of hyperparameters for a deep learning algorithm is well-known. The Hyperband, as one of the most common hyperparameter optimizers, considers several possible resource allocations (*e.g.,* the total number of epochs used during evaluation) and invokes Successive Halving [33] on randomly sampled hyperparameter configurations [34]. Compared to black-box approaches like Bayesian optimization, the Hyperband is 5× to 30× faster and evaluates an order-of-magnitude more configurations [34]. In addition to the hyperparameter configuration, rescaling input and output variables before being presented to deep neural networks greatly affects the model's performance [35]. When input variables have large values, the model learns large weights, which may cause numerical instability, poor performance during training, and generalization error in the network. Large-scaled target values result in significant update rates in weight values, making the learning process unstable. In common practices, preprocessing transformations are applied to input variables prior to training the networks, and postprocessing steps are introduced to the model's predictions for calculating the desired target values [35]. Therefore, we investigate different rescaling methods on the input and output variables to identify the most suited data preprocessing steps.

2.1. Training Setup

The dataset used in this work is from [18] with almost 53000 samples. Each sample consists of three consecutively measured edge-FBG spectra, the intensity values of 125 wavelength elements from 812 nm to 871 nm, as the input and the spatial coordinates of 21 discrete points along the fiber's length as corresponding target values. These discrete points are the positions of re-

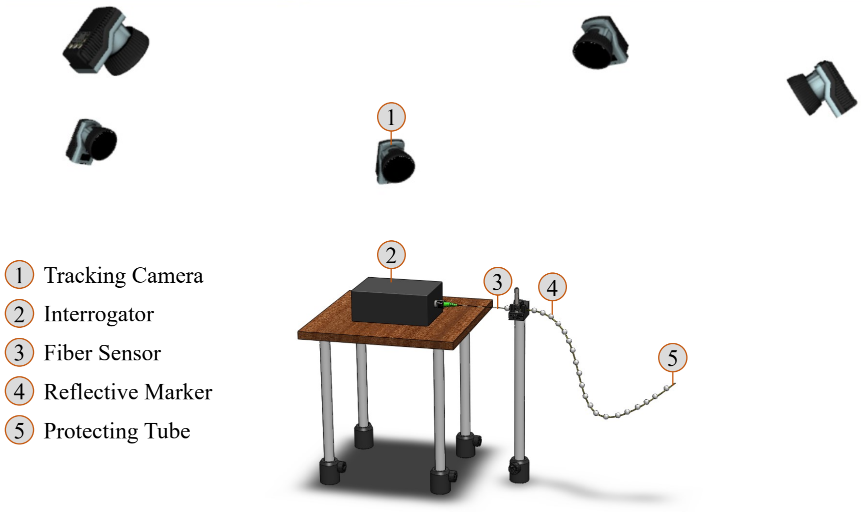

Figure 1: The data acquisition experimental setup of the edge-FBG sensor. Five tracking cameras (Oqus 7+) are used to monitor the sensor's shape. The sensor is inserted into a Hytrel furcation tubing to protect the fiber during shape manipulation.

flective markers that we attach to the sensor and monitor using a motion capture system. Figure 1 shows a schematic of the experimental setup. The FBG spectrum contains the reflected signal of 15 edge-FBGs from five sensing planes. Each sensing plane has three co-located FBGs at the left, top, and right edge of a single-mode fiber's core (SM800p from FIBERCORE company, UK).

We use the Hyperband algorithm, built in the Keras tuner [36], to perform hyperparameter optimization in two steps. First, a bigger search space is defined to optimize the settings of 1D convolutional layers (conv1D) and pooling layers (search criteria can be found in Table 3 in the appendix). For this hyperparameter tuning step, the number of conv1D layers is set to seven. Based on our observations when investigating various search criteria, the network with seven conv1D is deep enough for feature extraction. Then, we fix these layer settings and modify the search space to tune the loss function, the optimizer, and the dropout rate (more detail on the search criteria is available in Table 4 in the appendix). The model's input and output data are preprocessed using various data rescaling methods in this hyperparameter tuning step. The objective of the Hyperband is set to be the root-mean-square error on the validation set so that the scale of the scores, assigned to suggested configurations, is not affected when different loss functions get selected. As the Hyperband is based on a random search, we repeat each hyperparameter search three times for statistical robustness before selecting the final settings. To evaluate the predictive performance of the proposed model in an unbalanced way, the dataset is split into mutually disjoint Train-Validation-Test subsets: 80% for training, 10% for validating, and 10% for testing.

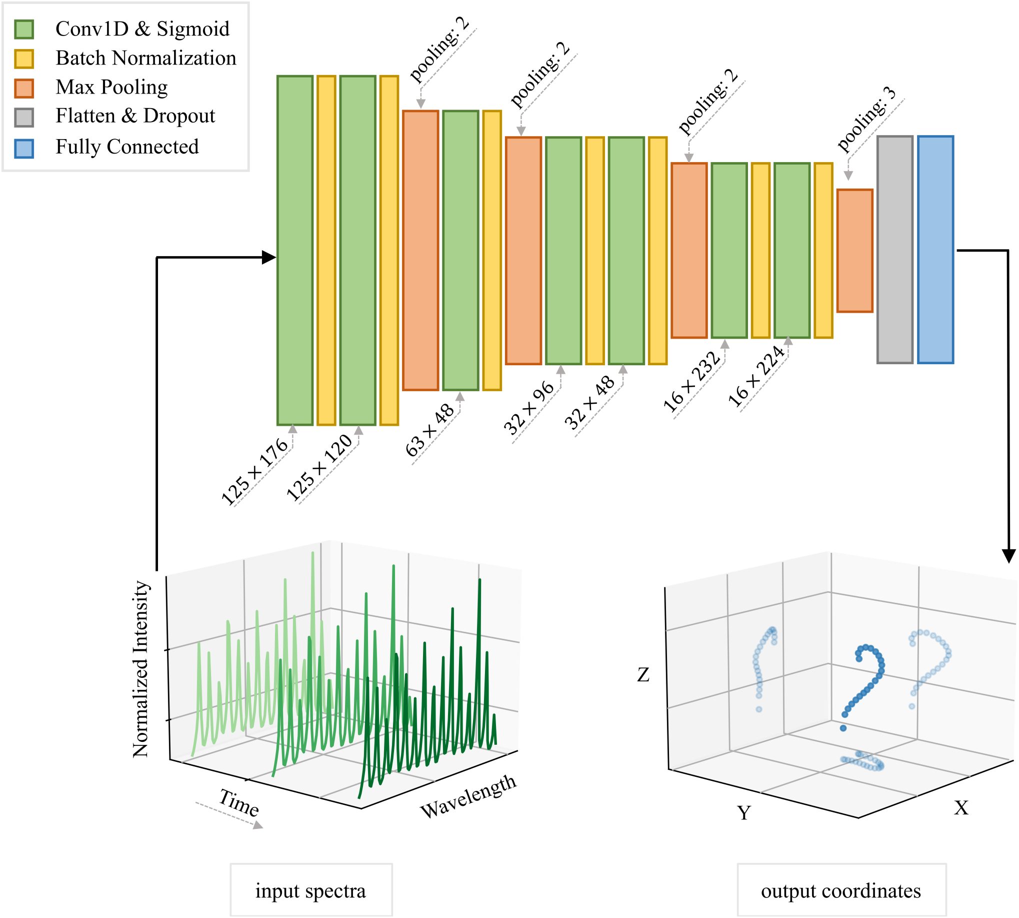

Figure 2: The architecture of the best-performing configuration after the first step of hyperparameter search. For this network, the input data is three consecutive edge-FBG spectra, normalized using one-dimensional z-scaling (see Section 2.2 for more details), and the output data is the absolute coordinates of 21 discrete points along the sensor's length. The channel sizes of the seven 1D convolution layers (conv1D) are 176, 120, 48, 96, 48, 232, and 224, respectively. The pooling sizes of the four max pooling layers are 2, 2, 2, and 3, respectively.

We investigated various configurations in the first hyperparameter tuning step. Figure 2 shows the best-performing architecture among the suggested configurations, in which each conv1D layer is followed by a Sigmoid activation function and batch normalization. The kernel size for the conv1D layers is 10. Four max pooling layers are placed after the conv1D layers number two, three, five, and seven for down sampling the features. The final layer is a fully connected layer with a linear activation function to map the extracted features into desired target values. These hyperparameters are fixed for the remainder of this paper.

2.2. Input Data Preprocessing

As mentioned earlier, the intensity ratios between Bragg wavelengths of co-located FBGs carry the strain information. Therefore, the input variables should not be normalized/standardized independently. We investigate two preprocessing transformations on the input variables, one-dimensional and multi-dimensional z-scaling [37]. In the first method, we apply the standard scaling technique, considering the input data as a one-dimensional vector. The data distribution after rescaling has a zero mean value, and its standard deviation is one. Figure 3(a) and (b) show the data distribution before and after rescaling. In the second method, we apply multi-dimensional standard scaling [37] by subtracting each wavelength element from its mean value and dividing them over the square root of the covariance matrix

$$Z = UD^{-1/2}U^{t}(X - \mu), \tag{1}$$

where U and D are the Eigenvectors and the Eigenvalues of the covariance matrix, X is the input data (sensor's spectra), and μ is the mean intensity value at each wavelength element over the training dataset. With this approach, we achieve an approximately Gaussian density distribution (see Figure 3(c)).

2.3. Output Data Preprocessing

In this section, we consider the measured coordinates of each marker as a point cloud and investigate the model's performance when various preprocessing transformations are applied to these point clouds (for more details, see the appendix). In the first method (M1), we translate each point cloud

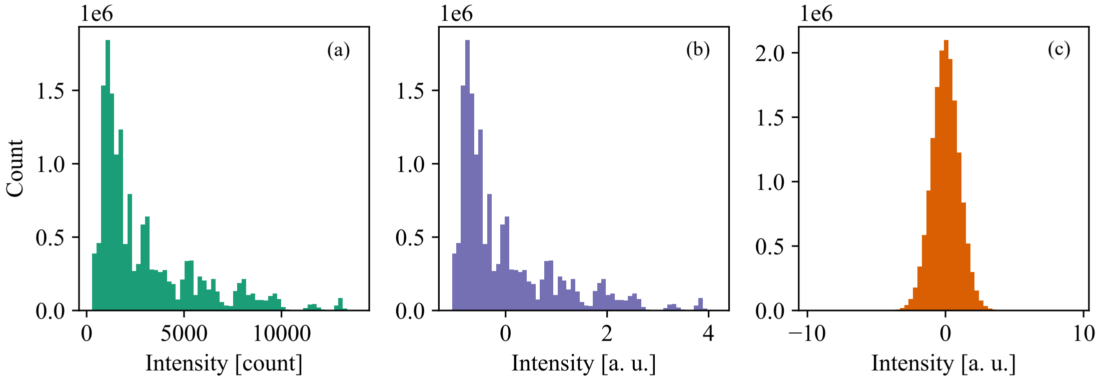

Figure 3: The histogram of the flat original input data (a), normalized input data using one-dimensional (b), and multi-dimensional z-scaling (c). The density distribution when using multi-dimensional z-scaling is approximately Gaussian, with skewness of ~ 0.003 and kurtosis of ~ -1.2.

to the origin of the global frame by subtracting the mean coordinate values from the original coordinates. We calculate the radial distance of the points from the cloud's center in all markers and compute its mean value. We then divide the translated coordinates by this calculated mean radial distance. In this method, the spatial coordinate elements for each marker have different scaling from the original data, but their density profile remains unchanged (see Figure 4). In the second approach (M2), each already translated point cloud is rescaled based on the mean of the radial distance of its own points, and therefore, the scaling factor is different for each point cloud. For the third method (M3), we apply a three-dimensional standard scaling to each point cloud. This way, the transformed data is uncorrelated, and the density profiles are different from the original ones. Lastly, as the fourth method (M4), we use the relative coordinates between the markers instead of absolute coordinate values. Figure 4 shows how the distribution of the coordinate elements changes when applying different preprocessing transformations to the target values.

2.4. Siamese Network

A further improvement of the network's performance was possible by guiding the feature-extracting part of the network in selecting relevant features for a given spectral sample [38, 39]. The Siamese network [32] is an architecture, designed for learning similarity metrics, which is well known from face recognition [40, 41] and handwritten forgery detection applications [32, 42]. A Siamese network usually takes two inputs, compares them in the feature space, and provides a similarity measure between the two feature vectors. Siamese architectures consist of two identical subnetworks (the feature extractors) with shared weights that are trained using paired samples corresponding to similar (genuine) or dissimilar (imposter) outputs/pairs. During training, the feature extractor subnetworks are forced to provide vectors close to each other when the inputs belong to the same groups and are far away from each other if they are from different groups.

In our implementation, shown in Figure 5, we use the same layer settings

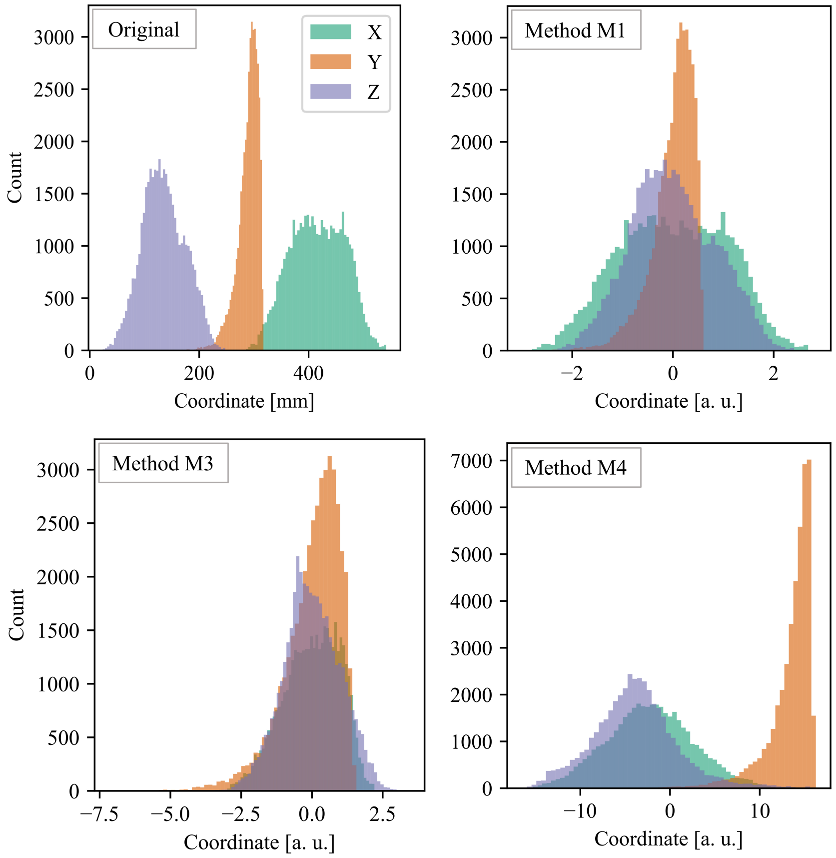

Figure 4: The histograms of the original x-, y-, and z-coordinates, their normalized values using M1 and M3, and the relative values using M4 for the point cloud number 10 are shown. The histogram of processed values using methods M2 is not depicted, as the distributions of x, y, and z coordinates are similar to M1.

for feature extraction as in the architecture explained in Section 2.1. We calculate the Euclidean distance between the two feature vectors, apply batch normalization, and pass it through a single-unit fully connected layer followed by a Sigmoid activation function. The output of the Sigmoid activation function gives a value close to one for distant feature vectors and a value close to zero for close vectors. In parallel, the feature vectors are also passed into two fully connected layers. The first one has 1344 units followed by a Sigmoid activation function, and the second one is similar to the last layer of the previous architecture (compare Figure 2), in which the preprocessed coordinates are calculated. We group the samples using the RMSE, that is, the root-mean-square of the Euclidean distance between the corresponding shapes. First, we calculate the RMSE for all possible pairs in the training dataset. We then define the 1^{st} and the 25^{th} percentiles in the RMSE's histogram as thresholds for labeling the samples. These limits are selected after studying various combinations. If the calculated RMSE between two samples is less than the lower limit, we label the samples as zero (genuine pairs), and if it is within a 1% range around the upper limit, we label them as one (imposter pairs).

The following loss function is used for this Siamese network:

$$\begin{aligned}\text{Loss} = \text{mean}\Big(& \alpha\left((1-y_{\text{true}})\, y_{\text{pred}}^2 + y_{\text{true}} \max(0, M - y_{\text{pred}})^2\right) \\ & + (1-\alpha)\big(L(y_A - y_a) + L(y_B - y_b)\big)\Big)\end{aligned} \tag{2}$$

where,

$$L(a) = \begin{cases} 0.5\,\frac{a^2}{\delta} & |a| \leqslant \delta, \\ 0.5\,\delta + (|a| - \delta) & \text{otherwise.} \end{cases} \tag{3}$$

In definition (2), α is a scalar coefficient to weight loss contributions of the three model's outputs, and δ is a hyperparameter defining the range for mean-absolute-error, and mean-square-error in L, a modified version of Huber loss function [43]. M is the margin, y_{true} is the true label of paired samples, y_{pred} is the output of the right arm, y_A and y_B are the true relative coordinates, and y_a and y_b are the predicted relative coordinates in the left and the middle arms of the network (Figure 5). The partial loss, calculated from y_{pred}, is the Contrastive loss [44]. Depending on whether the inputs are a genuine/imposter pair, the first or the second part of the Contrastive loss

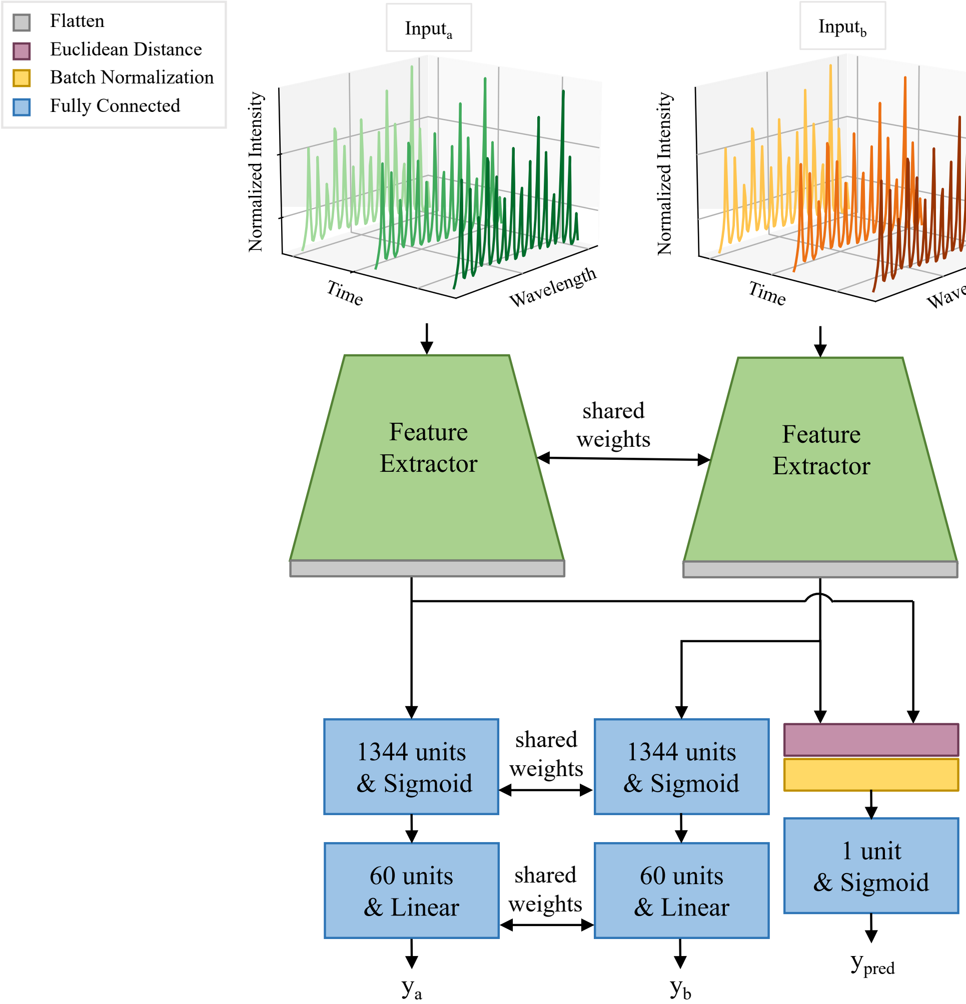

Figure 5: The architecture of the Siamese model. The feature extractor subnetworks have a similar architecture to what is shown in Figure 2, but without the dropout and the fully connected layers.

is applied to the output of the network's right arm. The two L loss functions are calculated from predicted relative coordinate values in the left and middle arms of the network (Figure 5). For a genuine pair, the network pushes y_{pred} towards zero, such that the first part of the Contrastive loss also gets closer to zero. If the inputs are an imposter pair, y_{pred} is forced to be larger than the value of M, such that the feature vectors stay separated in the feature space. Similar to the data preprocessing Sections 2.2 & 2.3, the training hyperparameters for this network, including the optimizer's parameters, M,

Table 1: Shape evaluation errors on the test dataset when the input data are preprocessed using one-dimensional and multi-dimensional normalization methods. IQR: interquartile, one-dim.: one-dimensional normalization, multi-dim.: multi-dimensional normalization.

	tip error [mm]		**RMSE** [mm]	
method	median	IQR	median	IQR
one-dim.	4.46	4.30	2.74	2.39
multi-dim.	13.38	11.34	8.11	5.76

α, and δ, were tuned using the Hyperband algorithm (see Table 5 in the appendix for the search criteria). We ran the Hyperparameter search multiple times and selected the best-performing architecture for final training.

3. Results

Evaluating the performance of the configurations suggested by the Hyperband is done by calculating the shape evaluation metrics between the true and the predicted shapes. Shape evaluation metrics include the tip error (the Euclidean distance between the true and the predicted coordinate of the sensor's tip) and the RMSE. The best-performing architecture among the three hyperparameter search attempts for each normalization method is selected based on the median values of the shape evaluation metrics in the validation dataset.

Table 1 shows the error values for the two input normalization methods. The one-dimensional normalization method, which preserves the distribution profile of the input data, results in a median tip error and a median RMSE of 4.46 mm and 2.74 mm, respectively. In the multi-dimensional normalization approach, the median values are 13.38 mm and 8.11 mm, respectively, which are significantly higher compared to the one-dimensional normalization method. This might be due to the validation loss reaching its plateau quicker when the input data distribution is approximately Gaussian (shown in Figure 6). The one-dimensional normalization method is therefore selected as the input data preprocessing step for the remainder of this paper.

The error statistics for shape evaluation metrics when using different preprocessing methods on the target data are shown in Table 2. Among the three preprocessing approaches applied to the absolute coordinate values (M1, M2, and M3), the first method (M1) shows the lowest error values with a median tip error of 4.68 mm and a median RMSE of 2.83 mm. However, the network performs better in predicting relative coordinates (M4) compared to absolute values by resulting in the median value of 4.36 mm for the tip error and 2.78 mm for the RMSE. Therefore, the relative coordinate values are selected as the best-performing target data preprocessing. The last row in Table 2 shows the shape evaluation parameters of the Siamese network when using the best-performing data preprocessing on both input and target data, one-dimensional normalization, and M4. As can be noted, there is a significant improvement in all error values, and the median tip error is reduced by almost 1.25 mm to 3.11 mm compared to M4 (more information on the significance test is provided in the appendix). The median value of RMSE is also reduced to 1.98 mm compared to the M4 method, which is 2.78 mm.

The designed Siamese network uses the RMSprop as the optimizer with a learning rate of 1^{-4}, a momentum of 0.9, and a decay factor of 0.7. The loss function's hyperparameters, including M, α and δ, are 0.5, 0.7, and 2.2, respectively. A typical case of predicted shapes using the designed Siamese network is shown in Figure 7. The error statistics based on the Euclidean distance between the true and the predicted shapes are shown in Figure 8. It can be noticed that the median of the Euclidean distance between the true and the predicted shapes is increasing towards the sensor's end. As explained in [18], this accumulative error might be due to inaccuracies in predicting the

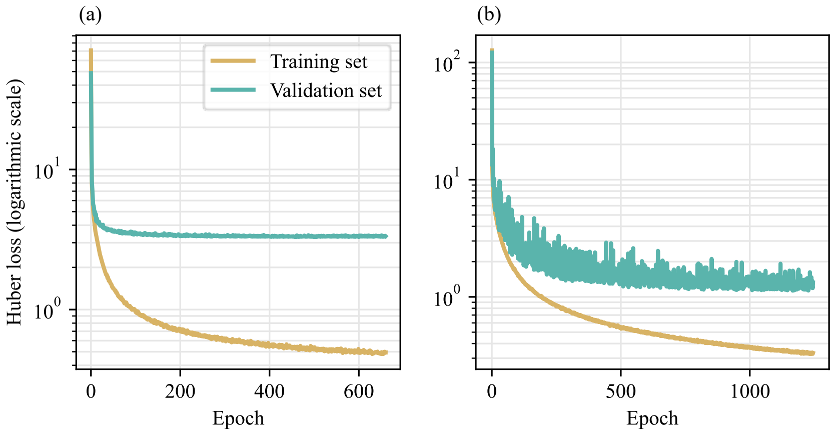

Figure 6: Training histories when the input data is preprocessed using (a) multi-dimensional and (b) one-dimensional normalization methods. The model was trained with early stopping conditions.

Table 2: Shape evaluation errors on the test dataset when the target data are processed using four different methods and when the network architecture is modified based on the Siamese design (indicated in bold). The model's output is first scaled back to absolute coordinates for each method, and then the error values are computed.

	tip error [mm]		**RMSE** [mm]	
method	median	IQR	median	IQR
M1	4.68	4.29	2.83	2.20
M2	6.73	5.46	3.97	2.69
M3	6.85	5.37	3.98	2.69
M4	4.36	4.46	2.78	2.56
Siamese	**3.11**	**3.38**	**1.98**	**1.97**

sensor's initial orientation.

4. Conclusion

In this work, we designed a deep learning-based model to extract the shape information of an edge-FBG sensor based on its full spectrum. We used the Hyperband algorithm to optimize the hyperparameters of our neural

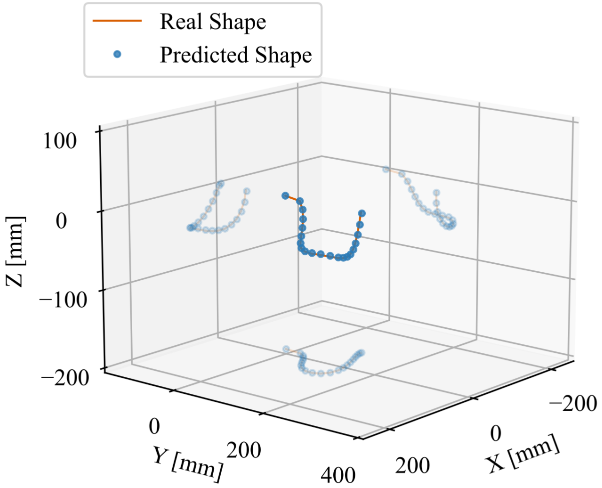

Figure 7: A typical case of predicted shapes using the designed Siamese model. The transparent lines and circles represent the XY, XZ, and YZ projections in the 3D graphs.

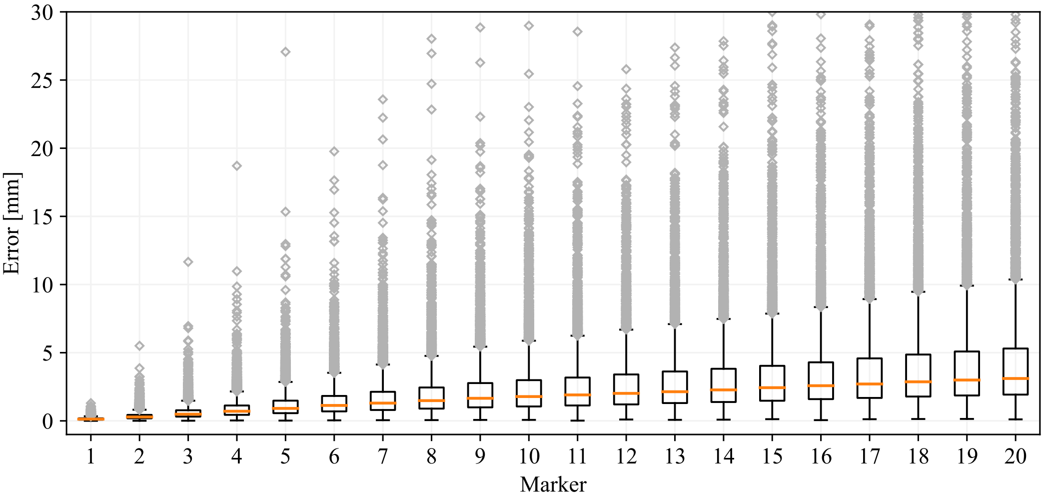

Figure 8: The error statistics are based on the Euclidean distance between the true markers' absolute coordinates and the predicted relative coordinates that are scaled back to the absolute values (the first marker is excluded). On each box, the median is indicated with a central mark, and the 25th and 75th percentiles are indicated with the bottom and top edges of the box, respectively. The whiskers show the minimum and maximum values within each group not considered outliers, and the outliers are marked with ◇ symbols. The total number of outliers are ∼ 400 out of ∼ 5300 samples. Some outliers were excluded for better visualization of the median values.

networks. We performed the hyperparameter tuning in two steps to avoid a large search space. First, the parameters related to the conv1D and the pooling layers were optimized. The best-performing architecture contains seven conv1D layers with a Sigmoid activation function and four max pooling layers. In the second step, optimization and loss calculation hyperparameters were defined in the Hyperband search space to optimize the networks with differently scaled input and output data. We showed that the models perform better when the input data are normalized with the one-dimensional z-scaling and when relative coordinates instead of absolute values are used as the target data. Upgrading the selected architecture to the Siamese design significantly improved the shape prediction accuracy of a 30 cm long sensor, with a median tip error of 3.11 mm and a median RMSE of 1.98 mm. We achieved an improvement of almost 2.7 mm in the median value of the tip error, and 1.4 mm in the median value of the RMSE using the proposed model compared to the previously designed network architecture proposed in

[18] which showed a median tip error of 5.8 mm and a median RMSE value of 3.4 mm. Compared to the mode field dislocation method [29, 28], our proposed model can accurately predict the sensor's shape with an order of magnitude lower tip error.

In future work, we will add temporal shape information to the input data to further improve the prediction accuracy. We also tend to continue investigating different architectural designs, including Siamese networks with triplet loss.

Supplementary information

In the supplementary material, we provided a video of the sensor's predicted shapes using the designed Siamese model.

Acknowledgement

We gratefully acknowledge the funding of this work by the Werner Siemens Foundation through the MIRACLE project.

References

[1] J. Burgner-Kahrs, D. C. Rucker, H. Choset, Continuum robots for medical applications: A survey, IEEE Transactions on Robotics 31 (6) (2015) 1261–1280.

[2] V. Vitiello, S.-L. Lee, T. P. Cundy, G.-Z. Yang, Emerging robotic platforms for minimally invasive surgery, IEEE reviews in biomedical engineering 6 (2012) 111–126.

[3] G. Dogangil, B. Davies, F. Rodriguez y Baena, A review of medical robotics for minimally invasive soft tissue surgery, Proceedings of the Institution of Mechanical Engineers, Part H: Journal of Engineering in Medicine 224 (5) (2010) 653–679.

[4] N. J. van de Berg, D. J. van Gerwen, J. Dankelman, J. J. van den Dobbelsteen, Design choices in needle steering—a review, IEEE/ASME Transactions on Mechatronics 20 (5) (2014) 2172–2183.

[5] X. Wang, M. Q.-H. Meng, Robotics for natural orifice transluminal endoscopic surgery: a review, Journal of Robotics 2012 (2012).

[6] B. P. M. Yeung, P. W. Y. Chiu, Application of robotics in gastrointestinal endoscopy: A review, World journal of gastroenterology 22 (5) (2016) 1811.

[7] C. J. Payne, G.-Z. Yang, Hand-held medical robots, Annals of biomedical engineering 42 (8) (2014) 1594–1605.

[8] N. Patel, C. Seneci, G.-Z. Yang, A. Darzi, J. Teare, Flexible platforms for natural orifice transluminal and endoluminal surgery, Endoscopy international open 2 (02) (2014) E117–E123.

[9] R. J. Webster III, B. A. Jones, Design and kinematic modeling of constant curvature continuum robots: A review, The International Journal of Robotics Research 29 (13) (2010) 1661–1683.

[10] K. Xu, N. Simaan, Analytic Formulation for Kinematics, Statics, and Shape Restoration of Multibackbone Continuum Robots Via Elliptic Integrals, Journal of Mechanisms and Robotics 2 (1), 011006 (11 2009). doi:10.1115/1.4000519.

[11] Optical Measurement/ Optical Tracking - NDI (2022).
URL `www.ndigital.com`

[12] Surgical Navigation/ Optical Tracking - Kick (2022).
URL `www.brainlab.com`

[13] M. Wagner, S. Schafer, C. Strother, C. Mistretta, 4d interventional device reconstruction from biplane fluoroscopy, Medical physics 43 (3) (2016) 1324–1334.

[14] N. Glossop, Localization and tracking technologies for medical robotics, in: Medical Robotics, Elsevier, 2012, pp. 41–58.

[15] T. Peters, K. Cleary, Image-guided interventions: technology and applications, Springer Science & Business Media, 2008.

[16] S. C. Ryu, P. E. Dupont, Fbg-based shape sensing tubes for continuum robots, in: 2014 IEEE International Conference on Robotics and Automation (ICRA), IEEE, 2014, pp. 3531–3537.

[17] S. Manavi, L. Witthauer, L. Iafolla, A. Zam, G. Rauter, P. C. Cattin, Temperature-compensated fbg-based 3d shape sensor using single-mode fibers, in: Integrated Photonics Research, Silicon and Nanophotonics, Optical Society of America, 2018, pp. JTu6C–1.

[18] S. Manavi, T. Renna, A. Horvath, S. Freund, A. Zam, G. Rauter, W. Schade, P. C. Cattin, Using supervised deep-learning to model edge-fbg shape sensors: a feasibility study, in: Optical Sensors 2021, Vol. 11772, SPIE, 2021, pp. 79–88.

[19] R. J. Roesthuis, S. Janssen, S. Misra, On using an array of fiber bragg grating sensors for closed-loop control of flexible minimally invasive surgical instruments, in: 2013 IEEE/Rsj International Conference on Intelligent Robots and Systems, IEEE, 2013, pp. 2545–2551.

[20] S. Jäckle, T. Eixmann, H. Schulz-Hildebrandt, G. Hüttmann, T. Pätz, Fiber optical shape sensing of flexible instruments for endovascular navigation, International journal of computer assisted radiology and surgery 14 (12) (2019) 2137–2145.

[21] G. Marowsky, Planar waveguides and other confined geometries: Theory, technology, production, and novel applications, Vol. 189, Springer, 2014.

[22] J. Yi, X. Zhu, H. Zhang, L. Shen, X. Qiao, Spatial shape reconstruction using orthogonal fiber bragg grating sensor array, Mechatronics 22 (6) (2012) 679–687.

[23] 3D Shape Sensing (2022).
URL `www.sensuron.com`

[24] Fiber Optic Shape Sensing — The Shape Sensing Company - TSSC (2022).
URL `https://shapesensing.com`

[25] C. Waltermann, A. L. Baumann, K. Bethmann, A. Doering, J. Koch, M. Angelmahr, W. Schade, Femtosecond laser processing of evanescence field coupled waveguides in single mode glass fibers for optical 3d shape sensing and navigation, in: Fiber Optic Sensors and Applications XII, Vol. 9480, SPIE, 2015, pp. 202–209.

[26] B. J. Soller, D. K. Gifford, M. S. Wolfe, M. E. Froggatt, High resolution optical frequency domain reflectometry for characterization of components and assemblies, Optics express 13 (2) (2005) 666–674.

[27] R. R. Thomson, H. T. Bookey, N. D. Psaila, A. Fender, S. Campbell, W. N. Macpherson, J. S. Barton, D. T. Reid, A. K. Kar, Ultrafast-laser inscription of a three dimensional fan-out device for multicore fiber coupling applications, Optics express 15 (18) (2007) 11691–11697.

[28] C. Waltermann, K. Bethmann, A. Doering, Y. Jiang, A. L. Baumann, M. Angelmahr, W. Schade, Multiple off-axis fiber bragg gratings for 3d shape sensing, Applied optics 57 (28) (2018) 8125–8133.

[29] S. Manavi, S. Freund, M. Angelmahr, G. Rauter, A. Zam, W. Schade, P. C. Cattin, The secret role of undesired physical effects in eccentric fbgs, arXiv preprint arxiv:2210.16316 (2022).

[30] L. Faustini, G. Martini, Bend loss in single-mode fibers, Journal of lightwave technology 15 (4) (1997) 671–679.

[31] P. Drexler, P. Fiala, Optical fiber birefringence effects–sources, utilization and methods of suppression, InTech, 2011.

[32] J. Bromley, I. Guyon, Y. LeCun, E. Säckinger, R. Shah, Signature verification using a" siamese" time delay neural network, Advances in neural information processing systems 6 (1993).

[33] K. Jamieson, A. Talwalkar, Non-stochastic best arm identification and hyperparameter optimization, in: Artificial intelligence and statistics, PMLR, 2016, pp. 240–248.

[34] L. Li, K. Jamieson, G. DeSalvo, A. Rostamizadeh, A. Talwalkar, Hyperband: A novel bandit-based approach to hyperparameter optimization, The Journal of Machine Learning Research 18 (1) (2017) 6765–6816.

[35] C. M. Bishop, et al., Neural networks for pattern recognition, Oxford university press, 1995.

[36] T. O'Malley, E. Bursztein, J. Long, F. Chollet, H. Jin, L. Invernizzi, et al., Kerastuner, `https://github.com/keras-team/keras-tuner` (2019).

[37] A. Kessy, A. Lewin, K. Strimmer, Optimal whitening and decorrelation, The American Statistician 72 (4) (2018) 309–314.

[38] T. Wiatowski, H. Bölcskei, A mathematical theory of deep convolutional neural networks for feature extraction, IEEE Transactions on Information Theory 64 (3) (2017) 1845–1866.

[39] S. Mallat, Group invariant scattering, Communications on Pure and Applied Mathematics 65 (10) (2012) 1331–1398.

[40] S. Chopra, R. Hadsell, Y. LeCun, Learning a similarity metric discriminatively, with application to face verification, in: 2005 IEEE Computer Society Conference on Computer Vision and Pattern Recognition (CVPR'05), Vol. 1, IEEE, 2005, pp. 539–546.

[41] G. Koch, R. Zemel, R. Salakhutdinov, et al., Siamese neural networks for one-shot image recognition, in: ICML deep learning workshop, Vol. 2, Lille, 2015, p. 0.

[42] S. Dey, A. Dutta, J. I. Toledo, S. K. Ghosh, J. Lladós, U. Pal, Signet: Convolutional siamese network for writer independent offline signature verification, arXiv preprint arXiv:1707.02131 (2017).

[43] P. J. Huber, Robust estimation of a location parameter, in: Breakthroughs in statistics, Springer, 1992, pp. 492–518.

[44] R. Hadsell, S. Chopra, Y. LeCun, Dimensionality reduction by learning an invariant mapping, in: 2006 IEEE Computer Society Conference on Computer Vision and Pattern Recognition (CVPR'06), Vol. 2, IEEE, 2006, pp. 1735–1742.

Appendix .1. Hyperparameter Optimization

This section presents the search criteria for all three hyperparameter optimizations performed in this work. Table 3 shows the search space settings for the first step of hyperparameter optimization, in which the number of conv1D layers was set to seven. Each conv1D layer was followed by a Sigmoid activation function and batch normalization. For the second step of hyperparameter optimization, the settings of the conv1D and the pooling layers were fixed. Table 4 shows the search space settings for this hyperparameter tuning. The search criteria for tuning the Siamese network's hyperparameters are presented in Table 5.

Table 3: Search criteria for the first step of hyperparameter optimization. The optimized kernel size, channel sizes, and pooling layer settings, resulting from this hyperparameter tuning step, are fixed in the next hyperparameter search step.

hyperparameter	**search space**
dropout rate	min: 0, max: 0.3, step: 0.1
optimizer	SGDW, Adamw
learning rate	0.1, 0.01, 0.001, 0.0001
weight decay	0.1, 0.01, 0.001, 0.0001, 0.00001
momentum	min: 0, max: 0.9, step: 0.1
kernel size (similar for all conv1D layers)	min: 2, max: 10, step: 1
channel size (different for each conv1D layer)	min: 8, max: 256, step: 8
choice of max pooling (different after each conv1D layer)	true, false
pooling size (different for each max pooling layer)	min: 2, max: 3, step: 1

Table 4: Search criteria for the second step of hyperparameter optimization. In this step, the hyperparameter search is performed three times for each data preprocessing approach.

hyperparameter	**search space**
dropout rate	min: 0, max: 0.3, step: 0.1
optimizer	SGDW, Adamw, RMSprop, Adadelta, Adamax
learning rate	0.1, 0.01, 0.001, 0.0001
weight decay	0.1, 0.01, 0.001, 0.0001, 0.00001
momentum	min: 0, max: 0.9, step: 0.1
loss function	mean absolute error, mean squared error, mean squared logarithmic error, huber loss, mean absolute percentage error, cosine similarity

Table 5: Hyperparameter search criteria for Siamese network. α, δ, and M are the loss function's hyperparameters, defined in Eq. 2.

hyperparameter	**search space**
α	min: 0, max: 1, step: 0.1
δ	min: 0.1, max: 5, step: 0.1
M	min: 0.5, max: 1, step: 0.1
rho	min: 0.5, max: 0.9, step: 0.1
momentum	min: 0.5, max: 0.9, step: 0.1

Appendix .2. Point Cloud Rescaling

This section explains the output data transformation approaches in more detail. Figure 9 shows a 3D shape example of the fiber sensor with 21 markers. For illustration purposes, we only focus on three highlighted markers (numbers 7, 12, and 17) and study their point cloud modifications as we apply M1-M4 rescaling methods. Figures 10 and 11 depict the scatter plots (point clouds) of measured coordinates of the selected markers in $\sim$ 5800 different shape examples. To compare the size of the point clouds after rescaling, an estimated sphere of each point cloud is depicted with a black mesh plot. Each sphere is centered at the mean coordinate of the original/rescaled points and has a radius of r. The radius r in each point cloud is the mean value of the calculated radial distance between the points and the cloud's center.

In method M1, the rescaling factor is the same for all spheres. Therefore, as can be seen in Figures 10 ($b_{1\text{-}3}$), the relative size between the spheres is similar to their original versions (Figures 10 ($a_{1\text{-}3}$)). In method M2, the rescaling factor for each point cloud is the average of calculated r values in

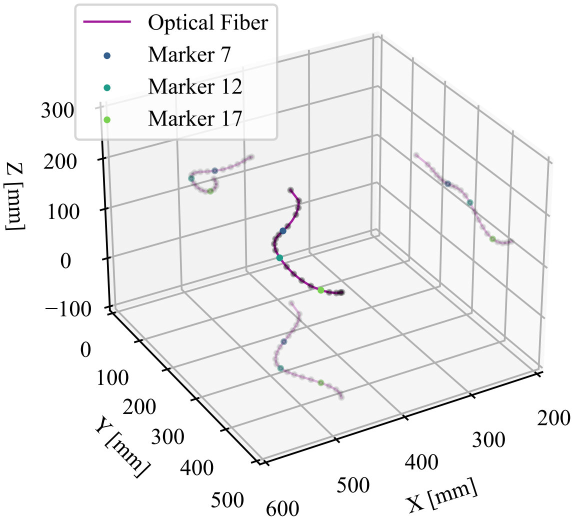

Figure 9: A 3D shape example of the fiber sensor with 21 attached reflective markers is depicted. The three highlighted markers, numbers 7, 12, and 17, are selected for scatter plotting. The remaining reflective markers are shown with gray circles.

that point cloud. Therefore, all point clouds have sphere mesh plots with a radius of one (Figures 10 ($c_{1\text{-}3}$)). In the third method (M3), applying three-dimensional standard scaling to the point clouds makes the transformed data uncorrelated (Figures 11 ($d_{1\text{-}3}$)). Using relative coordinates between the markers (M4) greatly changes the point clouds' appearance. As the markers are fixed on the sensor, the maximum relative distance between two neighboring markers is limited. It can be seen in Figures 11 ($e_{1\text{-}3}$) that the coordinate points, especially for the markers closer to the sensor's tip, are constrained in terms of volume and better form a sphere.

Appendix .3. Significance Test

In this section, the significance test results, comparing the evaluated models, are presented. Figure 12 shows the tip error box plots of all seven methods evaluated in this paper. As can be clearly noticed, the Siamese network has the least median tip error. We performed Tukey's HSD pairwise group comparisons on the seven methods. The Siamese method shows p-values close to zero compared to the other seven methods, proving that the shape prediction's improvement is statistically significant.

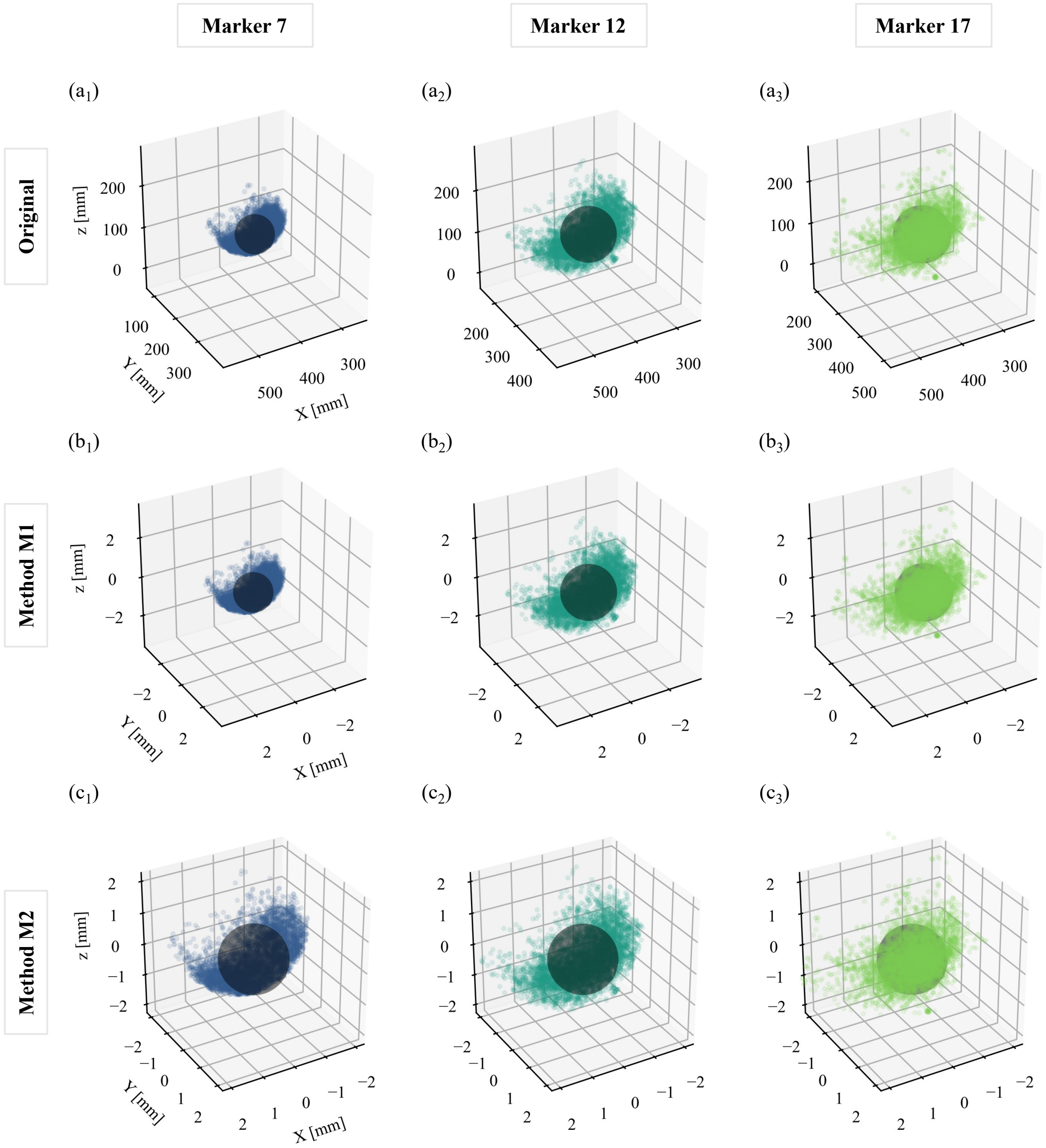

Figure 10: The scatter plot of measured coordinates in $\sim$ 5800 shape examples. The estimated sphere of each point cloud is shown with a black mesh plot. The Original coordinate values of marker numbers 7 (a_1), 12 (a_2), and 17 (a_3). The rescaled point clouds using M1 method for marker numbers 7 (b_1), 12 (b_2), and 17 (b_3). The rescaled point clouds using M2 method for marker numbers 7 (c_1), 12 (c_2), and 17 (c_3).

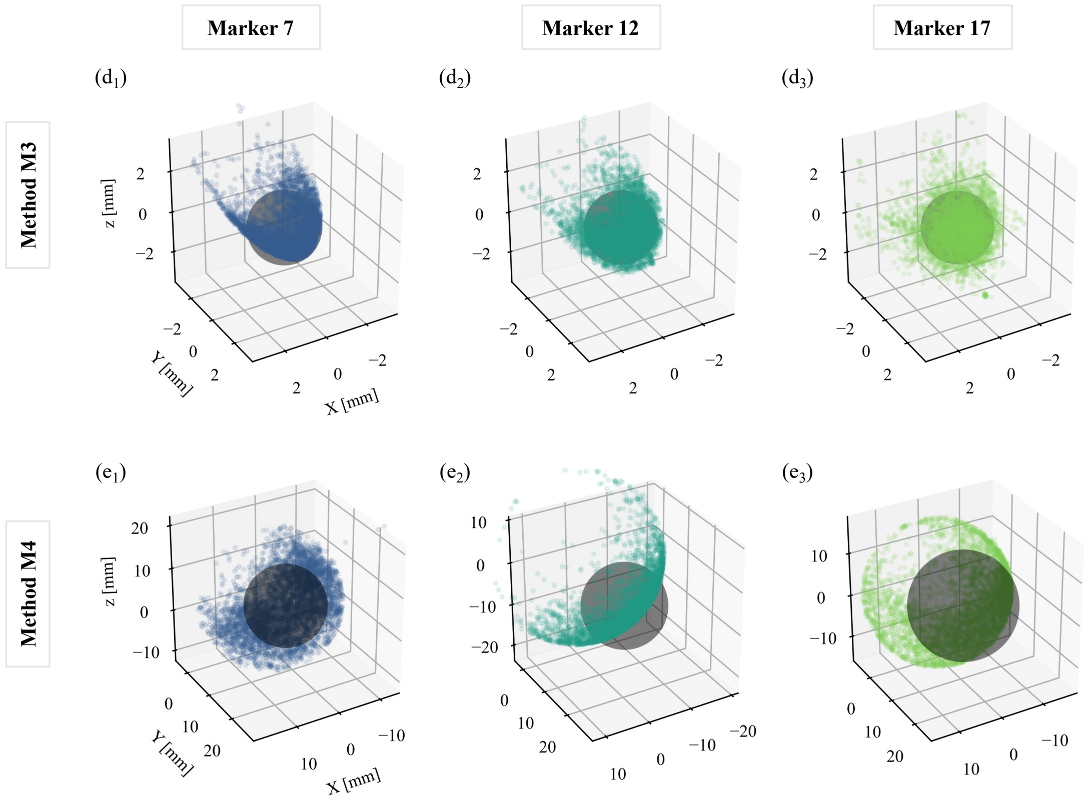

Figure 11: The rescaled point clouds using M3 method for marker numbers 7 (d_1), 12 (d_2), and 17 (d_3).The rescaled point clouds using M4 method for marker numbers 7 (e_1), 12 (e_2), and 17 (e_3).

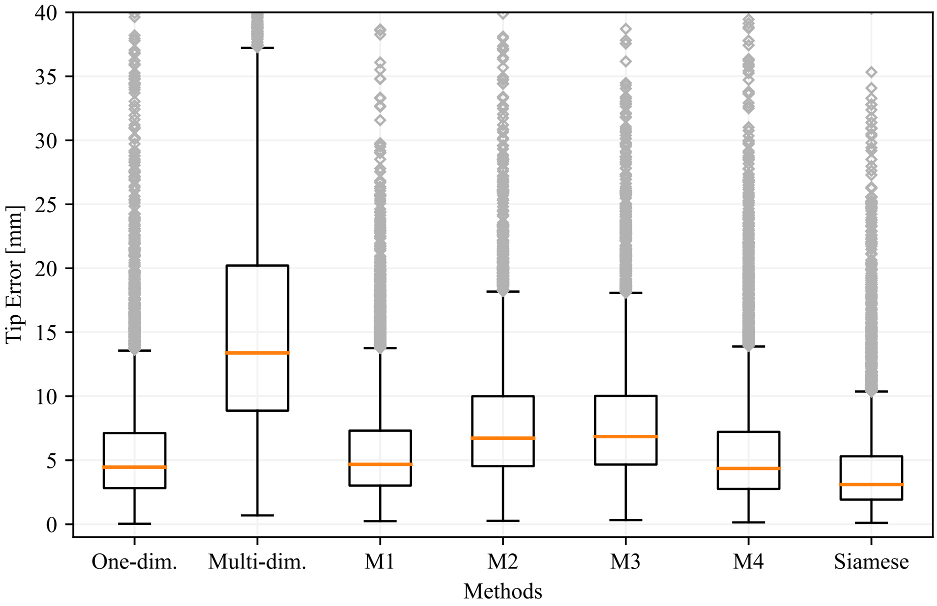

Figure 12: The tip error statistics of the designed networks when different data preprocessing methods and the Siamese architecture were employed. On each box, the median is indicated with a central mark, and the 25th and 75th percentiles are indicated with the bottom and top edges of the box, respectively. The whiskers show the minimum and maximum values within each group not considered outliers, and the outliers are marked with ◇ symbols. Some outliers were excluded for better visualization of the median values.

Chapter 7

The Secret Role of Undesired Physical Effects in Eccentric FBGs

In the publication presented in this chapter, we describe the physical phenomena in edge-FBG sensors that are induced by shape deformations. We comprehensively investigated how the edge-FBG spectra respond to external perturbations and why the mode field dislocation approach as the proposed technique for characterizing edge-FBG sensors in the literature is not accurate enough. The shape prediction error of our proposed deep learning method, compared to the mode field dislocation approach, is 50 times lower, and we could achieve a median tip error of almost $2\,\mathrm{mm}$ in a curvature range of $0.58\,\mathrm{m}^{-1}$ to $33.5\,\mathrm{m}^{-1}$. Moreover, by decoding our model's decisions, we were able to provide a visual explanation of our model's predictions. Our finding shows that the designed deep learning model has found a meaningful pattern in the edge-FBG's side slope and used them as additional sources of shape deformation information to compensate for the low spatial resolution of the sensor.

This is the submitted version of the following manuscript:
Samaneh Manavi Roodsari, Sara Freund, Martin Angelmahr, Georg Rauter, Wolfgang Schade, and Philippe C. Cattin. The secret role of undesired physical effects in accurate shape sensing with eccentric FBGs.
The preprint version is available online at https://doi.org/10.48550/arXiv.2210.16316.

The secret role of undesired physical effects in accurate shape sensing with FBGs

Samaneh Manavi Roodsari[1*], Sara Freund[1], Martin Angelmahr[2], Georg Rauter[1], Wolfgang Schade[2] and Philippe C. Cattin[1]

[1]Department of Biomedical Engineering, University of Basel,
Gewerbestrasse 14, Allschwil, 4123, Switzerland.
[2]Department of Fiber Optical Sensor Systems, Fraunhofer
Institute for Telecommunications, Heinrich Hertz Institute, HHI,
Am Stollen 19H, Goslar, 38640, Germany.

*Corresponding author(s). E-mail(s): samaneh.manavi@unibas.ch;

Abstract

Fiber optic shape sensing is an innovative technology that has enabled remarkable advances in various navigation and tracking applications. Although the state-of-the-art fiber optic shape sensing mechanisms can provide sub-millimeter spatial resolution for off-axis strain measurement and reconstruct the sensor's shape with high tip accuracy, their overall cost is very high. The major challenge in more cost-effective fiber sensor alternatives for providing accurate shape measurement is the limited sensing resolution in detecting the shape deformations. Here, we present a novel data-driven technique to overcome this limitation by removing strain measurement, curvature calculation, and shape reconstruction steps. We design a deep-learning model based on convolutional neural networks that is trained to directly predict the sensor's shape based on its spectrum. Our fiber sensor is based on easy-to-fabricate eccentric fiber Bragg gratings (FBG) and is interrogated with a simple and cost-effective readout unit in the spectral domain. We demonstrate that our deep-learning model benefits from undesired bending-induced effects (*e.g.,* cladding mode coupling and polarization), which contain high-resolution shape deformation information. These findings are the first steps toward a low-cost yet accurate fiber shape sensing solution for detecting complex multi-bend deformations.

Keywords: Eccentric FBGs, fiber sensors, FBG sensors, polarization, bending loss, deep learning, shape sensing, curvature sensing

Fiber optic shape sensing has proven to have great potential, specifically in medical applications such as catheter navigation, surgical needle tracking, and continuum robot navigation. Compared to other common navigation technologies [1–3], fiber shape sensing has many advantages, such as immunity to electromagnetic fields, bio-compatibility, and high flexibility. Fiber shape sensors are small in diameter, easily integrable into flexible instruments, and require no line-of-sight. Distributed sensors based on multicore fibers can also provide high-resolution shape measurements [4–6].

Fiber shape sensors measure off-axis strain, which is then used to calculate the directional curvature and reconstruct the sensor's shape [7]. Various fiber sensor configurations have been investigated for off-axis strain measurement, including multicore fibers with [8–10] or without [11–13] FBGs in their cores, fibers with cladding waveguide FBGs [14], and fiber bundles made from multiple single-mode fibers that contain FBG arrays [15–19]. For an accurate shape reconstruction, high spatial resolution for off-axis strain measurement is essential. In some fiber shape sensor configurations (*e.g.,* distributed multicore fiber sensor), sub-millimeter spatial resolution can be achieved [4]. However, in these sensors, complex and expensive readout units are used to analyze the output signal in time- or frequency domain for strain measurement [20–23]. Although fiber sensors interrogated with the spectral-domain readout systems are cheaper, their spatial resolution is limited by their lower sensing plane density [8, 24], making them inapplicable for tracking complex shape deformations. Therefore, a cost-effective, high-resolution, and accurate fiber shape sensing technique is desirable.

Among cost-effective fiber shape sensors interrogated in the spectral domain, eccentric FBG (eFBG) sensors show great capacity for tracking applications thanks to their unique sensing mechanism [25–27]. Each sensing plane in eFBG shape sensors consists of three highly localized FBGs, written off-axis in the fiber's core (also known as edge-FBG triplet) as shown in Fig. 1a [25]. Shape deformations are commonly calculated from the displacement of the fundamental mode-field inside the optical fiber, which is estimated from spectral intensity modifications (See Figs. 1b and c) [25, 26]. However, many other effects including bending-sensitive mode coupling [28–31], polarization-dependent losses [32–36], and wavelength-dependent bending losses [37–43] also modify the eFBGs spectral profile. These effects cannot be accurately modeled, and their impact on the sensor's spectra is indistinguishable from the mode-field displacements. Further details on the eFBG configuration, sensing mechanism, and bending-induced effects are provided in Methods.

We present in this paper a data-driven modeling technique based on deep learning (DL) that can indeed find a meaningful pattern in the eFBG signal that is affected by uncontrolled bending-induced effects. These additional

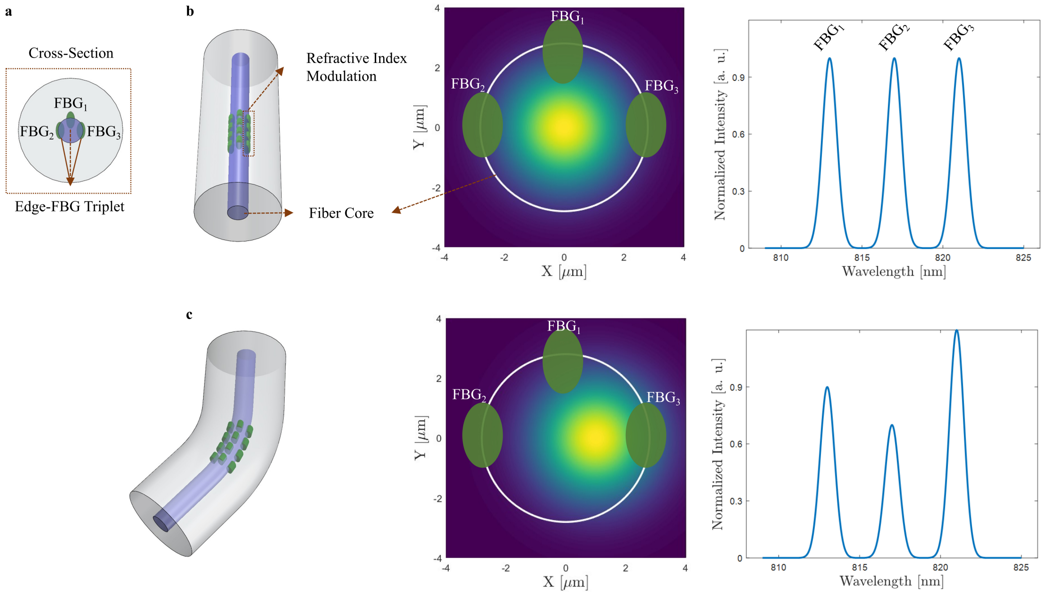

Fig. 1 **FBG configuration and working principle of the eFBG sensor.** **a** Sketch of the cross-section view of the eFGB sensor. Each sensing plane of the eFBG sensor consists of three FBGs inscribed off-axis with ∼90° angular separation (also known as edge-FBG triplet). **b** Mode-field distribution of a straight single-mode fiber and the expected signal from eFBGs of a same sensing plane. **c** When the fiber is curved, mode-field distribution moves in the opposite direction of the bending, which affects the relative intensity between the eFBGs.

sources of information considerably improve shape prediction accuracy. Our novel technique provides high spatial resolution shape estimation, directly from the eFBG sensor's signal without requiring any strain measurement, curvature calculation, and shape reconstruction steps.

Concept

In this section, we explain the designing and training process of a deep neural network for our eFBG shape sensor. The 30 cm long eFBG fiber sensor used in this work features five sensing planes separated by 5 cm from each other. At each sensing plane, three off-axis FBGs are inscribed at a radial distance of ∼2 µm to the top, left, and right side of the fiber's core.

The dataset used for developing the deep-learning-based model is collected using a similar setup reported in our previous work [44] (see Methods for more details). We use three normalized, consecutively measured spectral scans as input data to the proposed DL model. Each scan is recorded from 800 nm to 890 nm comprising 190 wavelength components. The target data are the relative coordinates of 20 discrete points (reflective markers of the tracking system) measured over the length of the shape sensor (see Ref. [45] for more detail on data preprocessing). For this dataset, around 58000 samples are collected during 30 mintues of random movement of the fiber sensor. To evaluate the predictive performance of the trained model in an unbiased way, samples are first shuffled and then split into Train-Validation-Test subsets: 80% for training, 10% for validating, and 10% for testing. We refer to this testing data set as $Test_1$ for the remainder of this paper. The second set of data ($Test_2$) with a size of $\sim$5800 samples is recorded separately to evaluate the performance of the trained model for unseen shapes from a continuous movement. We also collected 320 samples, as $Test_3$, when only certain sensor regions are bent (see Methods for more detail).

A DL model needs a specially designed network architecture to extract essential features from the sensor's spectra and to predict its corresponding shape. To do so, we ran an optimization algorithm similar to the Hyperband optimizer [46]. This optimization algorithm looks for the best set of essential parameters, such as number of layers, whose values can not be estimated from the data during training (also known as hyperparameters). Figure 2 shows the architecture of the best-performing configuration after hyperparameter tuning.

To find out which part of the spectra is relevant for feature extraction, we calculate the forward finite difference of the network's output with respect to the input spectral components. This difference provides an influence evaluation

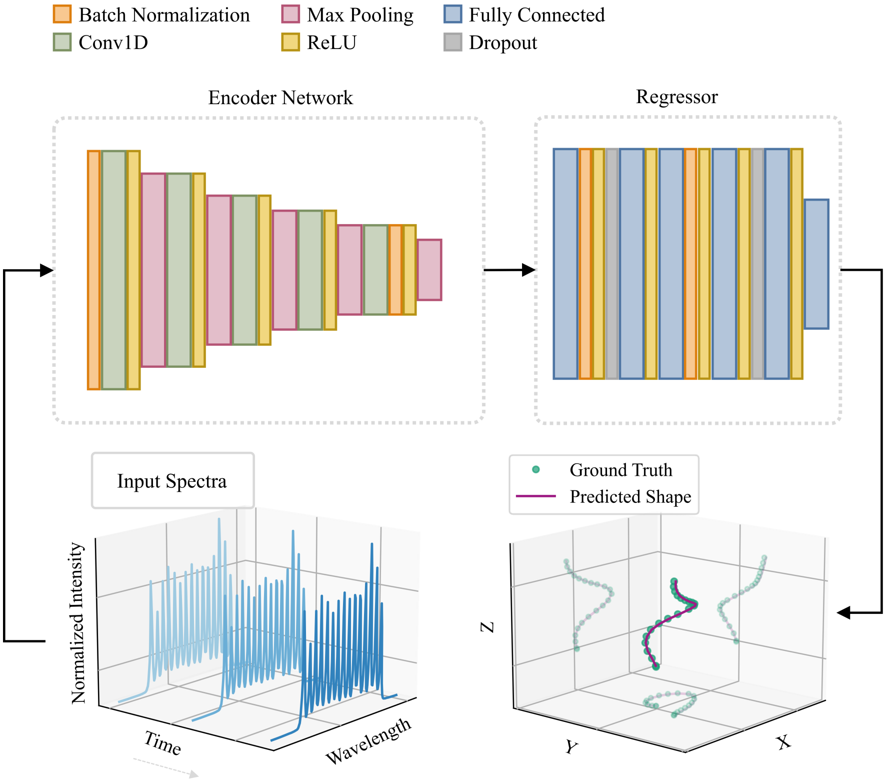

Fig. 2 Architecture of the best-performing configuration after hyperparameter tuning. The architecture includes five 1D convolutional layers (Conv1D), six fully connected layers, five max pooling layers, four batch normalization steps, and two dropout steps. The designed network receives three consecutive spectral scans as the input and predicts the relative coordinates of 20 discrete points over the sensor's curve. More detail on the channel, kernel, and pooling sizes is available under Methods.

Table 1 Shape evaluation errors in MFD and DL methods using test sets $Test_1$, $Test_2$, and $Test_3$. The lowest achieved error values are indicated in bold.

		tip error [mm]		**RMSE** [mm]	
dataset	method	median	IQR	median	IQR
$Test_1$	MFD	111.3	121.5	59.4	71.7
	DL	**2.1**	**2.6**	**1.5**	**1.6**
$Test_2$	MFD	98.5	46.0	53.8	29.1
	DL	17.1	12.6	9.8	7.0
$Test_3$	MFD	39.5	34.7	17.1	18.3
	DL	6.0	9.0	5.1	6.6

for each wavelength component of the input spectra to decode the model's predictions (see Methods).

As an evaluation baseline, we compared the shape prediction accuracy of the proposed DL approach with the mode-field dislocation method (MFD) on the same test sets. Following the process explained in our previous work [25], we calibrate our shape sensor to determine the exact angular and radial position of each eFBG. Then, we estimate the mode-field centroid at each sensing plane and calculate the curvature and the bending direction [25]. Finally, we reconstruct the 3D shape of the eFBG sensor using the interpolated values of the calculated directional curvatures at small arc elements. It should be noted that the density of the sensing planes in our eFBG shape sensor is not sufficient for the MFD method to estimate complex deformations. Nevertheless, we performed the test to show the superiority of the proposed data-driven technique (DL).

Results and Discussion

Shape prediction evaluation. We evaluated the performance of the DL approach using the three testing datasets and compared the results with the MFD method. Table 1 shows the shape error metrics including the tip error, that is, the Euclidean distance between the true and the predicted coordinate of the sensor's tip, and the root-mean-square of the Euclidean distance (RMSE) between the true and the predicted coordinates of the discrete points along the sensor's length. The MFD approach, when using $Test_1$ dataset, shows median and interquartile (IQR) tip error values of 111.3 mm and 121.5 mm, respectively. These error values reduce to 98.5 mm and 46 mm when using $Test_2$ dataset. The reason for such performance difference is that $Test_1$ dataset contains more diverse shapes, as the samples are randomly selected from a larger dataset compared to $Test_2$, which is a continuous sensor movement in a short period. As expected, the error values are considerably high in all testing datasets, since there is too little information available for the MFD approach to estimate the complex shape deformations in these datasets.

The DL method, on the other hand, significantly improves the shape prediction accuracy of $Test_1$ samples, with a median and IQR tip error values of 2.1 mm and 2.6 mm. These values increase to 17.1 mm and 12.6 mm on less diverse $Test_2$ samples. This is due to the fact that a DL model can only learn to extract the most general/relevant features from the input signal, if the training dataset is representative of the expected signals from the sensor. However, in $Test_2$ dataset, less than 2% of the samples have at least 100 similar examples in the training data (a maximum RMSE of 5 mm is chosen as the similarity measure after evaluating several thresholds). This shows that 30 minutes of manual shape manipulation is insufficient to cover the sensor's working space and create a representative training dataset for the model to generalize properly. On the other hand, in $Test_1$ dataset, almost 20% of the samples have at least 100 similar examples in the training dataset, which means the DL method is being tested on samples that the model has already learned how to handle. Therefore, $Test_1$ can mimic the situation where the training dataset represents the expected shapes of the sensor.

Shape evaluation results of $Test_1$ dataset define the performance of our model's lower limit. Such performance difference also suggests that the DL model is better to be trained as application-specific, since it can better focus on relevant features when learned from the expected shape distribution of the sensor. On the other hand, when training data covers most of the expected behaviors from the sensor, the DL model might only "memorize" the corresponding shape for each signal without searching for relevant features in the sensor's spectrum. To investigate this, we compare the performance of our DL method with a dictionary-based algorithm. In this approach, all the training and validation samples create a pre-defined dictionary. The shape prediction is made by looking for the closest spectrum to the test sample and presenting its corresponding shape. The median tip errors on datasets $Test_1$ and $Test_2$ are 5.9 mm and 50.0 mm with IQR values of 3.9 mm and 43.3 mm, respectively, which are higher than error values when using our DL technique. This shows that our DL model generalizes and is indeed beneficial for predicting more accurate shapes.

Two essential factors have to be considered when working with dictionaries: the size of the dictionary and the execution time required to find the best matching example. To get an accurate shape estimation for a given sample, the number of stored samples in the dictionary should be large enough to cover all possible examples, which leads to a long execution time. Therefore, this approach has a trade-off between accuracy and execution time. However, extensive training data do not negatively affect these two factors in DL method, as the resulting model size is independent of the training data size.

Our observations show that the designed DL model can recognize deformations even between the sensing planes. To further investigate this interesting finding, we evaluated the shape predictions using $Test_3$ dataset, in which the deformations are only applied between the sensing planes. $Test_3$ dataset contains four deformation examples, each repeated twice and measured 40 times. As expected, the classical MFD method is not able to accurately predict the sensor's shape for such deformations, as the deformed area is not at any of the sensing planes. However, when using the DL method, we achieve a median tip error of 6 mm which is $\sim$ six times smaller than the median tip error using

MFD on this dataset. The precision of the predicted tip position in $Test_3$ dataset is 1.9 mm on average.

An example from $Test_3$ samples where the sensor is bent in the region between the sensing planes 3 and 4 is depicted in Fig. 3a. It should be noted that the intensity ratio of the eFBG Bragg peaks in each sensing plane can also be influenced by previously mentioned effects other than fundamental mode-field dislocations. The MFD approach, however, does not consider such effects

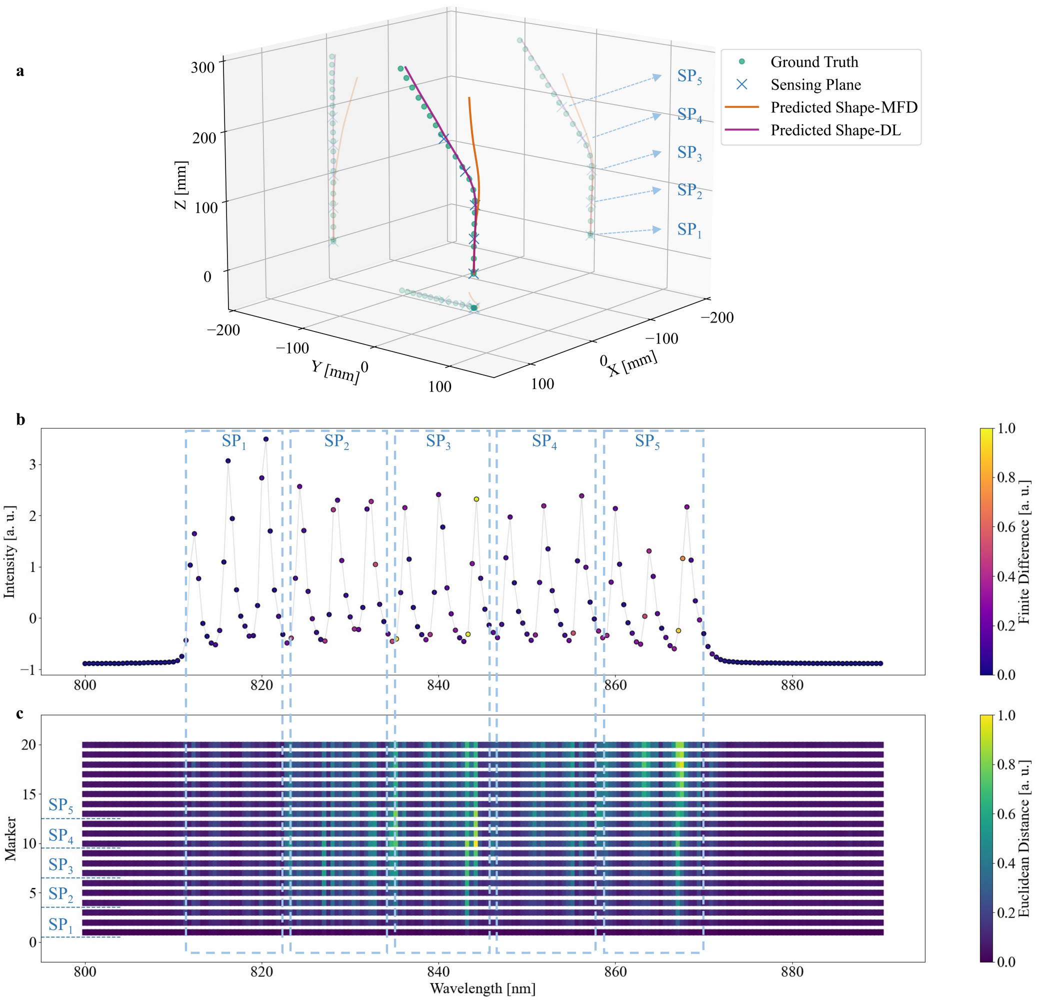

Fig. 3 Decoding the DL model decision for deformations between sensing planes. a An example from $Test_3$ samples in which the sensor is bent in the region between the sensing planes 3 and 4. The true shape (ground truth) is shown with green circles. The five sensing planes of the sensor are shown with × signs. The predicted shapes using the mode-field dislocation method (MFD) and the deep learning method (DL) are shown with orange and purple solid lines, respectively. **b** The finite difference of the loss value with respect to the input spectral elements. Wavelength components shown with colors closer to yellow contribute more to the model's decision on this particular example. **c** Highlighting the importance of input spectral elements in relative coordinate prediction of all 20 markers based on the magnitude of the Euclidean distance between the predicted relative coordinates of each marker, before and after spectral modification. The position of the sensing planes with respect to the markers are indicated with dashed blue lines. SP_i: i_{th} Sensing Plane.

and is thus incapable of correctly interpreting the signal variations. On the other hand, the DL model manages to accurately predict the sensor's shape as it looks at the full spectral profile, including the minute changes at the wavelengths outside the Bragg resonances. Figure 3b shows the finite difference analysis of the loss value with respect to the 190 wavelength components of the input spectra. The higher the difference, the more important the corresponding wavelength component is for shape prediction in this example. Figure 3c gives a deeper insight into this investigation. For all 190 wavelength components, the Euclidean distance between the predicted relative coordinates of each marker before and after the spectral modification is depicted using a color map. The contribution of each wavelength component to the relative coordinate prediction of all 20 markers is realized from the presented color map in Fig. 3c.

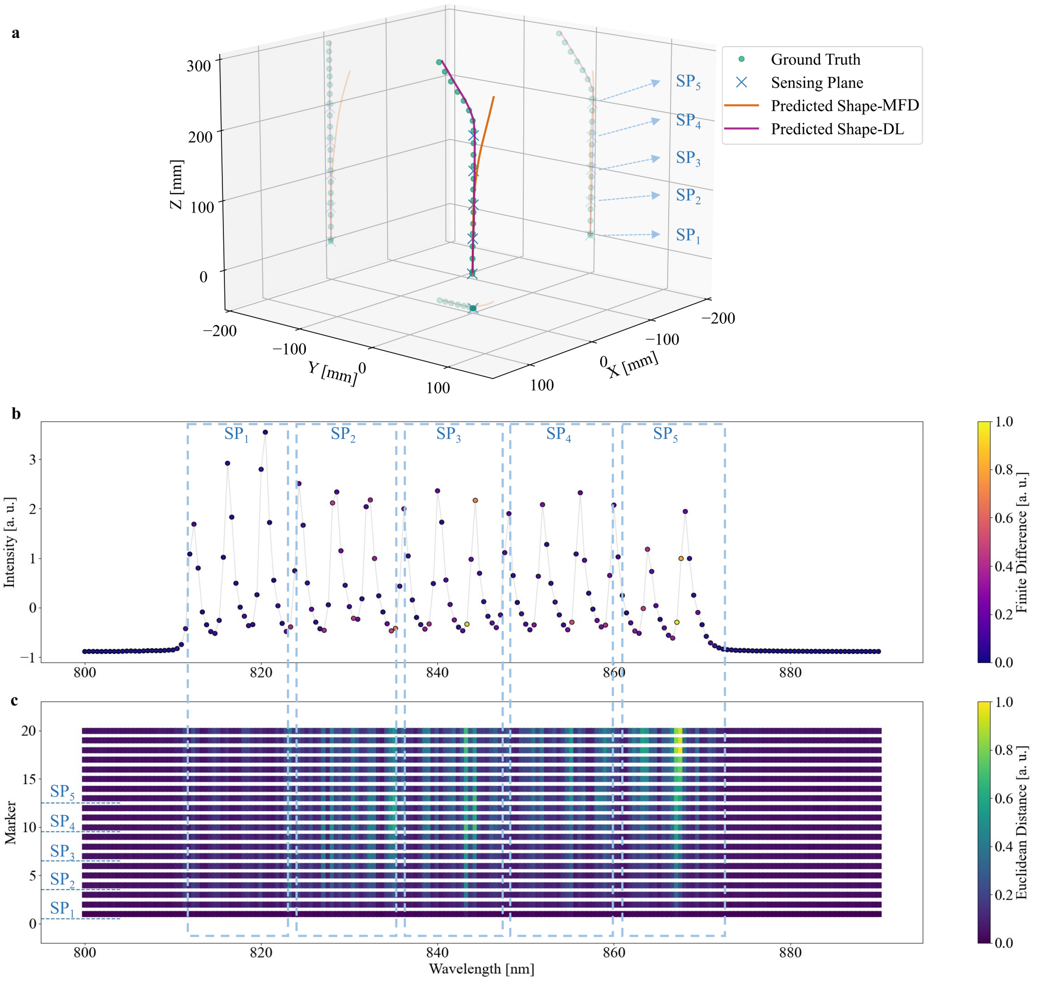

Fig. 4 Decoding the DL model decision for deformations after the last sensing plane. An example from $Test_3$ samples in which a 3 cm long segment, 1 cm after the last sensing plane, is deformed. Refer to the caption of Fig. 3 for more details.

Another important finding is that the DL model can also detect deformations after the last sensing plane. Figure 4 shows an example in which, a 3 cm long segment, 1 cm after the last sensing plane, is deformed. Similar to the example in Fig. 3, the MFD method is not able to predict the sensor's shape in such deformations. The DL model, in contrast, learned to employ relevant features in the side slopes of the eFBG spectra to predict the correct shape (see Figs. 4b and c). A possible explanation for such intriguing performance is that in the area after the last sensing plane, wavelength-dependent interference occurs between the back-reflected light from the air-glass interface at the fiber's end tip (Fresnel reflection) and the downstream incident light. Deformations in this region affect interferences in two ways: first, the spectral profile of the downstream light changes due to the bending. Second, the coupling conditions between the back-reflected and the downstream lights change. Consequently, the measured spectra from the fiber sensor show small variations, as the deformations affect the interference pattern.

Optimum number of sensing planes. A key factor in eFBG sensors, when using the MFD method, is the number of sensing planes for detecting shape deformations. Similar to any other quasi-distributed shape sensor, the distance between the sensing planes determines the sensor's spatial resolution in shape measurements. Depending on the complexity of the shape deformations, a limited number of sensing planes in the sensor (low spatial resolution) can lead to large tip errors in methods that include shape reconstruction (*e.g.,* the MFD method). In this section, we present a theoretical analysis for realizing the minimum number of sensing planes required in eFBG sensors when using the MFD method to reach the same accuracy for the shape prediction as we get using five sensing planes in our DL method here.

We simulated the shape reconstruction error for different spatial resolutions. To do so, we first interpolate the discrete curve points over the sensor's true shape measured by the motion capture system, using a Spline with a resolution of 0.1 mm (this value was selected empirically). We then calculated the curvature and the torsion–the curve's deviation from the osculating plane–at the query points. Finally, we use the calculated curvatures and bending directions at the sensing planes to reconstruct the spatial curve and compare it with the true shape. For a 25 cm long sensor with 50 mm spatial resolution (five sensing planes), the median tip error of the reconstructed shapes, tested on $Test_1$ and $Test_2$ datasets, is $\sim$50 mm, which is almost 16 times higher compared to what the DL approach achieved (see Table 1). In order to get a median tip error of 3 mm, the spatial resolution of the sensor should also be in a similar range, meaning that the MFD method would need around 84 sensing planes consisting of 252 eFBGs.

Conclusion

In this paper, we developed a novel fiber shape sensing mechanism with a data-driven technique, that unlike conventional fiber shape sensors, does not include off-axis strain measurement and curvature calculation at discrete points along the fiber sensor's length to estimate its 3D shape. We used an easy-to-fabricate eFBG sensor with a simple and cost-effective readout unit. We designed a deep learning algorithm that can directly learn from our sensor's signal to predict its corresponding shape. We then evaluated the shape prediction accuracy of our designed model (the DL method) in various testing conditions and compared it with an exemplary experiment, the mode-field dislocation method (MFD). Furthermore, we showed that the spatial resolution of off-axis strain measurement in FBG-based (quasi-distributed) shape sensors is the main limitation, as the deformations between the sensing planes are not detected in complex shapes. The deep learning technique, on the other hand, uses the full spectrum of our eFBG sensor, including the Bragg resonance's side slopes, as the model's input to compensate for the low density of sensing planes. We believe that the deep learning model is using the impact of undesired bending-induced phenomena, including cladding mode coupling, bending-loss oscillations, and polarization-dependent losses, as additional sources of information to overcome the spatial resolution limitation for detecting complex deformations. Therefore, there is no need to adapt the fiber sensor design and its interrogation system for minimizing the impact of such bending-induced phenomena. The shape prediction error of our developed DL method for 3D curves in a curvature range of $0.58\,\mathrm{m}^{-1}$ to $33.5\,\mathrm{m}^{-1}$ is reduced by a factor of ~ 50 compared to the MFD method. We also showed that the designed deep learning model generalizes nicely, as the performance is twice as good compared to a dictionary-based algorithm. The proposed shape sensing solution is 30 times less expensive than the commercially available distributed fiber shape sensor with a similar level of accuracy.

Methods

Working Principle of eFBG Sensor When the eFBG sensor is bent, the field distribution of the fundamental mode moves away from the core center [25–27] (see Fig. 1b). Dislocations in the mode-field's centroid cause intensity changes in the reflected signal from the eFBGs [25]. From the intensity ratio between the eFBGs at each sensing plane, curvature and bending direction can be calculated [25]. For simplification, this approach assumes that no other physical phenomena inside a bent optical fiber affect the intensity ratio between the eFBGs of the same sensing plane.

However, positioning FBGs away from the core axis breaks the cylindrical symmetry of the fiber, which increases coupling from the core mode to the cladding modes [28, 29]. The strength of such mode coupling varies when the fiber is bent, as it affects the overlap integral between the interacting modes [28, 30]. Bending an optical fiber causes strain-induced refractive index changes and dislocates the intensity distribution of the propagating light [26, 47, 47], which directly influences the coupling efficiency. Therefore, the intensity of the cladding modes changes when the fiber is bent. In eFBGs, formation of cladding-mode resonances in fiber gratings provides highly sensitive full directional bending response with a simple light intensity measurement [31]. Although cladding modes are often stronger in stripped fibers or in fibers with lower refractive index coatings than the cladding layer [28, 29], they have also been observed in standard fibers coated with higher refractive index materials [48]. Any recoupling between the excited cladding resonances and the fundamental mode, affects the relative intensity values between the eFBGs.

FBG interrogators for quasi-distributed sensors typically consist of a broadband light source, like a super luminescent diode (SLED), and a grating-based spectrometer. The emitted light from SLEDs is partially polarized, meaning that it undergoes wavelength-dependent polarization changes [32] in a birefringence medium (*e.g.,* bent fiber) [33–36]. On the other hand, the efficiency of spectrometer grating is polarization-dependent, and therefore, the spectral profile will be impacted by polarization-dependent losses. This effect further modifies the measured intensity ratio between the Bragg peaks. The polarization effect in intensity-based fiber sensors is often kept at a minimum by using a polarization scrambler to change the polarization state randomly or by using polarization-insensitive spectroscopy instruments.

As is well known, light power loss increases when optical fibers bend [37]. Macro bending loss usually reflects itself in spectral modulations due to coherent coupling between the core mode and the radiated field reflected by the cladding-coating and the coating-air interfaces (also known as whispering gallery modes) [38, 49]. The reflected field, at the coating-air boundary, causes short-period modulations as the re-injection path is longer [38, 49]. Whereas, reflections at the closer cladding-coating interface cause long-period resonances [39–41, 49]. These bending attenuation losses are also temperature-dependent. Thermal variations affect the refractive index of the coating layer and consequently influence the coupling between the core and the cladding whispering gallery modes [42]. Many models have been proposed to evaluate bending loss peak positions and shapes ([39, 40, 43]). The strong wavelength dependence of bending losses is an additional complicating factor in designing intensity-based sensors [49] as it modulates the spectral profile and affects the intensity ratio at the Bragg peaks of the eFBGs in a same sensing plane.

Setup. Data acquisition setup used for developing the deep-learning-based model is shown in Fig. 5. We used a low-cost FBG interrogator (MIOPAS GmbH, Goslar, Germany) consisting of an uncooled transmit optical subassembly (TOSA) SLED module and a NIR micro-spectrometer with 0.5 nm resolution to cover all 15 Bragg wavelengths from 813 nm to 869 nm. We recorded the sensor's spectra at random curvatures and orientations (in a curvature range of $0.58\,\mathrm{m}^{-1}$ to $33.5\,\mathrm{m}^{-1}$) while monitoring the reflective markers attached to the 30 cm long sensor using a motion capture system (Oqus 7+, Qualisys AB, Sweden). The data acquisition time period was 30 minutes for $Test_1$ and 3 minutes for $Test_2$ datasets. The acquisition rates in the FBG interrogator and the motion capture system were 75 Hz and 200 Hz, respectively. The sensor's spectra and the coordinate values corresponding to its shape were synchronized with a tolerance of less than 3 ms.

We also used a laser-cut curvature template (Fig. 5) to collect 320 samples for $Test_3$ dataset, when only certain sensor regions should be bent. The curvature template has four grooves allowing the sensor to be bent at the middle 30 mm area between the sensing planes 2 and 3, 3 and 4, 4 and 5, and 10 mm after the last sensing plane with a bending radius of 50 mm.

Training Setup. The search space we defined for tuning the network's hyperparameters consists of the number of 1D convolutional layers (Conv1D), the number of fully connected layers (FC), the layer settings, the choice of batch normalization and downsampling, training settings, and loss function parameters. Search criteria are presented in Table 2.

In the designed network, input samples with a batch size of 256 are first batch normalized and then fed into a Conv1D layer with 16 channels, followed by a max pooling layer with a kernel size of 3 and a stride of 2. The second Conv1D layer also has 16 channels, followed by a max pooling layer with a kernel size of 2. The third Conv1D layer has 32 channels, followed by a max pooling layer with a kernel size of 3 and a stride of 2. The fourth Conv1D layer also has 32 channels with a stride of 2, followed by a max pooling layer with a kernel size of 3. The last Conv1D layer has 256 channels, followed by batch normalization and a max pooling layer with a kernel size of 2 and a

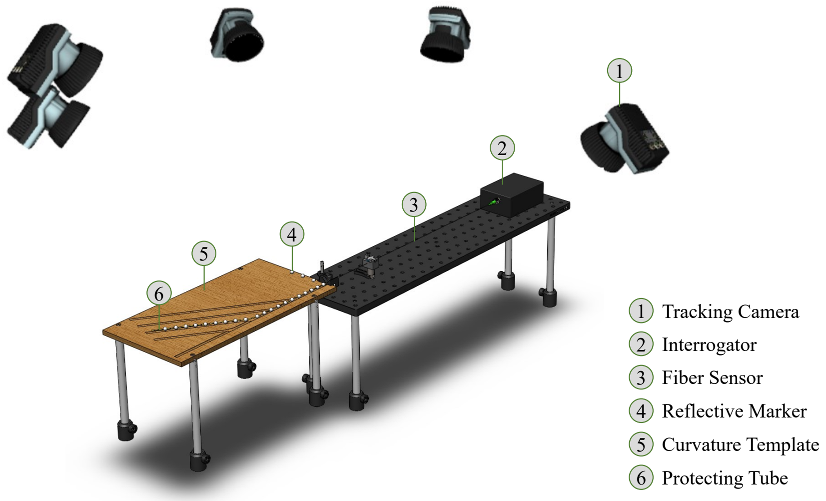

Fig. 5 The data acquisition experimental setup. The motion capture system includes five tracking cameras (Oqus 7+, Qualisys AB, Sweden). For protection purposes, the fiber sensor is inserted in a Hytrel furcation tubing with an inner diameter of 425 µm and an outer diameter of 900 µm. Two v-clamps are used to hold the protection tubing and to fix the optical fiber before the insertion. The reflective markers are 6.4 mm in diameter with an 1 mm opening (X12Co., Ltd, Bulgaria). A thermocouple is placed close to the sensor's base to monitor the temperature during the data acquisition, ensuring no sudden thermal fluctuation affects the sensor's signal.

Table 2 Search criteria for hyperparameter optimization.

hyperparameter	search space	selected values
number of Conv1D layer	min: 1, max: 20, step: 1	5
number of FC layer	min: 1, max: 20, step: 1	5
BN after each layer	true, false	-
dropout after FC layer	true, false	-
dropout rate	min: 0.1, max: 0.8	-
stride	min: 1, max: 2, step: 1	-
kernel size (max pooling layer)	min: 2, max: 3, step: 1	-
distribution of initial weights	standard, Xavier_uniform, Xavier_normal, Kaiming_uniform, Kaiming_normal	Xavier_normal
learning rate	0.01, 0.001, 0.0001, 0.00001	0.0001
sorting Conv1D layers	true, false	true
L2 regularization	0.1, 0.01, 0.001, 0.0001, 0.00001, 0	0
threshold in SmoothL1	any values between 0.0 and 5.0	4.04

stride of 2. The extracted features are flattened to a 2048-long vector, fed into 5 FC layers, each with 2000 units. The first FC layer is followed by batch normalization and a dropout layer with a probability of 0.37, and two more FC layers. A batch normalization, an FC layer, a dropout layer with a probability of 0.16, and a fourth FC layer are the remaining layers before the final layer. The last layer is an FC layer that maps the output of the fourth FC layer into the target values, the relative coordinates. In all layers of this network architecture, the rectified linear unit (ReLU) serves as the activation function, and the kernel size for the Conv1D layers is 3. In this model, the Adam optimizer with a learning rate of 0.0001 minimizes the SmoothL1 loss function with a threshold of 4.04.

Decoding The Model's Decisions. Inspired by Gradient-weighted Class Activation Mapping (Grad-CAM), we decode the decisions made by our CNN (convolutional neural network)-based model. Decoding our model's decisions helps us understand which part of the input spectra contributes to coordinate predictions. Grad-CAM is a commonly used technique in image classification problems that generates visual explanations from any CNN-based model without any re-training or architectural changes required. Gradient is a measure that shows the effect on the output caused by the input. In other words, we are looking for the part of the input with the highest effect on the model's output. However, due to the small output dimension in each channel of the last Conv1D layer, its gradient heat map highlights the inputs' important parts with a low resolution. Therefore, instead of the gradient of the Conv1D layers, we calculate the forward finite difference of the model's loss with respect to the input spectral elements. The spacing constant is chosen 0.1, higher than the spectral intensity noise level. In this method, we modify the intensity value of one spectral element and monitor the changes of the model's loss value. We repeat this process for all 190 spectral elements. The resultant color maps (shown in Fig. 3 (b) and Fig. 4 (b)) indicate the impact of the changes in each spectral element on the model's SmoothL1 loss value. In order to investigate the contribution of each spectral element to the coordinate prediction of each individual marker, we calculated the Euclidean distance between the predicted coordinates of each marker before and after spectral modification. This way, we were able to highlight all the spectral elements contributing to the relative coordinate prediction of each marker.

Supplementary Information. We provided three videos in the supplementary material, visualizing the sensor's predicted shapes using the DL and the MFD methods on all three datasets.

Acknowledgments. We gratefully acknowledge the funding of this work by the Werner Siemens Foundation through the MIRACLE project.

References

[1] Optical Measurement/ Optical Tracking - NDI. www.ndigital.com Accessed 2022-01-25

[2] Surgical Navigation/ Optical Tracking - Kick. www.brainlab.com Accessed 2022-07-12

[3] Wagner, M., Schafer, S., Strother, C., Mistretta, C.: 4d interventional device reconstruction from biplane fluoroscopy. Medical physics **43**(3), 1324–1334 (2016)

[4] Soller, B., Wolfe, M., Froggatt, M.: Polarization resolved measurement of rayleigh backscatter in fiber-optic components. In: National Fiber Optic Engineers Conference, p. 3 (2005). Optica Publishing Group

[5] TSSC - The shape sensing company / Fiber optic shape sensing. www.shapesing.com Accessed 2022-12-01

[6] Meng, Y., Fu, C., Du, C., Chen, L., Zhong, H., Li, P., Xu, B., Du, B., He, J., Wang, Y.: Shape sensing using two outer cores of multicore fiber and optical frequency domain reflectometer. Journal of Lightwave Technology **39**(20), 6624–6630 (2021)

[7] Marowsky, G.: Planar Waveguides and Other Confined Geometries: Theory, Technology, Production, and Novel Applications vol. 189. Springer, New York (2014)

[8] Khan, F., Denasi, A., Barrera, D., Madrigal, J., Sales, S., Misra, S.: Multicore optical fibers with bragg gratings as shape sensor for flexible medical instruments. IEEE sensors journal **19**(14), 5878–5884 (2019)

[9] Moore, J.P., Rogge, M.D.: Shape sensing using multi-core fiber optic cable and parametric curve solutions. Optics express **20**(3), 2967–2973 (2012)

[10] Bronnikov, K., Wolf, A., Yakushin, S., Dostovalov, A., Egorova, O., Zhuravlev, S., Semjonov, S., Wabnitz, S., Babin, S.: Durable shape sensor based on fbg array inscribed in polyimide-coated multicore optical fiber. Optics Express **27**(26), 38421–38434 (2019)

[11] Nishio, M., Mizutani, T., Takeda, N.: Shape identification of variously-deformed composite laminates using brillouin type distributed strain sensing system with embedded optical fibers. In: Sensors and Smart Structures Technologies for Civil, Mechanical, and Aerospace Systems 2008, vol. 6932, pp. 800–808 (2008). SPIE

[12] Zhao, Z., Soto, M.A., Tang, M., Thévenaz, L.: Distributed shape sensing using brillouin scattering in multi-core fibers. Optics express **24**(22), 25211–25223 (2016)

[13] Issatayeva, A., Amantayeva, A., Blanc, W., Tosi, D., Molardi, C.: Design and analysis of a fiber-optic sensing system for shape reconstruction of a minimally invasive surgical needle. Scientific reports **11**(1), 1–12 (2021)

[14] Waltermann, C., Doering, A., Köhring, M., Angelmahr, M., Schade, W.: Cladding waveguide gratings in standard single-mode fiber for 3d shape sensing. Optics letters **40**(13), 3109–3112 (2015)

[15] Roodsari, S.M., Freund, S., Zam, A., Rauter, G., Cattin, P.C.: Fabrication and characterization of a flexible fbg-based shape sensor using single-mode fibers. IEEE Transactions on Biomedical Engineering **69**(8), 2488–2498 (2022)

[16] Manavi, S., Witthauer, L., Iafolla, L., Zam, A., Rauter, G., Cattin, P.C.: Temperature-compensated fbg-based 3d shape sensor using single-mode fibers. In: Integrated Photonics Research, Silicon and Nanophotonics, pp. 6–1 (2018). Optical Society of America

[17] Moon, H., Jeong, J., Kim, O., Kim, K., Lee, W., Kang, S., Kim, J.: Fbg-based polymer-molded shape sensor integrated with minimally invasive surgical robots. In: 2015 IEEE International Conference on Robotics and Automation (ICRA), pp. 1770–1775 (2015). IEEE

[18] Ryu, S.C., Dupont, P.E.: Fbg-based shape sensing tubes for continuum robots. In: 2014 IEEE International Conference on Robotics and Automation (ICRA), pp. 3531–3537 (2014). IEEE

[19] Roesthuis, R.J., Janssen, S., Misra, S.: On using an array of fiber bragg grating sensors for closed-loop control of flexible minimally invasive surgical instruments. In: 2013 IEEE/Rsj International Conference on Intelligent Robots and Systems, pp. 2545–2551 (2013). IEEE

[20] Eickhoff, W., Ulrich, R.: Optical frequency domain reflectometry in single-mode fiber. Applied Physics Letters **39**(9), 693–695 (1981)

[21] Masoudi, A., Newson, T.P.: Contributed review: Distributed optical fibre dynamic strain sensing. Review of scientific instruments **87**(1), 011501 (2016)

[22] Bao, X., Chen, L.: Recent progress in distributed fiber optic sensors. sensors **12**(7), 8601–8639 (2012)

[23] Yüksel, K.: Rayleigh-based optical reflectometry techniques for distributed sensing applications. In: International Conference on Engineering Technologies, ICENTE'18 (2018). Selçuk Üniversitesi

[24] Beisenova, A., Issatayeva, A., Iordachita, I., Blanc, W., Molardi, C., Tosi, D.: Distributed fiber optics 3d shape sensing by means of high scattering np-doped fibers simultaneous spatial multiplexing. Optics express **27**(16), 22074–22087 (2019)

[25] Waltermann, C., Bethmann, K., Doering, A., Jiang, Y., Baumann, A.L., Angelmahr, M., Schade, W.: Multiple off-axis fiber bragg gratings for 3d shape sensing. Applied optics **57**(28), 8125–8133 (2018)

[26] Bao, W., Rong, Q., Chen, F., Qiao, X.: All-fiber 3d vector displacement (bending) sensor based on an eccentric fbg. Optics Express **26**(7), 8619–8627 (2018)

[27] Rong, Q., Guo, T., Bao, W., Shao, Z., Peng, G.-D., Qiao, X.: Highly sensitive fiber-optic accelerometer by grating inscription in specific core dip fiber. Scientific reports **7**(1), 1–9 (2017)

[28] Thomas, J., Jovanovic, N., Becker, R.G., Marshall, G.D., Withford, M.J., Tünnermann, A., Nolte, S., Steel, M.: Cladding mode coupling in highly localized fiber bragg gratings: modal properties and transmission spectra. Optics express **19**(1), 325–341 (2011)

[29] Thomas, J.U., Jovanovic, N., Krämer, R.G., Marshall, G.D., Withford, M.J., Tünnermann, A., Nolte, S., Steel, M.J.: Cladding mode coupling in highly localized fiber bragg gratings ii: complete vectorial analysis. Optics Express **20**(19), 21434–21449 (2012)

[30] Erdogan, T.: Cladding-mode resonances in short-and long-period fiber grating filters. JOSA A **14**(8), 1760–1773 (1997)

[31] Feng, D., Qiao, X., Albert, J.: Off-axis ultraviolet-written fiber bragg gratings for directional bending measurements. Optics letters **41**(6), 1201–1204 (2016)

[32] Galtarossa, A., Menyuk, C.R.: Polarization Mode Dispersion vol. 296. Springer, New York (2005)

[33] Smith, A.: Birefringence induced by bends and twists in single-mode optical fiber. Applied optics **19**(15), 2606–2611 (1980)

[34] Ulrich, R., Rashleigh, S., Eickhoff, W.: Bending-induced birefringence in single-mode fibers. Optics letters **5**(6), 273–275 (1980)

[35] Kersey, A.D., Davis, M.A., Patrick, H.J., LeBlanc, M., Koo, K., Askins, C., Putnam, M., Friebele, E.J.: Fiber grating sensors. Journal of lightwave technology **15**(8), 1442–1463 (1997)

[36] Block, U.L., Digonnet, M.J., Fejer, M.M., Dangui, V.: Bending-induced birefringence of optical fiber cladding modes. Journal of lightwave technology **24**(6), 2336 (2006)

[37] Marcuse, D.: Field deformation and loss caused by curvature of optical fibers. JOSA **66**(4), 311–320 (1976)

[38] Faustini, L., Martini, G.: Bend loss in single-mode fibers. Journal of lightwave technology **15**(4), 671–679 (1997)

[39] Valiente, I., Yassallo, C.: New formalism for bending losses in coated single-mode optical fibres. Electronics Letters **22**(25), 1544–1545 (1989)

[40] Harris, A., Castle, P.: Bend loss measurements on high numerical aperture single-mode fibers as a function of wavelength and bend radius. Journal of Lightwave technology **4**(1), 34–40 (1986)

[41] Murakami, Y., Tsuchiya, H.: Bending losses of coated single-mode optical fibers. IEEE Journal of Quantum Electronics **14**(7), 495–501 (1978)

[42] Morgan, R., Barton, J., Harper, P., Jones, J.: Temperature dependence of bending loss in monomode optical fibres. Electronics Letters **13**(26), 937–939 (1990)

[43] Renner, H.: Bending losses of coated single-mode fibers: a simple approach. Journal of Lightwave technology **10**(5), 544–551 (1992)

[44] Manavi, S., Renna, T., Horvath, A., Freund, S., Zam, A., Rauter, G., Schade, W., Cattin, P.C.: Using supervised deep-learning to model edge-fbg shape sensors: a feasibility study. In: Optical Sensors 2021, vol. 11772, pp. 79–88 (2021). SPIE

[45] Manavi, S., Huck-Horvath, A., Freund, S., Zam, A., Rauter, G., Schade, W., Cattin, P.C.: Using supervised deep-learning to model edge-fbg shape sensors. arXiv preprint arxiv:2210.16068 (2022)

[46] Li, L., Jamieson, K., DeSalvo, G., Rostamizadeh, A., Talwalkar, A.: Hyperband: A novel bandit-based approach to hyperparameter optimization. The Journal of Machine Learning Research **18**(1), 6765–6816 (2017)

[47] Shao, L.-Y., Xiong, L., Chen, C., Laronche, A., Albert, J.: Directional bend sensor based on re-grown tilted fiber bragg grating. Journal of Lightwave Technology **28**(18), 2681–2687 (2010)

[48] Renoirt, J.-M., Zhang, C., Debliquy, M., Olivier, M.-G., Mégret, P., Caucheteur, C.: High-refractive-index transparent coatings enhance the optical fiber cladding modes refractometric sensitivity. Optics Express **21**(23), 29073–29082 (2013)

[49] Morgan, R., Barton, J., Harper, P., Jones, J.D.: Wavelength dependence of bending loss in monomode optical fibers: effect of the fiber buffer coating. Optics letters **15**(17), 947–949 (1990)

Chapter 8

Conclusion and Outlook

8.1 Discussion

This thesis aimed to develop cost-effective shape-sensing solutions based on optical fibers for navigating continuum robots in RAMIS with clinically relevant accuracy. A tool tracking system in RAMIS provides a closed-loop motion control of continuum robots that makes path planning possible and alleviates manipulation safety concerns. The work presented here focuses on developing two shape-sensing solutions: sensors based on multiple single-mode fibers containing FBG arrays and edge-FBG shape sensors.

The first developed prototypes based on multiple fibers were presented in Chapters 3 and 4. The proposed sensor is categorized as a quasi-distributed FBG sensor, interrogated using the WDM technique. The designed sensor consists of three single-mode fibers, each with an array of five FBGs that are $5\,\mathrm{cm}$ apart. A sensor assembly setup was designed to align and fix the three fibers on a substrate with highly flexible glue, ensuring no twisting occurs during the gluing process. We selected two different substrates, a semi-rigid wire-braided Polyimide, and a super-elastic Nitinol wire, to study the effect of the substrate's stiffness on the sensor's performance.

The sensor probe with the semi-rigid substrate showed high thermal sensitivity. Therefore, a template-free motorized calibration setup in a temperature-controlled environment was designed to calibrate the sensor. The calibrated sensor showed high sensitivity to small deformations with curvature levels of $0.7\,\mathrm{m}^{-1}$ to $2.5\,\mathrm{m}^{-1}$. The average positioning error in this $20\,\mathrm{cm}$ long sensor was $\sim 2.7\,\mathrm{mm}$.

The sensor probe with the super-elastic substrate had a triangular cross-section and showed bending preferences at specific orientations. Therefore, four 3D curvature templates were designed to perform the sensor calibration in a controlled condition. Unlike typical calibration setups in which the sensor is rotated in a fixed curvature template, the designed curvature template was rotated to various orientations before the sensor insertion. This technique was successfully able to provide repeatable data for sensor calibration. However, the prediction accuracy of this $20\,\mathrm{cm}$ long sensor in multi-bend shape deformations (curvature range of $0.04\,\mathrm{m}^{-1}$ to $8.7\,\mathrm{m}^{-1}$) was not satisfactory and showed a median tip error of $9.9\,\mathrm{mm}$ to $16.2\,\mathrm{mm}$.

Some limitations could not be overcome in these sensor configurations, such as, low spatial resolution, glue aging, and the strain transfer between the substrate and the re-coated FBGs. Moreover, the calibration setup is always a limiting factor, as the shape accuracy of the ground truth is limited by the template. Such sensors can only be suitable for short flexible tools with limited flexibility, but not for detecting complex deformations in continuum robots. For longer sensors, expensive broader light sources and higher resolution spectrometers would be needed to increase the dynamic range of the sensor.

The second shape sensing solution we developed in this project was based on edge-FBGs. Edge-FBG shape sensors are highly flexible and can provide real-time shape estimations. The main challenge in edge-FBG shape sensors, which we addressed in this thesis, was the complexity of the sensor's response to shape deformations and the low shape prediction accuracy when using existing approaches from literature. In standard calibration techniques for fiber shape sensors, the fiber is rotated in a curvature template at known curvatures and all possible bending directions. However, in edge-FBG sensors, the intensity ratios between the co-located edge-FBGs, which carry the shape deformation information, are also sensitive to deformations applied to the fiber segments outside the sensing area. Therefore, the fiber part that connects the sensor to the interrogation system should be fixed during the calibration. On the other hand, such long and thin fibers might not perfectly follow the curvature template's movement during calibration, further limiting the calibration accuracy. Moreover, the existing approaches do not consider all the effects occurring in bent optical fibers and, consequently, cannot provide accurate shape predictions. Addressing the aforementioned challenges, we developed a new technique that does not require curvature templates or shape reconstruction steps and provides accurate shape prediction in real-time. In Chapter 5, we focused on studying the feasibility of modeling the complex behavior of edge-FBG shape sensors with deep learning techniques. We first studied the stability of the signal acquired by a low-cost interrogation system. This interrogator was examined in a setup designed for collecting sensor spectra during random shape deformation. As the accuracy level of ground truth shape estimation using templates was not satisfactory, we used a motion capture system to monitor the actual shape of the sensor during the data acquisition. We used custom-made reflective markers that did not limit the sensor's movements during manual shape manipulations. Then, we evaluated the performance of a simple network architecture in predicting the shape of the edge-FBG sensor.

In Chapter 6, we conducted a more thorough investigation using the deep learning technique. We defined the suitable settings of the data preprocessing steps and the hyperparameter search algorithm for designing the optimum network architecture. Moreover, we investigated an architectural design guided to learn similarities in the feature space, which considerably improved the prediction accuracy.

In Chapter 7, as the highlight of this PhD thesis, we proved that the deep learning technique upgrades the edge-FBG sensors from a quasi-distributed type into distributed fiber shape sensors. We studied possible sources of information that the deep learning model uses for such an upgrade. We also provided a visual explanation showing that spectral elements other than reflection peaks in the sensor's spectrum were vital for the deep learning model's decisions on the testing samples. We showed that the deep learning model performs better than a lookup table approach, in which the shape predictions are made by looking for the closest spectrum in the provided dataset. Such a comparison showed that deep learning was not memorizing the corresponding shape for each signal but rather found generalizing rules. The deep learning model we designed can accurately predict complex deformations, in a curvature range of $0.58\,\mathrm{m}^{-1}$ to $33.5\,\mathrm{m}^{-1}$, with a median tip error of almost $2\,\mathrm{mm}$. This shape sensing solution is 30 times less expensive than the commercially available distributed fiber shape sensor at a similar level of accuracy.

However, there are, of course, some challenges when using edge-FBG shape sensors. Although the deep learning model we developed can accurately predict complex shapes in the laboratory environment, it does not yet perform as well when it receives an input signal that is out of its expectations. The shape prediction error is almost one order of magnitude larger when the testing samples are from different shapes. Moreover, the sensor requires a referencing step prior to each use, as the spectrum profile of the straight fiber should be known for normalizing the input spectra. These sensors are not yet at a high technology readiness level and need further investigations, especially in an actual application environment.

8.2 Conclusion

This work has contributed to developing optical fiber-based shape sensing solutions for navigating continuum robots in RAMIS and flexible manual tools in MIS. We investigated two cost-effective shape sensing configurations, multiple single-mode fiber bundles, and an edge-FBG array sensor. Each presented shape sensing mechanism has certain benefits and drawbacks and can be suitable for specific applications. The fiber bundle with the semi-rigid tubular substrate has a working channel in the middle and is highly sensitive to small deformations. It can predict shapes with an uncertainty of around 1% and is suitable for navigating semi-flexible manual tools with a limited workspace and a maximum length of $20\,\mathrm{cm}$. The fiber bundle with a super-elastic wire has a more flexible substrate and can reach higher curvature levels. It can predict shapes with an uncertainty of 5% to 10%, depending on the complexity level of deformations. Such a sensor can be suitable for applications where large deflections are expected, but a centimeter range tip accuracy can still be acceptable. In general, shape sensors based on multiple single-mode fibers are limited by their substrate's properties, thermal sensitivity, and glue aging. In these sensors, there is always a trade-off between accuracy and flexibility.

In the second phase of this work, we investigated an edge-FBG array as the shape sensor. We studied the behavior of the sensor from the physical point of view and introduced possible sources of information that can be used to estimate the sensor's shape. As the behavior of such sensors is complex, standard characterization techniques are no longer applicable. Therefore, we developed a deep learning technique that can directly predict the fiber's 3D shape given the full spectrum of the edge-FBG array. We designed three CNNs using hyperparameter search with different search constraints and investigated their performance in predicting complex shapes. We also analyzed the impact of learning similarity metrics using the Siamese design on the deep learning model. The results showed that guiding the feature extractor subnetwork considerably improves the shape prediction accuracy. Given the limitations of template-based datasets, we designed a data acquisition setup where the edge-FBG sensor is manually manipulated while monitoring its actual shape using a motion capture system. Using this dataset, we trained our networks and were able to achieve a median tip accuracy of around $2\,\mathrm{mm}$ and a median RMSE of $1.4\,\mathrm{mm}$ in predicting the shape of a $25\,\mathrm{cm}$ long sensor. This approach requires no shape reconstruction algorithm and has upgraded the edge-FBG sensors to distributed shape sensors.

8.3 Outlook

The two fiber shape sensing solutions developed in this work are promising, but are not yet at a high technological readiness level. Despite the substantial limitations in the multiple single-mode fibers, there is still room for improvement. Mainly, for applications needing small deformation detection, one can use FBG arrays with smaller gaps between the sensing planes, creating a short shape sensor with high spatial resolution. For increasing the mechanical strength of the sensor probe, the currently used stripped FBGs can be replaced by draw tower gratings with polymer coatings. Also, dummy fibers can be placed around the substrate to create a symmetric cross-section for the sensor, minimizing bending preferences.

Based on the results of this work, we believe that edge-FBG sensors are promising navigation systems for medical applications, as they are highly flexible, accurate, and cost-effective. There is a great potential for advancing the presented modeling technique further to improve the accuracy and reliability of these sensors. In the context of the dataset, one can automate the shape manipulation process during data acquisition to cover the sensor's workspace and create representative training data. We also expect that training the implemented deep learning model application-wise, where certain constraints limit the sensor's movement, can improve the prediction accuracy. One could also try more advanced network architectures, extracting deeper features from the edge-FBGs spectra to create more general models. The sensor also needs to be tested in real application environments for stability and reliability.

Another remark could be to further investigate the possible sources of information in edge-FBG sensors and conduct experiments estimating which physical effect in a bent edge-FBG sensor contributes more to the deep learning model's decisions. This can be done by studying the sensor's behavior when the impact of one effect at a time is minimized. For instance, the interrogation system can be designed as polarization-insensitive to highlight the impact of polarization-dependent loss on the sensor's response. Also, particular types of fiber that limit the whispering gallery/cladding modes can be selected for edge-FBG inscription. Moreover, one can investigate the impact of the spectral gap between the edge-FBGs, the distance between the sensing planes, the coating material, and the temperature variation on the shape prediction accuracy.

Another research topic would be to use a high-resolution spectrometer that provides more spectral information on the FBGs side bands. One can also use apodized or geometrically corrected Bragg gratings to remove the side bands and study their possible influence. Investigating the cladding modes in more detail by addressing the following questions: how long do the cladding modes survive in edge-FBG sensors? What happens if the FBGs are inscribed closer to the cladding area? Would it improve the sensor's performance if a recoupling technique that couples the cladding modes back to the fiber's core is used?

Even though there is still room for improvement for a cost-effective and accurate fiber shape sensing solution, we demonstrated in this thesis that this emerging technology has great potential for navigating continuum robots in RAMIS.

Bibliography

[1] Optical Measurement/ Optical Tracking - NDI.

[2] Surgical Navigation/ Optical Tracking - Kick.

[3] W. Bao, Q. Rong, F. Chen, and X. Qiao. All-fiber 3d vector displacement (bending) sensor based on an eccentric fbg. *Optics Express*, 26(7):8619–8627, 2018.

[4] X. Bao and L. Chen. Recent progress in distributed fiber optic sensors. *sensors*, 12(7):8601–8639, 2012.

[5] D. Barrera, I. Gasulla, and S. Sales. Multipoint two-dimensional curvature optical fiber sensor based on a nontwisted homogeneous four-core fiber. *Journal of Lightwave Technology*, 33(12):2445–2450, 2014.

[6] A. Beisenova, A. Issatayeva, C. Molardi, D. Tosi, I. Iordachita, and W. Blanc. Distributed fiber optics 3D shape sensing by means of high scattering NP-doped fibers simultaneous spatial multiplexing. *Optics Express, Vol. 27, Issue 16, pp. 22074-22087*, 27(16):22074–22087, aug 2019.

[7] C. Bergeles and G. Z. Yang. From passive tool holders to microsurgeons: Safer, smaller, smarter surgical robots. *IEEE Transactions on Biomedical Engineering*, 61(5):1565–1576, 2014.

[8] U. L. Block, M. J. Digonnet, M. M. Fejer, and V. Dangui. Bending-induced birefringence of optical fiber cladding modes. *Journal of lightwave technology*, 24(6):2336, 2006.

[9] R. W. Boyd. *Nonlinear optics*. Academic press, 2020.

[10] J. Burgner-Kahrs, D. C. Rucker, and H. Choset. Continuum Robots for Medical Applications: A Survey. *IEEE Transactions on Robotics*, 31(6):1261–1280, 2015.

[11] F. Chen, D. Su, X. Qiao, and Q. Rong. Compact vector bend sensor using dual-off-axis innermost cladding-type fbgs. *IEEE sensors journal*, 18(18):7476–7480, 2018.

[12] M. Cohen, R. Shavit, and Z. Zalevsky. *Planar Waveguides and other Confined Geometries*, volume 189. Springer New York, 2015.

[13] L. Cooper, A. Webb, A. Gillooly, M. Hill, T. Read, P. Maton, J. Hankey, and A. Bergonzo. Design and performance of multicore fiber optimized towards communications and sensing applications. In *Optical Components and Materials XII*, volume 9359, pages 82–88. SPIE, 2015.

[14] M. Dehghani and S. A. A. Moosavian. Compact modeling of spatial continuum robotic arms towards real-time control. *Advanced Robotics*, 28(1):15–26, 2014.

[15] X. Dong, H. Zhang, B. Liu, and Y. Miao. Tilted fiber bragg gratings: Principle and sensing applications. *Photonic Sensors*, 1(1):6–30, 2011.

[16] P. Drexler and P. Fiala. *Optical fiber birefringence effects–sources, utilization and methods of suppression*. InTech, 2011.

[17] W. Eickhoff and R. Ulrich. Optical frequency domain reflectometry in single-mode fiber. *Applied Physics Letters*, 39(9):693–695, 1981.

[18] T. Erdogan. Cladding-mode resonances in short-and long-period fiber grating filters. *JOSA A*, 14(8):1760–1773, 1997.

[19] L. Faustini and G. Martini. Bend loss in single-mode fibers. *Journal of lightwave technology*, 15(4):671–679, 1997.

[20] G. Flockhart, W. MacPherson, J. Barton, J. Jones, L. Zhang, and I. Bennion. Two-axis bend measurement with bragg gratings in multicore optical fiber. *Optics letters*, 28(6):387–389, 2003.

[21] I. Floris, J. M. Adam, P. A. Calderón, and S. Sales. Fiber optic shape sensors: A comprehensive review. *Optics and Lasers in Engineering*, 139:106508, 2021.

[22] A. Galtarossa and C. R. Menyuk. *Polarization mode dispersion*, volume 296. Springer, 2005.

[23] J. M. Gere and B. J. Goodno. *Mechanics of materials*. Cengage learning, 2012.

[24] H. B. Gilbert, D. C. Rucker, and R. J. Webster. Concentric tube robots: The state of the art and future directions. *Springer Tracts in Advanced Robotics*, 114:253–269, 2016.

[25] J.-P. Goure and I. Verrier. *Optical fibre devices*. CRC Press, 2016.

[26] A. Harris and P. Castle. Bend loss measurements on high numerical aperture single-mode fibers as a function of wavelength and bend radius. *Journal of Lightwave technology*, 4(1):34–40, 1986.

[27] M. Heiblum and J. Harris. Analysis of curved optical waveguides by conformal transformation. *IEEE Journal of Quantum Electronics*, 11(2):75–83, 1975.

[28] O. V. Ivanov, S. A. Nikitov, and Y. V. Gulyaev. Cladding modes of optical fibers: properties and applications. *Physics-Uspekhi*, 49(2):167, 2006.

[29] K. Jamieson and A. Talwalkar. Non-stochastic best arm identification and hyperparameter optimization. In *Artificial intelligence and statistics*, pages 240–248. PMLR, 2016.

[30] L. B. Jeunhomme. *Single-mode fiber optics: principles and applications*. Routledge, 2019.

[31] B. A. Jones, W. McMahan, and I. D. Walker. Practical kinematics for real-time implementation of continuum robots. *Proceedings - IEEE International Conference on Robotics and Automation*, 2006(6):1840–1847, 2006.

[32] R. Kashyap. *Fiber bragg gratings*. Academic press, 2009.

[33] A. D. Kersey, M. A. Davis, H. J. Patrick, M. LeBlanc, K. Koo, C. Askins, M. Putnam, and E. J. Friebele. Fiber grating sensors. *Journal of lightwave technology*, 15(8):1442–1463, 1997.

[34] A. Khadour and J. Waeytens. Monitoring of concrete structures with optical fiber sensors. In *Eco-Efficient Repair and Rehabilitation of Concrete Infrastructures*, pages 97–121. Elsevier, 2018.

[35] F. Khan, A. Denasi, D. Barrera, J. Madrigal, S. Sales, and S. Misra. Multi-Core Optical Fibers with Bragg Gratings as Shape Sensor for Flexible Medical Instruments. *IEEE Sensors Journal*, 19(14):5878–5884, jul 2019.

[36] F. Khan, R. J. Roesthuis, and S. Misra. Force sensing in continuum manipulators using fiber bragg grating sensors. In *2017 IEEE/RSJ International Conference on Intelligent Robots and Systems (IROS)*, pages 2531–2536. IEEE, 2017.

[37] C. Kim, S. C. Ryu, and P. E. Dupont. Real-time adaptive kinematic model estimation of concentric tube robots. *IEEE International Conference on Intelligent Robots and Systems*, 2015-December:3214–3219, 2015.

[38] K. C. Kim and P. Volpe. *Bariatric Robotic Surgery*. Springer International Publishing, Cham, 2019.

[39] K. S. Lee and T. Erdogan. Fiber mode conversion with tilted gratings in an optical fiber. *JOSA A*, 18(5):1176–1185, 2001.

[40] P. Lenke, M. Wendt, K. Krebber, and R. Glötzl. Highly sensitive fiber optic inclinometer: easy to transport and easy to install. In *21st International Conference on Optical Fiber Sensors*, volume 7753, pages 758–761. SPIE, 2011.

[41] L. Li, K. Jamieson, G. DeSalvo, A. Rostamizadeh, and A. Talwalkar. Hyperband: A novel bandit-based approach to hyperparameter optimization. *The Journal of Machine Learning Research*, 18(1):6765–6816, 2017.

[42] H.-l. Liu, Z.-w. Zhu, Y. Zheng, B. Liu, and F. Xiao. Experimental study on an fbg strain sensor. *Optical Fiber Technology*, 40:144–151, 2018.

[43] S. Loranger, M. Gagné, V. Lambin-Iezzi, and R. Kashyap. Rayleigh scatter based order of magnitude increase in distributed temperature and strain sensing by simple uv exposure of optical fibre. *Scientific reports*, 5(1):1–7, 2015.

[44] S. Manavi, T. Renna, A. Horvath, S. Freund, A. Zam, G. Rauter, W. Schade, and P. C. Cattin. Using supervised deep-learning to model edge-FBG shape sensors: a feasibility study. In F. Baldini, J. Homola, and R. A. Lieberman, editors, *Optical Sensors 2021*, volume 11772, page 117720P. International Society for Optics and Photonics, SPIE, 2021.

[45] S. Manavi, L. Witthauer, L. Iafolla, A. Zam, G. Rauter, and P. C. Cattin. Temperature-compensated fbg-based 3d shape sensor using single-mode fibers. In *Advanced Photonics 2018 (BGPP, IPR, NP, NOMA, Sensors, Networks, SPPCom, SOF)*, page JTu6C.1. Optica Publishing Group, 2018.

[46] G. Marowsky. *Planar waveguides and other confined geometries: Theory, technology, production, and novel applications*, volume 189. Springer, 2014.

[47] A. Martinez, M. Dubov, I. Khrushchev, and I. Bennion. Direct writing of fibre bragg gratings by femtosecond laser. *Electronics Letters*, 40(19):1, 2004.

[48] A. Martinez, Y. Lai, M. Dubov, I. Khrushchev, and I. Bennion. Vector bending sensors based on fibre bragg gratings inscribed by infrared femtosecond laser. *Electronics Letters*, 41(8):1, 2005.

[49] A. Masoudi and T. P. Newson. Contributed review: Distributed optical fibre dynamic strain sensing. *Review of scientific instruments*, 87(1):011501, 2016.

[50] H. Moon, J. Jeong, S. Kang, K. Kim, Y.-W. Song, and J. Kim. Fiber-bragg-grating-based ultrathin shape sensors displaying single-channel sweeping for minimally invasive surgery. *Optics and Lasers in Engineering*, 59:50–55, 2014.

[51] J. P. Moore and M. D. Rogge. Shape sensing using multi-core fiber optic cable and parametric curve solutions. *Optics express*, 20(3):2967–2973, 2012.

[52] R. Morgan, J. Barton, P. Harper, and J. D. Jones. Wavelength dependence of bending loss in monomode optical fibers: effect of the fiber buffer coating. *Optics letters*, 15(17):947–949, 1990.

[53] Y. Murakami and H. Tsuchiya. Bending losses of coated single-mode optical fibers. *IEEE Journal of Quantum Electronics*, 14(7):495–501, 1978.

[54] N. Patel, C. Seneci, G.-Z. Yang, A. Darzi, and J. Teare. Flexible platforms for natural orifice transluminal and endoluminal surgery. *Endoscopy International Open*, 02(02):E117–E123, 2014.

[55] H. Renner. Bending losses of coated single-mode fibers: a simple approach. *Journal of Lightwave technology*, 10(5):544–551, 1992.

[56] G. Robinson and J. B. Davies. Continuum robots - a state of the art. *Proceedings - IEEE International Conference on Robotics and Automation*, 4(May):2849–2854, 1999.

[57] R. J. Roesthuis, M. Kemp, J. J. van den Dobbelsteen, and S. Misra. Three-dimensional needle shape reconstruction using an array of fiber bragg grating sensors. *IEEE/ASME transactions on mechatronics*, 19(4):1115–1126, 2013.

[58] S. M. Roodsari, S. Freund, A. Zam, G. Rauter, and P. C. Cattin. Fabrication and characterization of a flexible fbg-based shape sensor using single-mode fibers. *IEEE Transactions on Biomedical Engineering*, 69(8):2488–2498, 2022.

[59] B. E. Saleh and M. C. Teich. *Fundamentals of photonics*. john Wiley & sons, 2019.

[60] R. Scarmozzino, A. Gopinath, R. Pregla, and S. Helfert. Numerical techniques for modeling guided-wave photonic devices. *IEEE Journal of Selected Topics in Quantum Electronics*, 6(1):150–162, 2000.

[61] L. Schenato. A review of distributed fibre optic sensors for geo-hydrological applications. *Applied Sciences*, 7(9):896, 2017.

[62] R. T. Schermer and J. H. Cole. Improved bend loss formula verified for optical fiber by simulation and experiment. *IEEE Journal of Quantum Electronics*, 43(10):899–909, 2007.

[63] L.-Y. Shao, L. Xiong, C. Chen, A. Laronche, and J. Albert. Directional bend sensor based on re-grown tilted fiber bragg grating. *Journal of Lightwave Technology*, 28(18):2681–2687, 2010.

[64] A. Smith. Birefringence induced by bends and twists in single-mode optical fiber. *Applied optics*, 19(15):2606–2611, 1980.

[65] A. W. Snyder and J. Love. *Optical waveguide theory*. Springer Science & Business Media, 2012.

[66] B. J. Soller, D. K. Gifford, M. S. Wolfe, and M. E. Froggatt. High resolution optical frequency domain reflectometry for characterization of components and assemblies. *Optics express*, 13(2):666–674, 2005.

[67] G. Tangonan, V. Jones, J. Pikulski, and H. Hsu. Bend loss measurements for small mode field diameter fibres. *Electronics Letters*, 25:142, 1989.

[68] J. Thomas, N. Jovanovic, R. G. Becker, G. D. Marshall, M. J. Withford, A. Tünnermann, S. Nolte, and M. Steel. Cladding mode coupling in highly localized fiber bragg gratings: modal properties and transmission spectra. *Optics express*, 19(1):325–341, 2011.

[69] J. U. Thomas, N. Jovanovic, R. G. Krämer, G. D. Marshall, M. J. Withford, A. Tünnermann, S. Nolte, and M. J. Steel. Cladding mode coupling in highly localized fiber bragg gratings ii: complete vectorial analysis. *Optics Express*, 20(19):21434–21449, 2012.

[70] J. Troccaz. *Medical Robotics*. John Wiley and Sons, Inc., Hoboken, NJ USA, feb 2013.

[71] R. Ulrich, S. Rashleigh, and W. Eickhoff. Bending-induced birefringence in single-mode fibers. *Optics letters*, 5(6):273–275, 1980.

[72] I. Valiente and C. Yassallo. New formalism for bending losses in coated single-mode optical fibres. *Electronics Letters*, 22(25):1544–1545, 1989.

[73] N. J. Van De Berg, D. J. Van Gerwen, J. Dankelman, and J. J. Van Den Dobbelsteen. Design Choices in Needle Steering - A Review. *IEEE/ASME Transactions on Mechatronics*, 20(5):2172–2183, 2015.

[74] H. Venghaus. *Wavelength filters in fibre optics*, volume 123. springer, 2006.

[75] V. Vitiello, S. L. Lee, T. P. Cundy, and G. Z. Yang. Emerging robotic platforms for minimally invasive surgery. *IEEE Reviews in Biomedical Engineering*, 6:111–126, 2013.

[76] M. Wagner, S. Schafer, C. Strother, and C. Mistretta. 4D interventional device reconstruction from biplane fluoroscopy. *Medical Physics*, 43(3):1324–1334, mar 2016.

[77] I. D. Walker. Continuous Backbone “Continuum” Robot Manipulators. *ISRN Robotics*, 2013:1–19, 2013.

[78] C. Waltermann, K. Bethmann, A. Doering, Y. Jiang, A. L. Baumann, M. Angelmahr, and W. Schade. Multiple off-axis fiber Bragg gratings for 3D shape sensing. *Applied Optics*, 57(28):8125, 2018.

[79] X. Wang and M. Q.-H. Meng. Robotics for Natural Orifice Transluminal Endoscopic Surgery: A Review. *Journal of Robotics*, 2012:1–9, 2012.

[80] Y. Wang, B. Shi, T. Zhang, H. Zhu, Q. Jie, and Q. Sun. Introduction to an fbg-based inclinometer and its application to landslide monitoring. *Journal of Civil Structural Health Monitoring*, 5(5):645–653, 2015.

[81] R. J. Webster and B. A. Jones. Design and kinematic modeling of constant curvature continuum robots: A review. *International Journal of Robotics Research*, 29(13):1661–1683, 2010.

[82] P. Westbrook, K. Feder, T. Kremp, T. Taunay, E. Monberg, J. Kelliher, R. Ortiz, K. Bradley, K. Abedin, D. Au, et al. Integrated optical fiber shape sensor modules based on twisted multicore fiber grating arrays. In *Optical Fibers and Sensors for Medical Diagnostics and Treatment Applications XIV*, volume 8938, pages 88–94. SPIE, 2014.

[83] P. S. Westbrook, T. Kremp, K. S. Feder, W. Ko, E. M. Monberg, H. Wu, D. A. Simoff, S. Shenk, and R. M. Ortiz. Performance characteristics of continuously grated multicore sensor fiber. In *2017 25th Optical Fiber Sensors Conference (OFS)*, pages 1–4. IEEE, 2017.

[84] P. S. Westbrook, T. Kremp, K. S. Feder, W. Ko, E. M. Monberg, H. Wu, D. A. Simoff, T. F. Taunay, and R. M. Ortiz. Continuous multicore optical fiber grating arrays for distributed sensing applications. *Journal of Lightwave Technology*, 35(6):1248–1252, 2017.

[85] K. Xu and N. Simaan. Analytic formulation for kinematics, statics, and shape restoration of multibackbone continuum robots via elliptic integrals. *Journal of Mechanisms and Robotics*, 2(1):1–13, 2010.

[86] B. Yang, J. Duan, Z. Xie, and H. Xiao. Evaluation of Mode Field Diameter of Step-Index Fibers and Comparison Analysis. *Research Journal of Applied Sciences, Engineering and Technology*, 6(3):382–386, 2013.

[87] S. Yin, P. B. Ruffin, and T. Francis. *Fiber optic sensors*. CRC press, 2017.

[88] K. Yüksel. Rayleigh-based optical reflectometry techniques for distributed sensing applications. In *International Conference on Engineering Technologies, ICENTE'18*. Selçuk Üniversitesi, 2018.

[89] L. Zhang, X. Qiao, Q. Liu, M. Shao, Y. Jiang, and D. Huang. Off-axis ultraviolet-written thin-core fiber bragg grating for directional bending measurements. *Optics Communications*, 410:197–201, 2018.

[90] Z. Zhao, M. A. Soto, M. Tang, and L. Thévenaz. Distributed shape sensing using brillouin scattering in multi-core fibers. *Optics express*, 24(22):25211–25223, 2016.

[91] D. Zheng, J. Madrigal, H. Chen, D. Barrera, and S. Sales. Multicore fiber-bragg-grating-based directional curvature sensor interrogated by a broadband source with a sinusoidal spectrum. *Optics Letters*, 42(18):3710–3713, 2017.

[92] W. Zou, X. Long, and J. Chen. Brillouin scattering in optical fibers and its application to distributed sensors. *Advances in Optical Fiber Technology: Fundamental Optical Phenomena and Applications*, 2015.